Analysis of hemodynamic indicators in Bicuspid Aortic Valves using a computational mathematical model

Ana Sofia Bernardo Torrado

Thesis to obtain the Master of Science Degree in

Biomedical Engineering

Supervisors: Prof. Adélia da Costa Sequeira dos Ramos Silva

Doctor Jorge Filipe Duarte Tiago

Examination Committee

Chairperson: Prof. Cláudia Alexandra Martins Lobato da Silva

Supervisor: Prof. Adélia da Costa Sequeira dos Ramos Silva

Members of the Committee: Doctor Sérgio Matoso Laranjo

November 2015

Tenho em mim todos os sonhos do Mundo.

Fernando Pessoa

Acknowledgments

The author would like to thank Professor Adélia Sequeira and Doctor Jorge Tiago. Both were great supervisors, sharing with me their vast knowledge, and creating a great environment for my professional development and growth.

Special thanks to Professor Adélia Sequeira, for giving me the opportunity to work with her, believing in my work and proposing me new challenges: (i) working in the Center for Computational and Stochastic Mathematics at Instituto Superior Técnico (Lisbon, Portugal), in collaboration with the Pediatric Cardiology Department of Santa Marta Hospital (Lisbon, Portugal); (ii) but also the most enthusiastic experience of my life, the 2015 summer internship in Advanced Computing Research, in the Center for Cardiovascular Simulation, at the University of Texas, at Austin (USA).

To Doctor Jorge Tiago for giving me an enthusiastic support to the on-going development of the project, providing valuable input (always!), ideas, and encouragement. This support was invaluable in achieving the numerical simulations and in solving issues on COMSOL Multiphysics.

I am very grateful to Doctor Fátima Pinto, Medical Director of the Pediatric Cardiology Department, at the Santa Marta Hospital (introduced to me by Professor Adélia Sequeira) for providing me the medical images to develop my work. I would like thank Doctor Sérgio Laranjo and Doctor Marta António, for their important contribution from the medical point of view (on MRI images and the BAV data base), as well as all the time spent on this enthusiastic project.

To Professor Luis Sousa (Mechanics Department, Instituto Superior Técnico), who help me in the construction of the three dimensions Tricuspid Aortic model, on Solidworks.

Finally, thanks to my friends and, mainly, to my wonderful parents who have always been so supportive, emotionally (as source of motivation, optimism and happiness in my life) and financially. Thank you for allowing me this opportunity to grow and learn. I could not have made it without you. Thank you all for the guidance and the willingness!!!

Abstract

The Bicuspid Aortic Valve (BAV) is a congenital cardiac disorder, prevalent in 1%–2% of the general population, where 33% of BAV patients may experience vascular complications. BAV consists of two cusps/leaflets instead of three, as in a normal aortic valve (Tricuspid Aortic Valve, TAV). This thesis is devoted to the numerical study of hemodynamic effects in different BAV geometries (2D) using a Fluid Structure Interaction (FSI) method with an Arbitrary Lagrangian Eulerian (ALE) approach. One idealized TAV model and six BAVs corresponding to patient-specific geometries (with aortic root dimensions measured from MRI exams) were analyzed. These geometries were studied according to: (i) velocity blood flow, (ii) mechanical structural (leaflets/aortic root wall) deformations (Von Mises stress) and (iii) hemodynamic stresses analysis (Wall Shear Stresses, WSS; Oscilatory Shear Index, OSI), during two cardiac cycles. Comparing BAVs with TAV analysis, BAVs present asymmetric blood flow jets, vortices and larger WSS on the leaflets (in particular on the belly and on the tip), which can be a potential cause for early valvular calcification or exacerbate the existent calcification. Regarding our FSI numerical simulations applied to all BAV models, we verified: (i) maximum velocity magnitudes greater than 2 m/s; (ii) higher Von Mises stress on the leaflets, with maximum values of 1.0×10^6 Pa; (iii) abnormal WSS stresses with values greater than 8 N/m^2 on the leaflets (higher WSS on the pathological fused leaflet). To complement this work, a 3D TAV geometry was considered and some numerical simulations were performed and briefly analyzed.

Keywords: Hemodynamic Indicators, Bicuspid Aortic Valve, Tricuspid Aortic Valve, Fluid Structure Interaction, Arbitrary Lagrangian Eulerian formulation, COMSOL Multiphysics

Resumo

A Válvula Aórtica Bicúspide (BAV) é uma patologia cardíaca congénita, que afecta 1%-2% da população em geral, em que 33% destes pacientes têm tendência a apresentar complicações vasculares. A BAV possui duas cúspides/folhetos, em vez de três (como numa Válvula Aórtica Tricúspide, TAV). Neste trabalho, efectuou-se o estudo numérico dos efeitos hemodinâmicos em diferentes geometrias de BAV, utilizando-se um método numérico de Interacção Fluido Estrutura (FSI) baseado numa formulação Lagrangiana Euleriana Arbitrária (ALE). Consideraram-se mais precisamente, uma TAV idealizada e 6 BAVs (correspondendo a geometrias que foram construídas recorrendo a dimensões recolhidas a partir de exames de Ressonâncias Magnéticas). Estas geometrias foram estudadas considerando: (i) análise de velocidades; (ii) deformações da estrutura (folhetos e parede da válvula aórtica) através de tensões de Von Mises; (ii) tensões hemodinâmicas (tensão de cisalhamento nas paredes, WSS; índice oscilatório de cisalhamento, OSI) durante dois ciclos cardíacos. Comparando com a análise da TAV, as BAVs apresentam fluxos sanguíneos assimétricos, com vórtices e mais elevado WSS concentrado nos folhetos (em particular no topo e na região central). Tal poderá potenciar o início do processo de calcificação ou agravar a calcificação já existente. Nas simulações numéricas realizadas, para todas as geometrias BAV, verificaram-se: (i) velocidades superiores a 2 m/s; (ii) elevadas tensões de Von Mises nos folhetos, com valores máximos de 1.0×10^6 Pa; (iii) WSS não usuais com valores máximos superiores a 8 N/m^2 e concentrados nos folhetos (particularmente no folheto patológico definido). Para complementar este trabalho foi ainda desenvolvida uma TAV 3D e feitas simulações computacionais que foram brevemente analisadas.

Palavras chave: Indicadores Hemodinâmicos, Válvula Aórtica Bicúspide, Válvula Aórtica Tricúspide, Interacção Fluido Estrutura, Formulação Lagrangeana Euleriana Arbitrária, COMSOL Multiphysics

Contents

List of Figures

List of Tables

List of Acronyms

2D – Two dimensional

3D - Three dimensional

ALE - Arbitrary Lagrangian Eulerian

BAV - Bicuspid Aortic Valve

BHV – Bioprosthetic Heart Valve

CT – Computed Tomography

CAS - Calcific Aortic Stenosis

CAVD - Calcific Aortic Valve Disease

EOA - Effective orifice area

FDRs - First-Degree Relatives

FE - Finite element

FSI – Fluid Structure Interaction

LCC - Left Coronary Cusp

MRI – Magnetic Resonance Imaging

NCC - Non-Coronary Cusp

OSI – Oscillatory Shear Index

PDE - Partial Differential Equation

RCC - Right Coronary Cusp

TAV – Tricuspid Aortic Valve

WSS – Wall Shear Stress

CHAPTER 1

Introduction

1.1. Background

Bicuspid aortic valve (BAV) is one of the most prominent congenital heart valve defects, prevalent in 1%–2% of the general population[1–7]**.** The congenital valve disease and the non-pathological case, the normal tricuspid aortic valve (TAV), are good candidates for computational analysis and simulations due to the inaccessible location of the aortic valves, their complex function and geometry[2,8–12]. The anatomy of these valves has been studied and reviewed extensively[12]. It was recognized that patients with BAV generally have congenital abnormalities which affect the aortic root, and consequently an abnormal blood flow can be verified leading to the development of problems in the ascending aortic root of BAV patients[13]. However, the treatment strategy for TAV and BAV is challenging. It's necessary to capture the hemodynamic details that promote those clinical problems. With the developments in cardiac imaging, the advancements in human molecular genetics, vascular biology, imaging techniques devoted to the heart valve diagnosis (Echocardiography, Computed Tomography Imaging or Magnetic Resonance Imaging) and computational methods (Computed Dynamics Fluid or Fluid Structure Interaction approaches), it is possible to obtain a better understanding of the etiology of the aortic disease associated with the BAV[3,4]. Computational methods, such as the Fluid Structure Interaction (FSI), have been used for medical reasons, because millions of people are annually diagnosed with aortic valve disorders - aortic stenosis and aortic insufficiency[14]. The most adequate computational method that studies the valve deformation due to the blood flow is the FSI based on an Arbitrary Lagrangian Eulerian (ALE) formulation[15]. This method helps in the evaluation of the hemodynamics influence of an asymmetric valve configuration, and consequently it can be used for planning clinical interventions[16].

1.2. Motivations and objectives

The knowledge of the anatomy and the physiology of the BAV has not been completely assessed, because in vivo and ex-vivo experiments using BAVs have been limited[16]. It can be extremely important for surgical techniques in terms of repairing cardiac valves and it can also have important impact in the manufacture of bioprosthetic heart valves (BHV). The study of the aortic valve and its root using FSI method has been studied. More recently several studies have been made due to the importance of understanding the real aortic valve behavior in normal and, mainly, in pathological cases. Previous studies did not produce sufficient data in terms of the influence of asymmetric morphologies on BAV, and hemodynamic stresses remain largely unknown[17]. There are also few studies that employ physiologic boundary conditions and use realistic material models to simulate the behavior of different BAVs. The objectives of this study include the construction of a TAV geometry (2D and 3D) and the implementation of FSI methods (for 2D models and, briefly, for a 3D model). As a result we will generate idealized BAVs (2D) and examine the influence of the morphologic characteristics in the aortic root and ascending thoracic aorta, employing physiologically realistic boundary conditions. In order to understand the BAV disease, we will analyze different aspects of the blood flow, in the BAV geometries previously generated, during the cardiac cycle, and we will compare the results with the healthy case (TAV model). These objectives will be reached though numerical simulations to obtain results for the blood flow velocity, Von Mises stresses on the cusps, WSS on the valve structure and OSI analysis.

1.3. Methodology

In order to obtain a characterization of the hemodynamic factors and the flow profile of the blood associated to different disease aortic valves we will do numerical simulations of the blood flow and its interaction with the valve and the aortic wall. To this end, we will pursue the following stages: (i) 2D

geometries construction, (ii) numerical simulation of blood flow in the aortic valve (a TAV and six idealized BAVs geometries) applying the FSI method with an ALE formulation on COMSOL Multiphysics[18]; (iii) the study of hemodynamic indicators and respective comparison between normal and pathological cases; finally, (iv) the validation of the results with those found in the literature. As additional work a 3D TAV model using the Solidworks 2014 will be created and, briefly, analyzed.

1.4. Thesis outline

This thesis is divided into 5 chapters.

Chapter 1 is the introduction where we present the background, motivations and purposes of this work.

Chapter 2 presents a literature review concerning medical aspects about Tricuspid Aortic Valve and Bicuspid Aortic Valve. A description related with the current imaging acquisition methods used and a review of the computational methodology are also given.

Chapter 3 describes the methods used in the present work, concerning: (i) the FSI numerical method based on the ALE approach, and respective problem definition as well as the governing equations; (ii) geometrical two-dimensional construction of TAV and different patient-specific BAV models (according with the process of data acquisition); (iii) numerical simulations in two dimensions on COMSOL[18]; (iii) geometrical three-dimensional construction of TAV on Solidworks.

Chapter 4 presents and discusses the results obtained with the methodology used in this work.

Finally, in Chapter 5, the main conclusions, limitations, future perspectives and developments are presented and suggested.

CHAPTER 2

Literature Review

This review of existent literature in the field starts with principal medical features about Aortic Valve (anatomy and dynamics of the aortic root, histology and biomechanics of leaflets) and describes the respective pathological condition, Bicuspid Aortic Valve (BAV), concerning the prevalence, embryology, anatomy and classification, respective pathologic patterns. Then, we present the state of the art related with Imaging Acquisition Methods (Echocardiographic, Computed Tomography Imaging and Magnetic Resonance imaging) that are used to construct Patient Specific Geometrical Models of cardiac valves. Finally, we describe briefly the Computational methods (Computational Fluid Dynamics, Fluid Structure Interaction) used in relevant previous works.

2.1. Aortic Valve

The human heart is subdivided by septa into right and left halves, and it has a subdivision of each half part into two cavities - the atrium and the ventricle (Figure 2.1.A). It presents four valves: the (i) atrioventricular valves - the mitral valve and the tricuspid valve (TAV) - situated at the transition between the left atrium to left ventricle and right atrium to right ventricle, respectively; (ii) the semilunar valves – the pulmonary valve and the aortic valve – are placed at the transition from the right ventricle to the pulmonary artery and from the left ventricle to the aorta, respectively. The left ventricle receives oxygenated blood from the left atrium via mitral valve, and the left ventricle pumps the blood into the aorta (the main vessel that transports through the aortic valve the oxygenated blood to the tissues)[15].

2.1.1. Anatomy of the aortic root

Anatomically, a non-pathological aortic valve, placed in the aortic root, includes three cusps or leaflets (Left Coronary Cusp, LCC; Non-Coronary Cusp, NCC; Right Coronary Cusp, RCC) and three

sinuses - the dilatations opposite to the cusps – that are connected through the commissures. The aortic root is related with the aortic valve from its position at the left ventricular outlet to the junction with the ascending aorta – through the sinotubular junction (here the aortic sinuses end and the aorta becomes tubular)[14,15]. The aortic root has four components: aortic annulus, aortic cusps, aortic or Valsalva sinuses and sinotubular junction (Figure 2.1B). Each aortic root component contributes to the intermittent, unidirectional channelling of large volumes of fluid, maintaining laminar flow, minimal resistance and the least possible tissue stress[19].

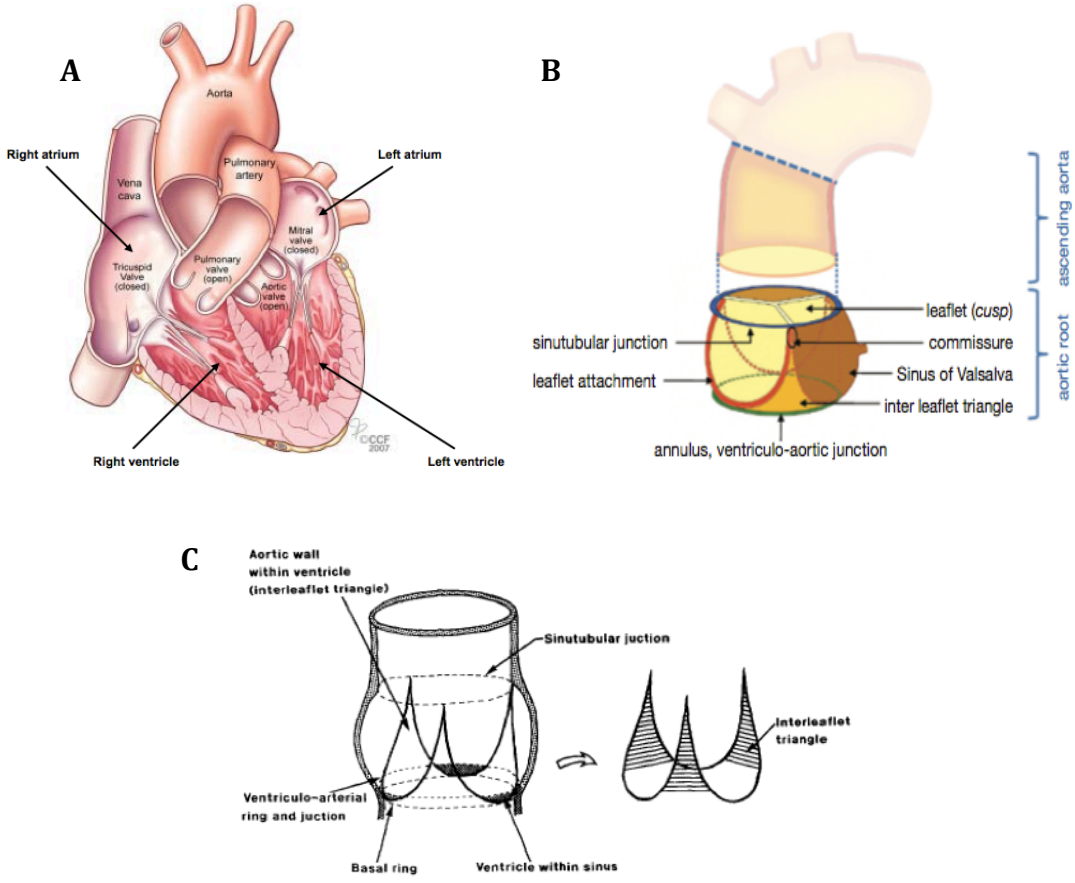

Figure 2.1. Illustrations: A. The heart presents four valves: the mitral valve, the tricuspid valve, the pulmonary valve and the aortic valve[21]. B. The nomenclature for the aortic root components[19]. C. Sketch of the aortic root: The interleaflet triangles, as extensions of the ventricular outflow tract[2].

The aortic valve leaflets – the trileaflet design - form the aortic valve allows the sealing mechanism, the optimal solution for achieving low resistance valve opening[19,20]. The three leaflets are anatomically divided into three parts: the tip (the free margin which provides the coaptation area to the corresponding neighbouring valve leaflets at the moment of the valve closure, avoiding regurgitation),

the “belly” and the base part of each leaflet[19]. There are also leaflet attachments that are inserted in the wall of the aortic root, being often named “the annulus”[19].

The sinuses of Valsalva or aortic sinuses are three bulges of the aortic wall being limited proximally by the leaflets attachments and distally by the sinotubular junction[19]. The aortic sinuses are responsible for maintaining the coronary artery blood flow, allowing the creation of vortices. These vortices are beneficial for the valve durability, leading to stress reduction on the aortic leaflets[19]. Associated with each commissure each point of the leaflets attachments lies one of three interleaflet triangles[19].

The interleaflet triangles are triangular extensions of the left ventricular outflow tract[20]. These triangular areas are bounded by the semilunar attachments of the leaflets[1] (Figure 2.1C).

The sinotubular junction (STJ) is the distal part of the sinuses toward the ascending aorta, being the structure that separates the aortic root from the ascending aorta[20]. The dilatation of the sinotubular junction is the cause of aortic insufficiency[19].

The “annulus” or “hemodynamic ventriculo-arterial junction” represents the separation level of ventricular and arterial hemodynamics[19].

2.1.2. Dynamics of the aortic root

Physiologically, the pressure drop across the aortic valves determines the resistance of the valve to the blood flow in the cardiac cycle and can be calculated as the difference between two pressures: the aortic and the left ventricular pressure[15,21] (Figure 2.2).

During systole, the pressure in the left ventricle exceeds the aortic pressure, consequently the aortic valve opens (being the pressure drop across the valve like a jet) and then the blood exits the left ventricle into aorta[14,21]. At the end of systole, there is a drop of pressure in the left ventricle and the aortic pressure leads to the aortic valve closure[14,21]. During diastole, it occurs the coaptation of each cusp against the other two cusps - when the valve is closed[14,21].

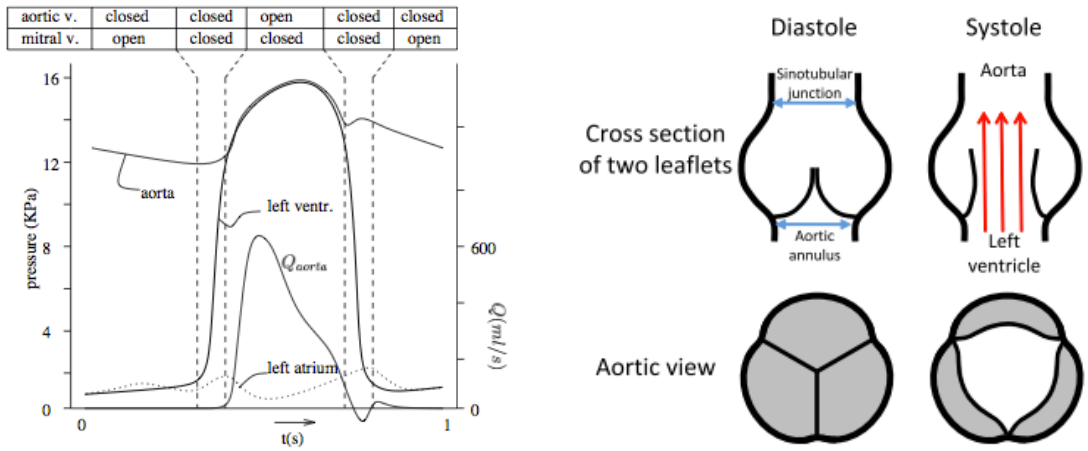

Figure 2.2. Pressure in the left ventricle, left atrium and aorta during one cardiac cycle and its relation with closure and opening of the aortic valve[21] (left). Illustration of an aortic valve closed, in diastole, and opened, in systole (right)[14].

2.1.3. Histology and tissue biomechanics of the leaflets

The anatomy of cells and tissues is important to understand the aortic valve physiological behavior and its pathological alterations[2]. The main cells present in heart valves include: the interstitial cells and the endothelial cells[22]. The interstitial cells are phenotypically of smooth muscle cells, cardiac muscle cells or the fibroblasts cell types. These cells are responsible for the production of glycosaminoglycans (GAGs) to retain water and to damping the mechanical forces and the viscoelastic properties of the valve[22,23]. The endothelial cells cover the surface of the leaflets with a continuously layer, being the alignment of the cells orthogonal to the blood flow[22].

The cross-sectional structure of the leaflets is thin, flexible (during the cardiac cycle) and can be divided into three layers: fibrosa, spongiosa and ventricularis[24] (Figure 2.3). Fibrosa, the thickest of the three layers, presents a highly dense network of collagen type-I fibers[22]. The elastin in the fibrosa forms a highly organized network of filaments, being a highly elastic protein media which stores energy during the loading of the valve and releasing it to the collagen during unloading[22]. Spongiosa, the middle layer, consists of highly hydrated glycosaminoglycans (GAGs), proteoglycans (PGs) and also presents collagen and elastin[22]. This “buffer” layer absorbs the load and transfers it to the elastic aortic wall to provide the minimum stress on the leaflet[22]. Ventricularis, the thinnest of the three layers,

consists of a collagen fiber network and elastin sheets[22]. This tri-layered structure ensures the high tensile strength for resisting the high transvalvular pressures and the low flexural stiffness as required for normal opening of the valve[22]. This is the result of the fibers orientation principally in the circumferential direction, because cusp is stiffer along the circumferential direction compared to radial direction[22].

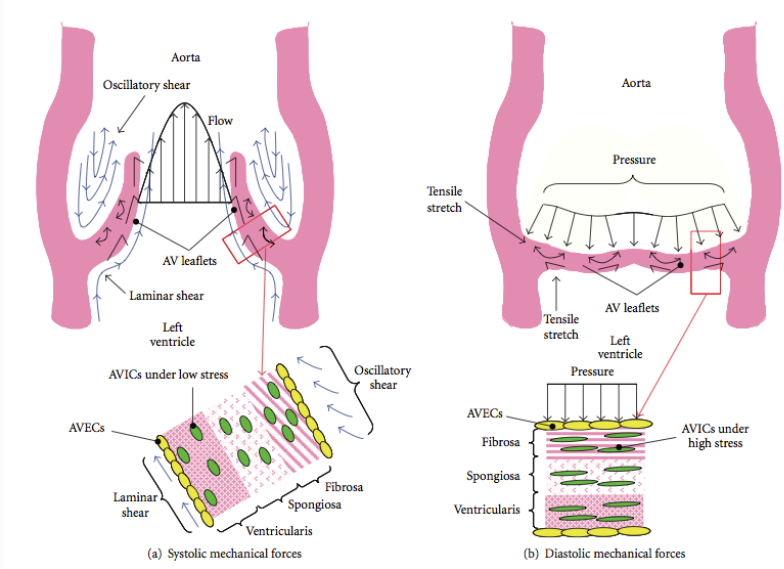

Figure 2.3. Schematic of mechanical forces experienced by the layers of the aortic valve during peak systole and peak diastole and correspondent effect of these forces on the leaflets[25].

Biological soft tissues exhibit a multi-axial non-linear stress-strain relationship and, consequently, large variability in mechanical properties are verified[26]. However, there is a lack of biaxial test data on fresh healthy human valve leaflet specimens[13]. Previous studies have reported the anisotropic material property for the aortic tissue leaflets based on bi-axial load-deformation data from pericardial bioprosthetic[9] and fresh porcine aortic tissue[27], respectively.

After explaining the fundamental medical aspects of the aortic valve it is crucial for this study to describe in the next section the correspondent pathological condition of aortic valve, BAV.

2.2. Bicuspid Aortic Valve

The earliest documented interest in the anatomy of the BAV stems from Renaissance, where Leonardo Da Vinci sketched the bicuspid variant more than 400 years ago[3,4,28]. In 1844, Paget identified the first pathological anomaly[3]. In 1858, Peacock noted the tendency of these valves to develop obstructive lesions (such as severe calcific aortic stenosis)[3].

2.2.1. Prevalence

BAV is one of the most prominent congenital heart valve defects, prevalent in 1%–2% of the general population, between a 2:1 and 4:1 males:females ratio[3–7,29]. This condition can be sporadic, genetic (familiar occurrence of BAV is verified in 9% of first-degree relatives, FDRs), or associated with aortic aneurysm syndromes[4]. Carmona et al. (2013) developed a prospective study of 100 consecutive families of BAV patients with different morphologies, and verified that the hereditary transmission of morphologic BAV types happens by chance and that the aortic dimensions in tricuspid aortic valve in the FDRs are normal[30]. There are yet doubts if the inheritance pattern of BAV is considered to be autosomal dominant or polygenic[30]. In terms of genetic theories for the abnormal valve structure, we emphasize that:

(i) BAV is associated with a high prevalence of calcific aortic valve disease (CAVD), due to the formation of calcific lesions on the leaflets, which contributes to the obstruction of the left ventricular outflow and progressive heart failure[17,31];

(ii) Aortopathy may be associated with BAV disease, leading to coarctation of the aorta, ascending aortic dilation (more than 50% of bicuspid adults have aortic dilatation[30]), aortic dissection or aneurysm formation[32,33].

33% of patients with a BAV may experience vascular complications (aortic stenosis, aortic regurgitation, an increased risk for infective endocarditis), and, consequently, require surgical

intervention[4,7,32,34–36]. BAV disease carries the highest risk of morbidity and mortality[37], lifelong surveillance of the aortic valve and aorta is required[4,7,32,34,35].

BAV prevalence at the Santa Marta Hospital

Santa Marta Hospital provided some data about their BAV patients. From our analysis, we summarize some aspects related with age, gender, leaflet fusion and pathological condition in Table 2.1.

Table 2.1. Data from BAV patients from the Santa Marta Hospital.

BAV Pacients from Santa Marta Hospital		
Age	<= 30	35%
	>30	65%
Gender	Female	26%
	Male	74%
Leaflet fusion	Fusion R-L	58%
	Without raphe	96%
	Fusion R-NC	37%
	Fusion L-NC	5%
Aortic Calcification	Yes	84%
	No	17%
Aortic Insufficiency	No	29%
	Mild	40%
	Moderate	28%
	Severe	2%
Aortic Stenosis	No	57%
	Mild	17%
	Moderate	10%
	Severe	16%
Aortic Dilatation	Normal	65%
	Asc.	23%
	Asc. And Ao. root	11%
	Ao. root	1%
Average dimensions (mm)	Sinus of Valsalva	32.42
	Sinotubular junction	29.1
	Ascending Aorta	37.8

We observed 82 BAV patients, with an average age of approximately 36 years old, being 74% (61 patients) from male gender. We concluded that patients have more predisposition to develop R-L fusion (58% of total population), without raphe (96%). We observed the following pathological

condition: 84% (68 patients) present tendency to develop aortic calcification; 40% (33 patients patients) present a mild aortic insufficiency; 57% (47 patients) have no aortic stenosis; 65% (53 patients) have a normal aortic condition; the average age for aortic the dilatation is 43 years old and the average age for absence of aortic dilatation is 33 years old.

Regarding the velocities, it was verified an average maximum velocity of 2.54 m/s, being observed that 13% of BAV patients have maximum velocities greater than 4 m/s. All of these patients present aortic calcification and a severe degree of aortic stenosis, and predispose to aortic insufficiency (mild, 40%; moderate, 20%).

2.2.2. Embryology

The development of the aortic valve is complicated and not yet completely understood[28], but it is known that the heart begins as a single tube, separates into two tubes and "begins to twist rightward onto itself"[28]. The semilunar valves originate from mesenchymal outgrowths (also called as cardiac cushions) that are located along the ventricular outflow tract of the heart tube[3,4,28].

The exact mechanism for the BAV development is unclear[4], but Sans–Coma and colleagues revealed, based on histologic assessments of Syrian hamster embryos, that the fusion of the right and left valve cushions at the beginning of valvulogenesis appears as a key factor in BAV formation[3,4,28,38].

There are different etiologies for the BAV fusion: "fused right and non-coronary leaflets results from a morphogenetic defect before cardiac outflow tract septation on the basis of an exacerbated nitric oxide-dependent epithelial-to-mesenchymal transformation" (Fernández et al. (2009)) and "fused right and left leaflets results from anomalous septation of the proximal portion of the cardiac outflow tract, with origin in a dysfunctional behavior of the neural crest cells" (Fernández et al. (2009))[39–41]. Compared with the patients with tricuspid aortic valve, it was verified a molecular abnormality in the extracellular matrix, with a deficient fibrillin-1 content in the vasculature of the BAV patients[4,32,38]. An inadequate fibrillin-1 production during valvulogenesis may disrupt the formation of the aortic cups and the result is a BAV and a weakened aortic root - with aortic dilatation[32,38,42] (Figure 2.4).

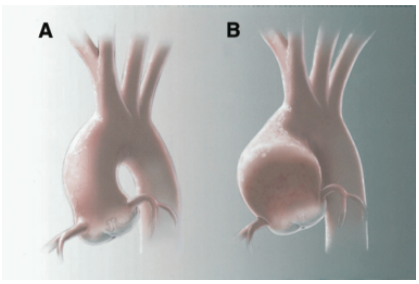

Figure 2.4. Representation of a normal aortic root (A) and a dilated aortic root (B)[32].

2.2.3. BAV anatomy, respective classification and pathology

BAV anatomy includes typically two inequal-sized cusps, due to the fusion of two cusps resulting in one larger cusp, instead of three cusps as in a TAV (Figure 2.5.)[4,37]. This larger cusp presents a central raphe (a fibrous ridge), which corresponds to a joint segment of two underdeveloped cusps extending into the commissural area. This raphe is identifiable in most BAV patients[5,37].

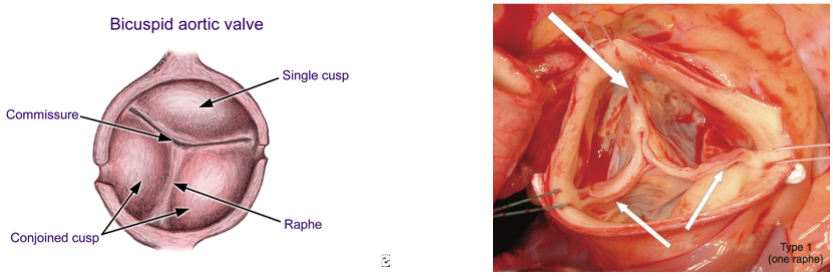

Figure 2.5. Left: BAV anatomy[43]. Right: Intraoperative picture of a BAV with left-right cusp fusion, where small arrows represent the two completely developed commissures and the large arrow represent the raphe[5].

Sievers and Schimidtke (2007) have classified BAVs in accordance with the valve characteristics: number of raphes, the spatial position of cusps or raphes, functional status of the valve (Table 2.2)[5]. The main category to classify the BAVs is termed “type” which represents the number of raphes: type 0 (valve with no raphe); type 1 (valves with one raphe) and type 2 (valves with two raphes)[5]. Surgical pathology studies demonstrated that 97% of BAVs include asymmetric cusps and rarely the cusps are symmetrical (case known as “pure” BAV) or there is no raphe[3,37].

Table 2.2. Schematic presentation of the development phenotypes of the aortic valve and typical characteristics[5].

Valves Classification		Tricuspid	Bicuspid		
Functional characteristics	**No. of cusps**	3	2	2	2
Morphological characteristics	**No. of raphes**	0	 0	 1	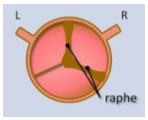 2
	No. of cusps	3	2 *Purely bicuspid	2 under and 1 fully developed *Potentially tricuspid	
	Size of cusps	Equal	Equal	Non-equal	
	No. of commissures	3	2	1 under and 2 fully developed	2 under and 1 fully developed

Empirical observations based on the surgical and imaging exams findings show that morphologic patterns of a BAV vary according with the commissures fusion. Each type of fusion may be predictive of clinical outcomes, in the distinct forms of proximal aortic lesions in BAV patients[6,35,44] – and leaflets orientation may be predictive of aortic elastic properties[23].

Schaefer et al. (2008) identified three morphologies of BAV related with distinct fusion patterns (Figure 2.6): (i) fusion of right and left coronary cusps; (ii) right and non-coronary cusp fusion; (iii) left and non-coronary cusps. After surgical observation it was verified that fusion of the left and right coronary cusps occurs in 70%-86% of the cases (more common in men)[6]. This can be associated with a coarctation of the aorta. However, in general, the patients presented a larger dimension of the aortic root, an increased wall stiffness at the sinuses of Valsalva, and a smaller diameter at the aortic arch (with no difference in stiffness)[3,5,20,23,25]. This fusion pattern has a higher risk of aortic dissection that may result in aortic regurgitation from progressive root dilatation[45]. A second pattern is the right and non-coronary cusp fusion that occurs in 15%-30% of cases[6]. It is associated with a relative degree of

valve dysfunction (aortic stenosis or regurgitation), presenting ascending aortic dilatation and a larger aortic arch dimensions, leading to an intervention during childhood[4,6,37,46,47,25]. A third pattern is the fusion of the left and non-coronary cusps that occurs in 3% of cases[5,6,46].

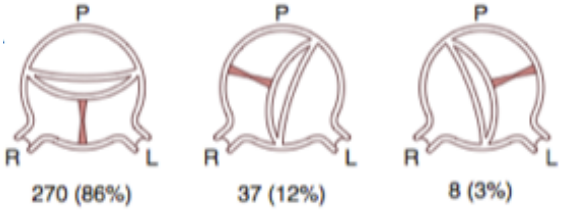

Figure 2.6. Classification of BAV: relative position of raphe and conjoined cusp in 315 bicuspid aortic valves. First: Fusion of RL. Second: Fusion of RP. Third: Fusion of PL. L=Left Coronary Cusp, P=Posterior Cusp/Non-coronary cusp and R=Right Coronary Cusp[46].

Table 2.3. presents aortic dimensions according to the degree of valve dysfunction (stenosis, regurgitation), where it is possible to observe the great diameters of BAV in relation to the TAV.

Table 2.3. Aortic dimensions according to BAV pathology[48].

Components	BAV				TAV	
	Normal Valve (n=21)	Valve Stenosis (n=28)	Valve Regurgitation (n=13)	P value	Normal valve (n=6)	P value
Annulus (cm)	2.40±0.20	2.60±0.45	2.50±0.33	>0.2	2.20±0.30	0.040
Sinus of Valsalva (cm)	4.10±1.10	4.00±0.53	4.20±0.75	>0.2	3.45±0.80	0.007
Sinotubular junction (cm)	3.90±1.00	3.70±0.70	3.90±0.90	>0.2	3.25±0.60	0.003
Ascending Aorta (cm)	5.30±0.28	5.10±0.58	5.20±0.40	0.153	5.70±0.70	>0.2

Possible hypothesis for previous clinical outcomes (the different fusion patterns, Figure 2.6) described are specific genetic defects, differences in spatial distribution of blood with inhomogeneous distribution of shear forces or pressures that, consequently, contribute to an abnormal flow development in the ascending aorta, with distinctive alterations of the proximal aortic wall[6,45]. In fact, it has been demonstrated that:

(i) Significant differences in the expression and spatial distribution of the extracellular matrix (ECM) proteins have been found in clinical cases of BAV with stenosis (associated with asymmetrical dilatation of the mid-ascending aorta and a normal aortic root diameter) and BAV insufficiency (associated with aortic root dilatation)[6].

(ii) Abnormal turbulence effects contribute to increase the susceptibility to BAV degeneration, where the leaflets of the BAVs demonstrate folding or wrinkling during the cardiac cycle[49]. With aging, BAVs presents an accelerated process of calcification which involves calcium and lipid deposition, neoangiogenesis, inflammatory cell infiltration and the development of fibrosis (Figure 2.7 e 2.8), being patients with left coronary and right coronary cusps the most predisposed to this process[3,6,34]. The advanced stage of CAVD involves the formation of calcium nodules on the leaflet aortic surface (fibrosa)[1].

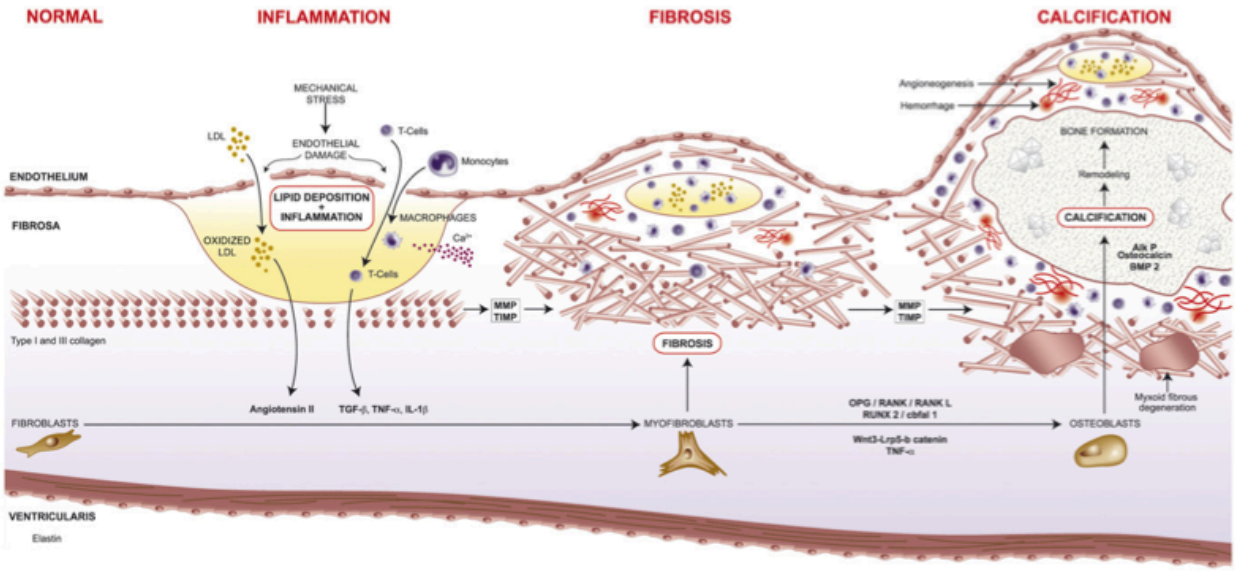

Figure 2.7. Mechanical stress leads to endothelial damage allowing infiltration of lipid and inflammatory cells into the aortic valve. Lipid oxidation increases the inflammatory process, promoting the secretion of cytokines. Latter there is the differentiation of fibroblasts into myofibroblasts, having the secretion of angiotensin. There is the action of metalloproteinases (MMPs) and respective inibitors, with fibrous tissue accumulating within the tissue, leading to thickening and stiffness of the valve. First there is the development of a microcalcification; but with the differentiation in myofibroblasts into osteoblasts, the calcification accelerates. Osteoblasts coordinate the calcification of the valve[51].

Different types of morphologic cusp fusion of BAV and respective blood flow pattern were analyzed *in vivo* using 4D magnetic resonance imaging (MRI)[52]. Hope (2010) verified the transvalvular systolic flow pattern as well the abnormal helical flow patterns in patients with BAV – that results in the specific orientation of systolic flow jets in the proximal aorta[52]. In what concerns the abnormal systolic flow pattern, it may be implicated with BAV and associated aortopathy, and not only related with a dilated aorta or aortic valve stenosis[52]. Note that the stenosis is caused by the stiffning of the leaflet tissue which imposes a pressure overload on the left ventricle, that can lead to the heart failure[1]. Helical flow patterns are verified in most common cusp fusion: the left coronary and right coronary cusps fusion produces a right-anteriorly directed eccentric systolic flow jet (that may be linked to asymmetric dilatation of the mid-ascending tubular aorta), and the fusion of the right coronary and non-coronary cusps produces a left posteriorly directed eccentric flow jet (possibly explaining the increased aortic arch)[52]. Particularly, the eccentric systolic flow can determine the specific pattern of segmental aortic root aneurysm formation of BAV patients and, consequently, they can develop aortic root insufficiency - being the degree of this pathology dependent on the dilatation of the sinotubular junction or the annulus[6,52]. The dilatation allows the transmission of the stress from the cusps to the aortic wall, and it is a consequence of higher stresses in the cusps (having a loss of equilibrium between the blood pressure forces and the wall forces)[52]. The aortic root aneurysm can cause aortic root insufficiency[15]. During aortic insufficiency, the large stroke volume causes wide pulse pressure with a rapid rise and fall, but when the turbulence energy density is higher, there is an elevated shear stress, leading to the damage of red blood cells, platelets and the endothelial cells on the surface of the tissues[25]. Thus, it is extremely important the quantification of Wall Shear Stress (WSS), which is the stress induced by blood flowing over the valve or the luminal side of the vascular wall[54,53].

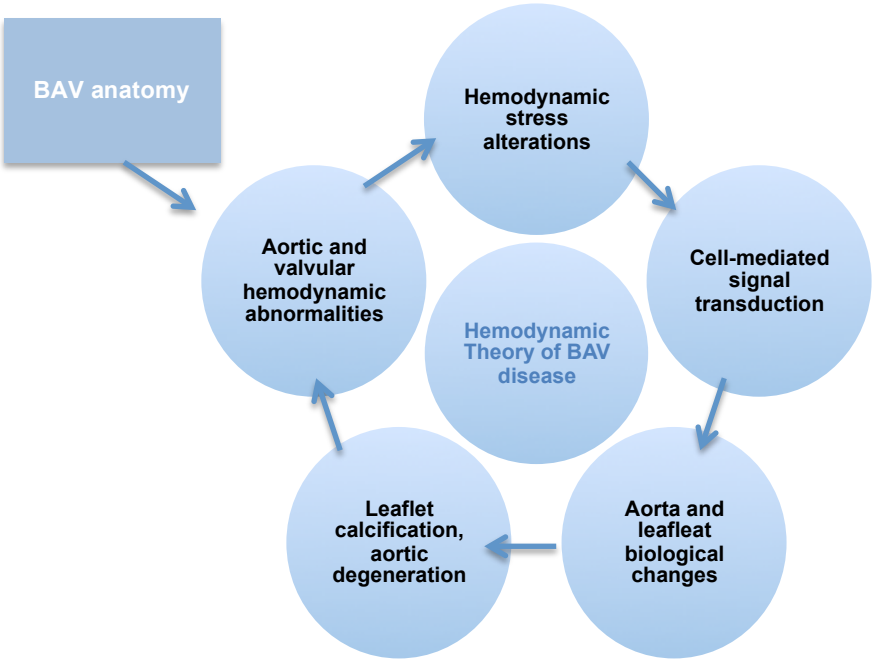

Figure 2.8. Hemodynamic theory of BAV disease[1] (Adaptation from Atkins, 2013).

2.3. Imaging Methods used in Patient Specific Modeling

Pacient-specific modeling is always desirable, but it's hard to define a 2D or a 3D geometry for a living human valve[15]. With the imaging modalities (Ultrasound, Computed Tomography-CT and Magnetic Resonance-MRI) and with the progress in image processing techniques it is possible to obtain the patient-specific morphological images[13]. Grande et al (1998) used MRI measurements of excised human aortic and root specimens, and Sirois et al. (2011) obtained a 3D geometry of an aortic root and valve from CT scans (with 64 number of slices)[55]. In this sense to reproduce a geometry 2D slices are captured and then, with measures of the valves, the patient-specific models are constructed. The problem is that the aortic valve is constantly in movement and synchronization with electrocardiography is needed[15]. Using patient-specific geometries it is possible to obtain correlations between the abnormal stresses computed in the numerical simulations and the respective alterations in the leaflets[13]. A BAV patient-specific simulation can be performed at a given time and the follow-up examinations can be performed on the patient to determine, for example, the location of any subsequent leaflet calcification. This approach can improve the clinical treatment[13].

2.3.1. Echocardiography

Echocardiography, known as *cardiac ultrasound*, is used for measurements of the aortic root and the ascending aorta (Figure 2.9), but also for the pathology detection and follow-up[2,56]. This non-invasive method uses standard ultrasound techniques to get the image of two-dimensional slices of the heart. It may provide morphologic information of cardiac tissue at any arbitrary point and hemodynamic information (the velocity of blood)[2]. Continuous wave Doppler ultrasound allows the knowledge of cardiac valves according with their function: (i) investigating the leaking of blood through the valve (valvular regurgitation), (ii) information about abnormal communications between the left and right side of the heart, (iii) calculation of the cardiac output, (iii) ejection fraction[2]. It becomes possible to determine the severity of valve dysfunction by the use of hemodynamic indices (peak ejection velocity, effective valve orifice area, mean transvalvular pressure gradient)[2]. Despite the advantages of the method, a 2D view does not give a complete representation of the aortic root geometry and may for example underestimate the largest annular dimension[56]. To perform measures with more accuracy, this method can be combined with a computed tomography (CT) exam.

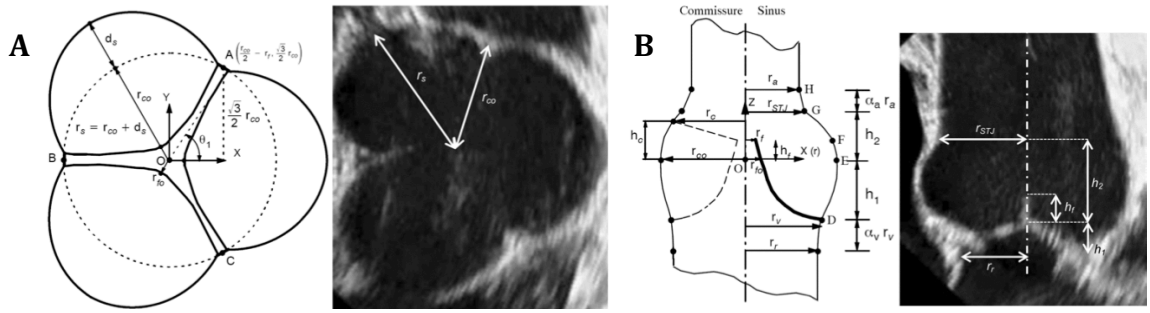

Figure 2.9. Schematic aortic valve representations in different planes (A. z=0 plane, left; B. y=0 plane, right) and respective echocardiographic measurements[15].

2.3.2. Computed tomography imaging

A computed tomography (CT) scanner uses ionizing radiation (X-rays), and the exam consists in the use of intravenous injections of contrast agents, which contain elements of a high atomic number (iodine or barium) relative to the surrounding tissue. CT corresponds to a diagnostic tool to examine tissue composed of elements of a higher atomic number than the tissue surrounding them (for

example, bone or calcifications within the body)[56]. CT scanner corresponds to a ring that has one or more X-ray sources and opposing detectors rotated rapidly around the patient (which moves axially through the scanner), producing projections from multiple fan beams (equally spaced two-dimensional cross sections, the slices) allowing a volumetric three dimensional reconstruction[2]. CT provides precise diameters with respect to the different components of the aortic root (aortic annulus, sinuses of Valsalva, sinotubular junction) and the ascending aorta (Figure 2.10), but also, qualitative information about cusp morphology and symmetry of the sinuses[56]. These measurements should be performed using an electrocardiogram to a synchronized detection with the heartbeat[2].

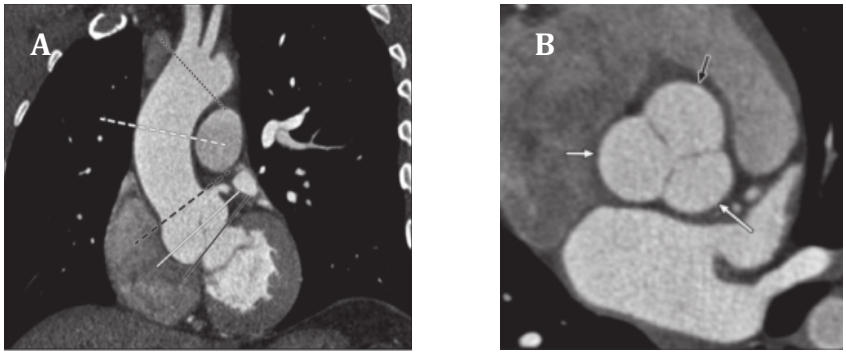

Figure 2.10. CT images: (A). Coronal CT image with landmarks reported for measurement: aortic annulus (solid black line), aortic sinuses of Valsalva (solid white line), sinotubular junction (dashed black line), mid ascending aorta (dashed white line) and high ascending aorta (dotted black line)[55]. (B). CT image of aortic sinuses: left (long white arrow), right (black arrow) and non-coronary (short white arrow)[55].

2.3.3. Magnetic resonance imaging

Magnetic resonance (MR) uses non-ionizing radio frequency (RF) signals to acquire images. The MR imaging scanner requires a magnetic field of 1.5 to 3 Tesla (T), which corresponds to 30 000 to 60 000 times the strength of the Earth's magnetic field[56]. This powerful magnetic field is used to align the magnetization of atoms in the body and the RF fields to alter the alignment of this magnetization to the nuclei producing a rotating magnetic filed which is detectable by the scanner[2]. The detectable information is used to construct an image of the body's region of interest, being this method suitable for soft tissue, bones, and also other calcium-based body components[2].

MR images are acquired in frequency space, being obtained by inverse Fourier transforms which

require long time scans to traverse the whole frequency space. One benefit of MRI in young patients is that they can suspend respiration for 25-35 seconds (a long scanning time), allowing a spatial resolution similar to the CT images[56]. MR has the potential to visualize BAVs in the entire cardiac cycle. The steady-state free precession (SSFP) sequence is an MRI pulse sequence used for assessing valve anatomy and motion (Figure 2.11) that offers a good contrast between blood pool and vessel wall or myocardium, a high signal-to-noise ratio[55,57]. SSFP produces a 2D image in any plane having multiple frames along the cardiac cycle[57]. To obtain less artifacts and a high resolution, one possible approach in the image acquisition, along several cardiac cycles, is combined with the ECG[55].

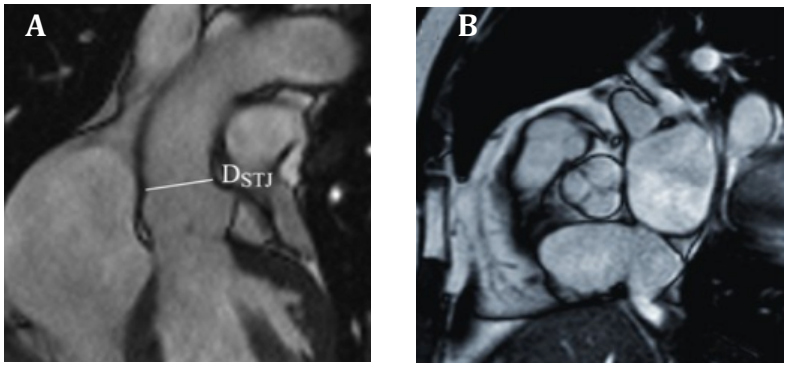

Figure 2.11. MRI images of the aortic root in different axis analysis[2]: (A). long-axis. (B). short-axis

.

2.4. Computational Methods

Computational methods provide new tools for physicians that help the medical planning[16,58]. With them it is possible to improve in accuracy the understanding of anatomical and physiological BAV disease, which may vary from patient to patient, with different morphological variants of congenitally bicuspid aortic valve[27,59]. Computational Fluid Dynamics (CFD) and FSI methods, using Finite Elements (FE), have been implemented for the identification of stress pattern distribution and mechanics of the aortic root of the valves, to clarify the researchers about failure mechanisms and also allow the improvement of future prosthetic valve designs (the main applications)[8,10,11,60–63].

2.4.1. Finite element modeling (FEM) studies

FE method is a numerical technique used to approximate solutions of partial differential equations (PDEs)[65]. The FE approach involves: (i) a division of the whole domain into disjoint parts, where the domain (the valve) is represented as a collection of simple domains – the geometrical component of the finite elements connected by nodes; (ii) a derivation of approximation functions (often algebraic polynomials) over each element; (iii) the assembly of elements, which is based on the continuity of the solution and the balance of internal fluxes[65].

FE methods have been used in the numerical modeling of physiologic valves. The first studies analyzed the complex behavior of the aortic valve structure (between the aortic root and its respective interaction with the leaflets).

Grande et al. (1998) published a FE study focusing on asymmetrical effects of the root and leaflet geometry of normal aortic valves in the end diastole configuration based on MRI patient data of nine subjects and the resulting study indicated asymmetries inherent to the valve[61,66]. The constitutive material model employed was of the linear type, with Young modulus of 334 kPa and 6885 kPa for the leaflets and the aortic root, respectively. Thickness of the tissues was assigned physiologically with values taken from literature. It was found that peak stress values were located in the non-coronary leaflet and lowest in the left leaflet, 538 kPa and 410 kPa, respectively.

Gnyaneshwar et al. (2002) presented a FE dynamic analysis to investigate the effect of leaflet and aortic root interaction on valve function, beginning in the mid-systole configuration for the entire cardiac cycle[8]. This analysis employed shell elements and used linear elastic material properties, where the aortic root had an elastic modulus twice larger than that of the valve leaflet, 2 MPa[8]. This study showed that the expansion of the aortic root helps in the opening of the leaflet and it is most important at the beginning of systole[8]. The maximum Von Mises stresses during opening and closing were 30kPa and 800kPa, respectively, being located in the leaflet attachment regions - which are clinically relevant because they are commonly associated with tearing, calcification, and valvular failure[8].

Kim et al. (2007) presented a dynamic FE simulation analysis with a morphologically and physiologically realistic material specification for the leaflets using a Fung-elastic constitutive model for in-plane and bending responses[62]. This study investigated the complex bioprosthetic heart valves (BHV) deformations and stress distributions throughout the cardiac cycle (during the opening and closing phases). The purpose was to understand the concentration of the mechanical stress and large flexural deformation that is closely related to the calcification and tissue degeneration in BHV, to help in the development of tissue caused valve substitutes[62].

There are also computational studies focused on asymmetric BAV models using FE analysis to understand the stress distribution on the leaflets with the valve in the fully closed position. Consequently, it allows to conclude about the common regions of the calcification phenomena and also of the structural valvular failure[8,9,13].

Conti et al. (2010) made a dynamic FE simulation – where they verified a right/left fusion BAV (BAV type I) to demonstrate that BAV opened asymmetrically with an elliptic orifice[13,67]. To construct the geometry, valve dimensions were obtained through measurements from patient MRI data acquired from 8 normotensive and also healthy subjects with functional bicuspid aortic valves[67]. Thus, it was possible to construct a 3D model of the normal aortic valve root and leaflet structures and to employ the same technique to generate a BAV model[67]. Conti reported that restricted BAV cusp motion due to the fusion of the right and left cusps results in systolic flow deflection towards the right anterolateral ascending aorta - this reinforces the idea that BAV geometry motivates pathologies in the aortic wall[52,67]. Conti reinforced that the abnormal leaflet stress in the BAV geometry may play a role in tissue remodeling contributing for an early leaflet degeneration[67].

Jermihov et al. (2011) performed a FE analysis, using dimensions published in the literature to construct idealized TAV and BAV geometries. Jermihov employed for the leaflet material data obtained from the fresh porcine aorta valve experiments[27]. This study had the purpose of investigating the effect of geometric variations, between TAV and BAV geometries, with respect to the strain and stresses developed in the valves[27]. It was found that BAVs have higher stresses compared with TAVs

and it was also reported that BAVs present a smaller opening area in the fully open position, as it was previously reported by Conti et al. (2010)[27,67].

To verify the effect of flow in the cusps of the BAV on the aortic root and on the ascending aorta computational fluid dynamics based on FSI analysis was used[13]. Robicsek et al. (2004) conducted in vitro experiments using cryopreserved aortic root with BAV. This study demonstrated an excessive folding and creasing of the leaflets during a cardiac cycle and showed an asymmetrical flow pattern distal to the valve[49]. The results showed that BAVs are subjected to abnormally high stresses, leading to an early thickening[49].

2.4.2. Fluid structure interaction

FSI simulations are based on structural and fluid dynamic solvers that allow for the numerical simulation of the pressure load on the aortic root and on the cusps[17,68]. The FSI method used here is based on an ALE formulation to analyze the structural deformation and the fluid flow through computational fluid dynamics and FE Analysis[68]. This method will be explained in Chapter 3 (Methodology).

FSI analysis has been limited by non-physiological leaflet material properties, because realistic mechanical properties for the leaflets and for the physiological flow regimes represent a computational challenge[13].

In relation to the aortic valve study, Hart et al. (2003) conducted a FSI analysis in 3D including leaflet mechanical and blood flow data on an aortic valve and using an isotropic Neo-Hookean material model[63]. Hart et al. (2003) focused mainly on the closing behavior during the diastolic phase (but also in the kinematic opening and closing during the systolic phase) of the cardiac cycle, where the maximum Von Mises stresses computed during the cardiac cycle were 12kPa (in the opening phase) and 60kPa (in the closing phase)[63]. Hart et al. (2003) showed that during systole the leaflets of the valve were moving with the fluid in an essentially kinematical process governed by the fluid motion.

The maximum Reynolds number (900) was far from the expected physiological value (4500), was a limitation to the FSI capabilities[11].

Several studies employed FSI models to investigate the clinical aspects of the congenital BAVs[67-70]. Weinberg and Mofrad et al. (2008) employed 3D FSI models using the "operator split" Lagrangian and Eulerian approach to solve the conservation equations. In this formulation, the Eulerian calculation of the conservation equations is separated into Lagrangian and advection steps: in the first Lagrangian step the mesh moves with the flow, and in the second advection step the mesh is remapped to the original Eulerian position and the flow between adjacent cells is calculated by the advection algorithm[14]. This method was used to investigate the hemodynamics in BAVs, but their BAVs had a rare symmetric geometry[70,71]. Investigating the pathological condition of BAV, Weinberg et al. (2008) proposed a multiscale model for BAV and TAV: BAV model with leaflets of two equal sizes and TAV were numerically modeled by a set of FSI simulations to describe the cell, tissue and organ length scales[70]. These time dependent models incorporate nonlinear constitutive equations of the valve leaflet tissue. Weinberg et al. (2008) observed differences between TAV and BAV at the organ scale: the BAV shows greater flexibility in the solid phase and stronger jet formation in the fluid phase and at the cell scale the region of interest is verified on the wrinkling of the fibrosa[70]. This study supports the assertion that the difference in calcification observed in the BAV versus TAV (essentially in terms of organ level) may be due to the geometric difference between the two types of valves[70].

Katayama et al. (2012) analyzed the influence of the morphologic characteristics of the BAV on its disease progression. In this study the Navier-Stokes equation was described in ALE coordinates and to avoid distortion they applied an automatic mesh algorithm developed by their group. They considered the fibers alignment on a symmetric BAV: in one leaflet, the fibers were aligned as in the normal TAV model and, in the other leaflet, the fibers were aligned as if two separate leaflets were fused together[14,71]. Katayama concludes that BAV morphology creates an excessive bending strain on the leaflets during the ventricular ejection[71] – and showed the evidence that mechanical stresses may influence a rapid influence of the BAV disease, essentially due to the pressure gradients verified[71].

Chandra et al. (2012) examined the asymmetric effect on different anatomies of BAVs and compared the BAV results with TAV, using 2D FSI methods based on an ALE approach[17]. This study supports the existence of a mechano-etiology of CAVD in the BAV, showing the ability of abnormal fluid shear stress to trigger valvular inflammation, leading to a smaller opening area in BAVs[17], and consequently to the increase of the velocity magnitudes[17,71].

Marom et al. (2013) employed FSI models using a Cut-Cell method approach (created by their group) and they compared several morphologies: a trileaflet valve, two BAVs with asymmetric anatomy, and a symmetric BAV (Figure 2.12). In this method the mesh is adapted automatically to the moving boundaries by a recursive subdivision of each cell into identical cells. The results found are in agreement with the study of Chandra et al. (2012)[17]. It was verified a larger opening area in the TAV during systole; at the peak systole, larger vortices were found in BAVs compared to the TAV model, while the asymmetric configuration led to larger vortices near the larger leaflet. The location of the vortices in the BAVs was also closer to the leaflets than in the TAV model. The closer vortices and the smaller opening, which lead to higher velocities, probably caused the larger flow shear stresses on the leaflets of BAVs, and consequently, there is predisposition to the calcification process[14,25].

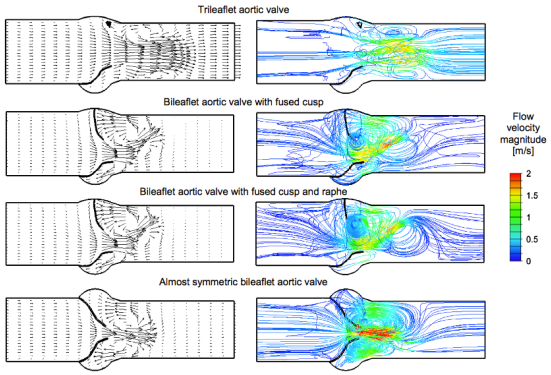

Figure 2.12. Comparison between TAV and three types of BAV in terms of velocity vectors and instantaneous streamlines at peak systole[68].

Espino et al. (2014) developed a 2D FSI model based on an ALE formulation of a BAV with symmetric and asymmetric cusps (with and without the aortic arch), during the systolic phase[73]. Espino concluded that the flow patterns were dependent of cusps asymmetry and material properties[73].

CHAPTER 3

Methodology

Chapter 3 illustrates the Fluid Structure Interaction (FSI) modeling approach with the presentation of the respective problem definition and governing equations. Toward the use of the numerical methods, we will describe the construction process of seven 2D geometries (an idealized geometric model of TAV and six 2D patient specific BAV models), on COMSOL Multiphysics (v. 4.4)[18]. Then, we will present different aspects involving the model: acquisition data (in case of BAVs models), selection of material properties, boundary conditions, convergence study, as well the solver properties applied to the different numerical simulations. Finally, we will briefly present the construction process of a 3D idealized TAV geometry, on Solidworks, and we will give a brief description of the implementation on COMSOL Multiphysics.

3.1. Fluid Structure Interaction (FSI)

The dynamic interaction of the heart valve with the blood is important to understand mechanical aspects related with the velocity field, deformations, stresses, pressure gradients in the valve structure during the cardiac cycle[59]. The dynamic behavior of the valve, namely its opening and closing motion, is a delicate process between the surrounding fluid (blood) and the structure (aorta and valve flexible leaflets). Some aspects compromise the blood-valve interaction modeling, interfering with a good performance of the numerical analysis of the heart valve operating under physiological conditions. These complications are focused on the large differences between the material properties of the fluid and the structure, but they are also due to the complex motions of the valve leaflets[64].

3.1.1. Problem definition and governing equations

The fluid structure coupling will be discussed, as well as a description of the techniques to solve the resulting set of equations for a 2D model of a flexible leaflet. A two dimensional representation of the valve is shown in Figure 3.1, where two flexible leaflets are immersed in a pulsatile flow within a rigid channel. This channel has a certain height and length, and contains a sinus cavity in the middle (orifice). A flexible leaflet with length, and thickness is attached to the top wall, before the sinus cavity.

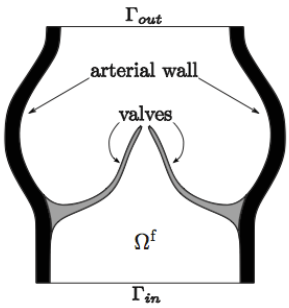

Figure 3.1. Representation of the computational model[59].

However, before describing the mathematical model adapted to Figure 3.1, it is important to focus our attention in the fluid properties.

- **Blood flow behavior**

Blood is a complex fluid that consists of cellular deformable elements: erythrocytes, leuckocytes and platelets. It has high concentration of erythrocytes contributing to the mechanical properties of blood. This fluid has many vital functions (it mainly delivers oxygen and nutrients to all tissues, drains metabolic waste products, defends the body against infection, transports hormones through the vascular system). Blood is an isothermal (at a temperature of 37ºC) and incompressible fluid, and it is commonly assumed to be a Newtonian fluid[11]. However, this last assumption is not valid everywhere in the circulatory system[15]. Blood has a non-Newtonian behavior (with shear thinning, thixotropic and viscoelastic properties) in small vessels and a Newtonian behavior in the large arteries (as in the case of aorta)[11,59,74]. In this study blood will be modeled as a Newtonian fluid, verifying the Newton's law of

viscosity, which states that:

$$\tau = \mu \, . \gamma \tag{1}$$

where τ is the shear stress, γ is the strain rate and μ is the viscosity (constant of proportionality). The specific properties applied for blood are the density ρ^f and the viscosity.

In fact, in the vascular system, fully developed flows are difficult to achieve. There is the Poiseuille solution (steady flow) and the Womersley solution (time-periodic flow, adequate to describe the rhythmic mechanical pumping of the heart). However, blood flow is often considered in the steady state (simpler than to assume the unsteady state), being approximated by the Poiseuille solution (with a parabolic velocity profile and flow direction parallel to the wall).

$$u(r) = u_{max}\left[1 - \left(\frac{r}{R}\right)^2\right], 0 \leq r \leq R \tag{2}$$

$$\Delta p = \frac{8\mu Q l}{\pi R^4} \tag{3}$$

The Poiseuille solution of a steady flow is defined by equation (2) (Figure 3.2), and the respective Poiseuille law is given by equation (3). In equation (2), u_{max} is the maximum velocity placed in the central layer and R is the radius. The Poiseuille law, given by equation (3), establishes a relation between steady flow and pressure gradient, being l the tube length, Q the flow rate and μ the fluid viscosity.

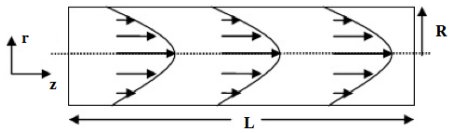

Figure 3.2. Laminar flow developed with a parabolic profile.

Blood is assumed to be a laminar flow, because the velocity field is parallel to the vessel centerline, except during the systole and in disease conditions, where the flow can exhibit turbulent features (recirculation regions, vortices). Note that blood flow becomes turbulent when the Reynolds number, given by equation (4) is larger than 2000 (verified in the end of systole, or in pathological conditions).

$$Re = \frac{\rho u D}{\mu} \tag{4}$$

where u is the average velocity, D the tube diameter, ρ the density and μ the dynamic fluid velocity.

- **Arbitrary Lagrangian Eulerian (ALE) formulation**

Before describing this formulation, we introduce the following notations related with the kinematics of continuum media[73]: (i) let $\widehat{\Omega} \subset \mathbb{R}^3$be a given reference configuration (the initial state) of a body and a family of one-to-one (time parametrized) mappings: $\hat{\varphi}: \widehat{\Omega} \times \mathbb{R}^+ \rightarrow \mathbb{R}^3$; (ii) for each particle or material point $\hat{x} \in \widehat{\Omega}$, $\hat{\varphi}\,(\hat{x}, t)$ will be its position at time t; (iii) in Figure 3.3., $\Omega(\mathrm{t}) \stackrel{\text{def}}{=} \hat{\varphi}(\widehat{\Omega}, t)$ is the current configuration of the body; (iv) the trajectory, the displacement and the velocity field are defined in equations (5), (6), (7), respectively.

$$\mathcal{T}_{\hat{\varphi}} \stackrel{\text{def}}{=} \mathrm{U}_{t \in \mathbb{R}^+} \Omega(t) \times \{t\} \tag{5}$$

$$\hat{d}\,(\hat{x}, t) \stackrel{\text{def}}{=} \hat{\varphi}(\hat{x}, t) - \hat{x} \tag{6}$$

$$\hat{u}(\hat{x}, t) \stackrel{\text{def}}{=} \frac{d\hat{\varphi}}{dt}(\hat{x}, t) \tag{7}$$

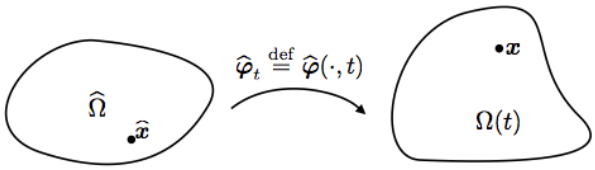

Figure 3.3. Kinematics of continuum media[74].

When modeling fluid structure interaction, the fluid is described with respect to an Eulerian reference frame (where the material moves through the computational domain)[21] and the structure is described with respect to a Lagrangian reference frame (where the computational domain moves with the material)[64,74]. Note that the Lagrangian field is defined in $\widehat{\Omega} \times \mathbb{R}^+$ and the Eulerian field is defined in $\Im_{\hat{\varphi}}$. Figure 3.4, A and B illustrates the Eulerian description of a Lagrangian field and a Lagrangian description of an Eulerian field, respectively. Note also that the Eulerian description of the velocity is given by: $u(x, t) \stackrel{\text{def}}{=} \hat{u}(\hat{\varphi}^{-1}(x), t)$.

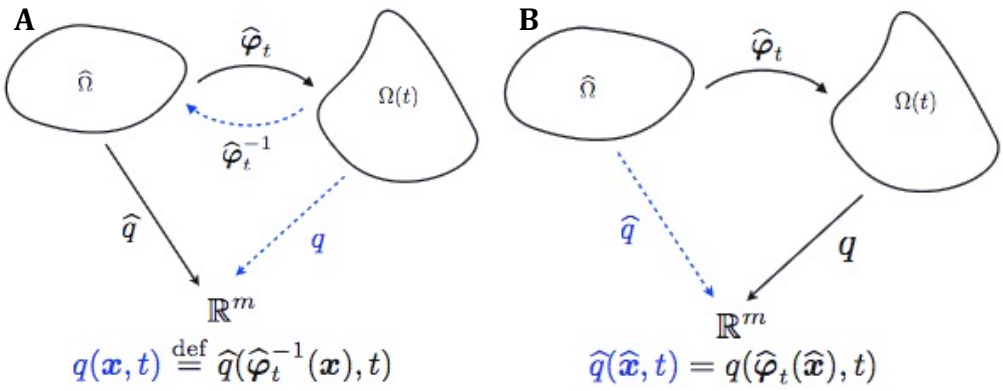

Figure 3.4. Illustration of: (A) Eulerian description of a Lagrangian field. (B) Lagrangian description of an Eulerian field[74].

One way of coupling the problems for the fluid and the structure is to use an Arbitrary Lagrangian Eulerian (ALE) formulation. The ALE method, developed in the early 70's by Hirt et al. (1974)[21], has three reference systems: (i) a spatial reference system (which is fixed, following an Eulerian description); (ii) a material reference system (which moves with the material, following a Lagrangian description); and (iii) a computational reference system (which moves according with the prescribed displacement). In this work, the finite element formulation is performed according with a computational reference system – ALE formulation.

The ALE description (Figure 3.5) involves a moving control volume $w(\mathrm{t})$ (equation (8)) with $\hat{\mathcal{A}}: w \times \mathbb{R}^+ \rightarrow \mathbb{R}^+$ the motion of the control volume (the ALE map). The trajectory of the moving control volume, the ALE description of the motion in terms of u and the velocity of the volume control are defined by equations (8) - (11), respectively.

$$w(\mathrm{t}) \stackrel{\text{def}}{=} \hat{\mathcal{A}}(w,t) \tag{8}$$

$$\mathcal{T}_{\hat{\mathcal{A}}} \stackrel{\text{def}}{=} \bigcup_{t \in \mathbb{R}^+} w(t) \times \{t\} \tag{9}$$

$$u: \mathcal{T}_{\hat{\mathcal{A}}} \rightarrow \mathbb{R}^3 \tag{10}$$

$$\widehat{w}(\mathrm{t}) \stackrel{\text{def}}{=} \frac{d\hat{\mathcal{A}}}{dt} \tag{11}$$

In equation (11), in general $\widehat{w} \neq \hat{u}$. However, we have $\widehat{w}$=0 according to the Eulerian description, and $\widehat{w}$=$\hat{u}$ according with the Lagrangian description.

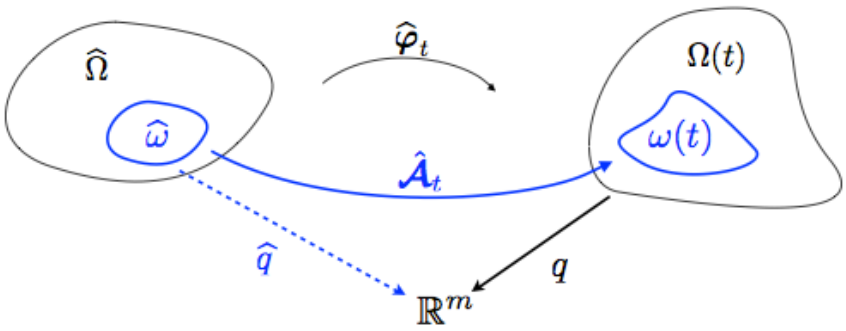

Figure 3.5. Arbitrary Lagrangian Eulerian (ALE) description[74].

Let q: $\mathcal{T}_{\hat{\varphi}} \rightarrow \mathbb{R}^3$ be an Eulerian field. Its Eulerian-time derivative and its Lagrangian-time derivative are defined by equations (12) and (13), respectively.

$$\frac{dq}{dt}(\boldsymbol{x},t), \forall\, \boldsymbol{x} \in \Omega(t) \tag{12}$$

$$\frac{Dq}{Dt}(\boldsymbol{x},t) \overset{\text{def}}{=} \left.\frac{\partial \hat{q}(\hat{x},t)}{\partial t}\right|_{\hat{x}=\widehat{\varphi_t}^{-1}(x)} = \frac{d}{dt} q(\hat{\varphi}(\hat{\boldsymbol{x}},t),t)\Big|_{\hat{x}=\widehat{\varphi_t}^{-1}(x)} \tag{13}$$

On the other hand, the ALE time derivative is defined as:

$$\frac{\partial q}{\partial t}(\boldsymbol{x},t) \overset{\text{def}}{=} \left.\frac{\partial \hat{q}(\hat{x},t)}{\partial t}\right|_{\hat{x}=\widehat{\mathcal{A}_t}^{-1}(x)} = \frac{d}{dt} q(\hat{\varphi}(\hat{\boldsymbol{x}},t),t)\Big|_{\hat{x}=\widehat{\mathcal{A}_t}^{-1}(x)} \tag{14}$$

and consequently is:

$$\left.\frac{\partial q}{\partial t}\right|_{\hat{\boldsymbol{x}}} = w \cdot \boldsymbol{\nabla q} + \frac{\partial q}{\partial t} \tag{15}$$

where $\left.\frac{\partial q}{\partial t}\right|_{\hat{x}}$ is the ALE-time derivative, $w \cdot \nabla q$ is the transport term and $\frac{\partial q}{\partial t}$ is the Eulerian-time derivative.

The ALE formulation involves a continuous adaptation of the mesh[63], allowing movements of the mesh in a Lagrangian way[21]. This method is not easy to implement and its computational cost depends on the problem in hands. Moreover, it presents large translations or inhomogeneous movements, and consequently the grid becomes ill-shaped, decreasing the accuracy of the solution[21]. Considering the heart valves there are large deformations of the thin leaflets within the computational fluid domain, and this behavior leads to difficulties in the mesh adaptation process[63]. Remeshing can be performed if the mesh quality degenerates too much. However, remeshing introduces artificial diffusivity, leading to a lack of sufficient robustness and accuracy[21,64].

- **Fluid structure interaction based on the ALE formulation**

We have used COMSOL Multiphysics (v.4.4)[18] for FSI model based on the ALE approach, between fluid and structures to obtain simulations in domains with moving boundaries. Regarding the theoretical concepts, the fluid domain is denoted by Ω^f and the structural domain by Ω^s.

The conservation of momentum and conservation of mass (continuity) equations, which govern the blood motion, Ω^f, are given by

$$\rho^f \left(\frac{\partial \boldsymbol{u}}{\partial t} + \boldsymbol{u_{fluid}} \cdot \nabla \boldsymbol{u_{fluid}}\right) - div\ \sigma^f\left(\boldsymbol{u_{fluid}}, p\right) = 0, \text{in } \Omega^f, \tag{16}$$

$$div\ \boldsymbol{u_{fluid}} = 0, \text{in } \Omega^f$$

This is the unsteady Navier-Stokes system, where $\boldsymbol{u}$ represents the velocity of the fluid, p the pressure, and $\sigma^f\left(\boldsymbol{u_{fluid}}, p\right) = 2\mu \boldsymbol{D}\left(\boldsymbol{u_{fluid}}\right) - p\boldsymbol{I}$ corresponds to the Cauchy stress tensor, where $\boldsymbol{D}\left(\boldsymbol{u_{fluid}}\right) = \frac{1}{2}\left(\nabla \boldsymbol{u_{fluid}} + \nabla^T \boldsymbol{u_{fluid}}\right)$ denotes the strain tensor and $\boldsymbol{I}$ is the identity tensor. In terms of constants, there are the fluid density ρ^f (1010 kg/ m^3) and the viscosity μ (3.5x10^{-3} Pa.s). To solve the system (16) we need to impose initial conditions (t=0 in $\partial\Omega^f$), as well as conditions on the boundaries $\partial\Omega^f = \Gamma_{in} \cup \Gamma_{wall} \cup \Gamma_{out}$ of the fluid domain Ω^f.

$$\boldsymbol{p} = \boldsymbol{p_0},\ \left[\mu\left(\nabla \boldsymbol{u_{fluid}} + \left(\nabla \boldsymbol{u_{fluid}}\right)^T\right]\right] \cdot \boldsymbol{n}\ on\ \Gamma_{in} \subset\ \partial\Omega^f, \tag{17}$$

$$\left[-p\boldsymbol{I}\left(\nabla \boldsymbol{u_{fluid}} + \left(\nabla \boldsymbol{u_{fluid}}\right)^T\right)\right] \cdot \boldsymbol{n} = -\widehat{p_0} \cdot \boldsymbol{n}\ on\ \Gamma_{out} \subset\ \partial\Omega^f \tag{18}$$

$$\boldsymbol{u_{fluid}} = \boldsymbol{0}\ on\ \Gamma_{wall} \subset\ \partial\Omega^f, \tag{19}$$

At the inlet boundary, Γ_{in}, it was imposed a value for the pressure and no viscous stress, where $\boldsymbol{n}$ is the unit normal vector exterior to Γ_{in} (equation (17)). At the outlet boundary, Γ_{out}, it must be noted that $\boldsymbol{u_{fluid}} \cdot t = 0$, $\widehat{p_0} \leq p_0$ and $\boldsymbol{n}$ is the outward unit normal vector to Γ_{out}. (equation (18)). On the wall, Γ_{wall}, a *no-slip* boundary condition (equation (19)) has been imposed.

Until now we have only considered the fluid domain. Thus, related with the solid kinematics, let $\widehat{\Omega}^s$ be a given reference solid configuration, with a solid motion: $\varphi: \widehat{\Omega}^s \times \mathbb{R}^+ \rightarrow \mathbb{R}^3$ (see Figure 3.6.).

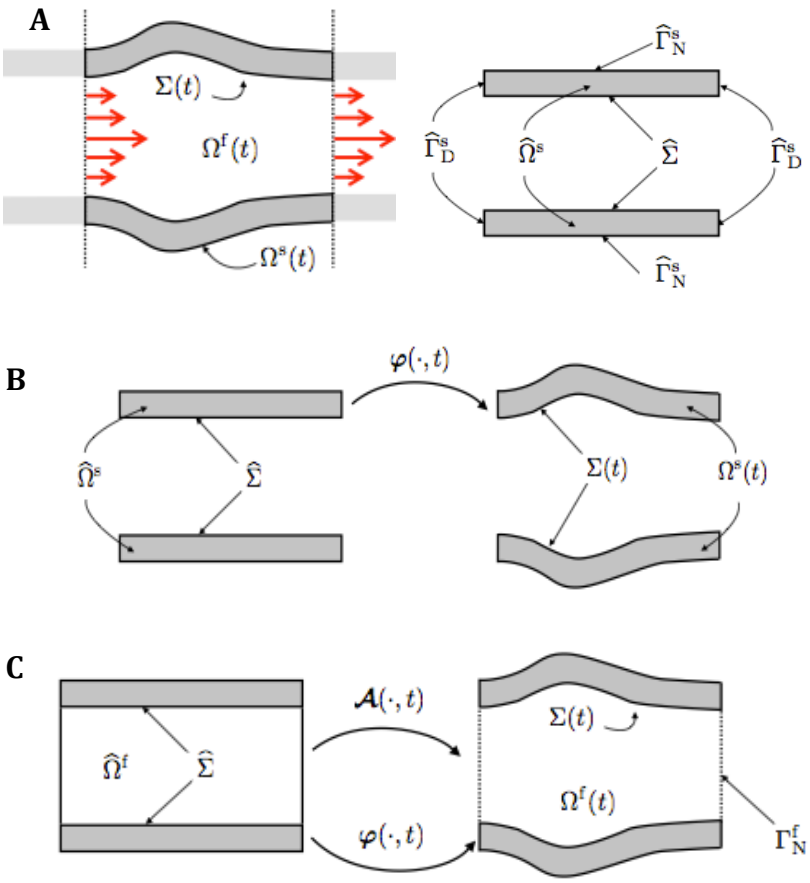

Figure 3.6. (A) Geometrical description of the blood flow (left side) and for the structure (right side). (B). Structure behavior. (C) FSI with the ALE approach[74].

FSI (based on an ALE approach) is a coupled problem for the fluid equations (system (20)) and the structure equations modeled as a linear elastic material (system (21)). This coupled problem is closed by appropriate interface conditions stating the continuity of the velocities and stresses in the coupling boundary (system (22)) (Figure 1). The ALE system is completed by the boundary conditions (17)-(19) and initial conditions in the fluid and the structure and we suppose that the structure is clamped at the inlet and outlet boundaries, to simplify.

$$\rho^f \left(\frac{\partial \boldsymbol{u}}{\partial t} + (\boldsymbol{u_{fluid}} - \boldsymbol{w}) \cdot \boldsymbol{\nabla u_{fluid}}\right) - \boldsymbol{div}\ \sigma^f(\boldsymbol{u_{fluid}}, p) = \mathbf{0}, \text{in } \Omega^f, \tag{20}$$

$$\boldsymbol{div}\ \boldsymbol{u_{fluid}} = 0, \quad \text{in } \Omega^f$$

$$\boldsymbol{\sigma}(\boldsymbol{u}, p)\boldsymbol{n} = \boldsymbol{g}, on\ \Gamma_N{}^f$$

where $\boldsymbol{w}$ is a new term (in relation to the first equation of system (16)), representing the velocity of the domain (ALE formulation).

$$\rho^s \frac{\partial^2 \boldsymbol{d}}{\partial t^2} - div\left(\boldsymbol{F}(\boldsymbol{d})\boldsymbol{S}(\boldsymbol{d})\right) = \mathbf{0}, \quad \text{in } \widehat{\Omega^s}, \tag{21}$$

$$\boldsymbol{d} = \mathbf{0}, \quad \text{on } \widehat{\Gamma_D^s},$$

$$F(\boldsymbol{d})S(\boldsymbol{d})\widehat{\boldsymbol{n^s}} = \mathbf{0}, \quad \text{on } \widehat{\Gamma_N^s}$$

$$\mathbf{u} = \boldsymbol{w}(\boldsymbol{d^f}), \text{ on } \Sigma(t), \tag{22}$$

$$\boldsymbol{F}(\boldsymbol{d})\boldsymbol{S}(\boldsymbol{d})\hat{n} = J\left(\boldsymbol{d^f}\right)\boldsymbol{\sigma}(\boldsymbol{u}, p)F(\boldsymbol{d^f})^{-T}\widehat{\boldsymbol{n}}, \text{ on } \widehat{\Sigma(t)}.$$

where d is the displacement, F is the deformation gradient, J the deformation Jacobian and S the second Piola-Kirchoff stress.

- **Hemodynamic indicators**

Hemodynamic indicators are important predictors to obtain a better understanding of the vascular diseases that affect the blood flow field near the wall[75]. The most relevant hemodynamic indicators are the Wall Shear Stress (WSS) and the respective derived measure, such as the Oscillatory Shear Index (OSI).

WSS is the tangential component of the Cauchy stress tensor (σ^f) on the wall, $\sigma^f\left(\boldsymbol{u_{fluid}}, p\right) = p\boldsymbol{I} + \boldsymbol{\tau}(\boldsymbol{u_{fluid}})$, where $\boldsymbol{\tau}(\boldsymbol{u_{fluid}})$ is the deviatoric tensor $\boldsymbol{\tau}\left(\boldsymbol{u_{fluid}}\right) = \boldsymbol{\tau}(\boldsymbol{u_{fluid}}, \boldsymbol{D}\left(\boldsymbol{u_{fluid}}\right))$, with $\boldsymbol{D}\left(\boldsymbol{u_{fluid}}\right)$ which denotes the symmetric part of the velocity gradient. WSS is given by:

$$WSS = \boldsymbol{\sigma_n} - (\boldsymbol{\sigma_n} \cdot \boldsymbol{n})\boldsymbol{n} = \boldsymbol{\tau_n} - (\boldsymbol{\tau_n} \cdot \boldsymbol{n})\boldsymbol{n} \tag{23}$$

where $\boldsymbol{n}$ is the unit normal vector exterior to the wall surface, $\boldsymbol{\sigma_n}$ and $\boldsymbol{\tau_n}$ are the normal components of the Cauchy stress tensor and the deviatoric tensor, respectively. OSI is a parameter used for unstationary flows, which measures the cyclic oscillatory nature or the directionality of the WSS at each point, having a correlation with residence time of the particles near the wall, given by:

$$OSI = \frac{1}{2}\left(1 - \frac{\left|\int_0^T WSS\, dt\right|}{\int_0^T |WSS|\, dt}\right) \tag{24}$$

where T is one cardiac period. OSI varies between 0 (purely unidirectional/pulsatile flow) and 0.5 (purely bidirectional/oscillatory flow).

- **Von Mises Stress**

Von Mises stress is related with the distortion energy failure theory, which compares two energies: (i) distortion energy in the actual case and (ii) distortion energy in a simple tension case at the time of failure. Von Mises Stress is denoted by σ_v, equation (25), where $\sigma_1, \sigma_2, \sigma_3$ are principal stresses defined in each direction (in relation to the deviatoric plane).

$$\left[\frac{(\sigma_1-\sigma_2)^2+(\sigma_2-\sigma_3)^2+(\sigma_3-\sigma_1)^2}{2}\right]^{\frac{1}{2}}=\sigma_v \quad (25)$$

Considering the failure theory, in a simplified way, failure occurs when the distortion energy in the actual case is greater than the distortion energy in a simple tension case at the time of failure.

$$\sigma_v \geq \sigma_y \quad (26)$$

3.2. Development of a TAV model

3.2.1. Construction of an idealized geometry

The construction of the TAV model was possible through the assessment to previous studies, explored by Chandra et al. (2012), Marom et al. (2012) and Espino et al. (2015)[15,17,73]. The TAV geometry was constructed on COMSOL Multiphysics[18], in *Geometry 1 Module*, using tools provided by this software. The parametric curve $\frac{1}{3}R\sin(\frac{pi}{2}R\ s)$ was used to draw each sinus of Valsalva. We used quadratic Bézier curves were used to construct the leaflets and rectangles to describe the rigid channels added to upstream (to mimic left ventricle) and downstream (to mimic the aorta) the TAV. To illustrate the thickness across the model we used lines. In the TAV model we applied *Geometry Operations* (such as, *Intersection*, *Mirror*, *Rotate*) and *Virtual Geometry Operations* (such as, *Ignore Edges* and *Ignore Vertices*). The length of the computational domain is 6.11 cm and the arterial diameter is 2.4 cm. The entry length and exit length are equal to 1.5 cm. Regarding the valve leaflet, the thickness is approximately 0.16 cm (on the leaflet base) and 0.06 cm (on the leaflet extremity), and the total length is approximately 2.71 mm. The orifice between the leaflets is approximately 0.1 cm.

The final computational domain corresponds to an aortic valve with a symmetric aortic root and leaflets, which can be observed in Figure 3.7.

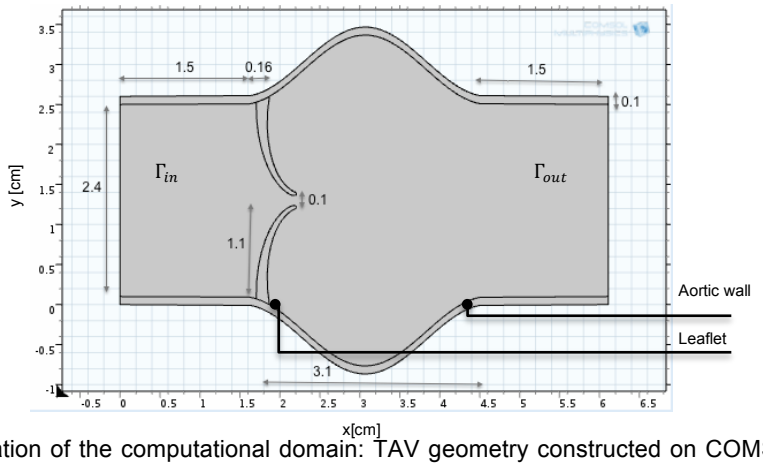

Figure 3.7. Representation of the computational domain: TAV geometry constructed on COMSOL Multiphysics. All measurements are in centimeters.

3.2.2. Materials

The material properties specification for the geometries is sparsely available through experimental data (from either porcine tissue or in rare cases from excised human tissue)[13]. Experimental studies of the mechanical behavior of porcine-aortic tissue show similar stress-strain behavior for major directions, leading to isotropic models. Material properties for the leaflets and the aortic wall of current idealized models are based on Conti et al.(2010), Marom et al. (2012), Chandra et al., (2012) and Espino et al. (2015) studies[15,17,67,73]. Leaflets were modeled as a linear elastic, nearly incompressible material. It must be noted that these material specifications, for the biologic tissue, as well for blood (mentioned in Section 3.1.1.), were inserted in the *Materials Module* but also in the *Fluid Structure Interaction Module*, on COMSOL[18].

Table 3.1. Properties of materials: cusps and aortic root of the TAV model.

Properties	Aortic root wall[15,17,67]	Leaflets[15,17,67,73]
Density (kg/m^3)	2000	1200
Poisson ratio	0.3	0.49
Young modulus (MPa)	2	0.37

3.2.3. Boundary conditions

The boundary conditions were inserted with the following path: in the *FSI* Module, we selected the *Laminar Flow* option, then we applied the most adequate boundary conditions (*Inlet*, *Outlet* and *Wall*). Boundary conditions used in previous FSI studies have been used to derive the appropriate boundary conditions for our case (Table 3.2).

Table 3.2. Boundary conditions considered in previous studies.

Boundary	Chandra et al. (2012)	Marom et al. (2013)	Yeh et al. (2013)	Espino et al. (2014)
Inlet	0 [mmHg]	80 [mmHg]	Physiological pressure profile [mmHg]	$v_{in} = v_p\left(\frac{t}{T}\right)$ [m/s] $v_p = 0.175\ m/s$
Outlet	Physiological pressure profile [mmHg]	0 [mmHg]	Physiological pressure profile [mmHg]	$P = P_0 + P_p\left(\frac{t}{T}\right)$ [mmHg] $P_0 = 80\ mmHg$ $P_p = 40\ mmHg$

After some tests with COMSOL[18], using the previous boundary conditions, we decided to use at the inlet a constant pressure of 0 mmHg as boundary condition and at the outlet the physiological pressure profile represented in Figure 3.8.B (which corresponds to two cardiac cycles, where each cardiac cycle has 0.8 s). It was used the Web Plot Digitizer program to obtain the coordinates that characterize the physiological pressure profile. Then using the *Curve Fitting Tool*, on Matlab, we obtained the function approximated by a Fourier series. This Fourier series was inserted on COMSOL[18], on *Global Definitions* section, as a *Piecewise Function*.

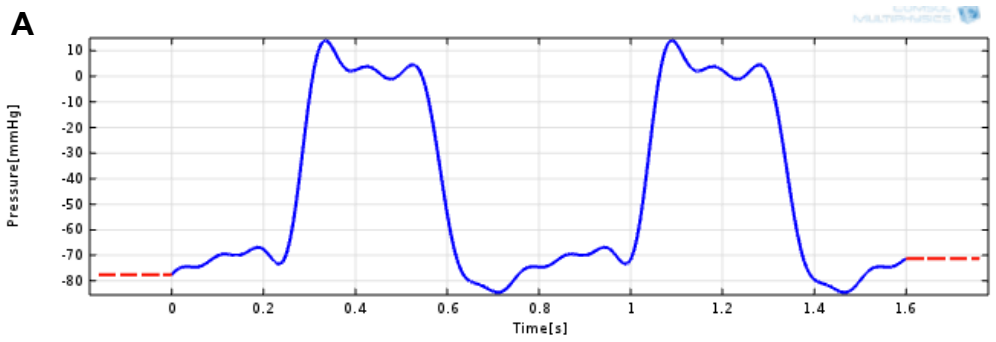

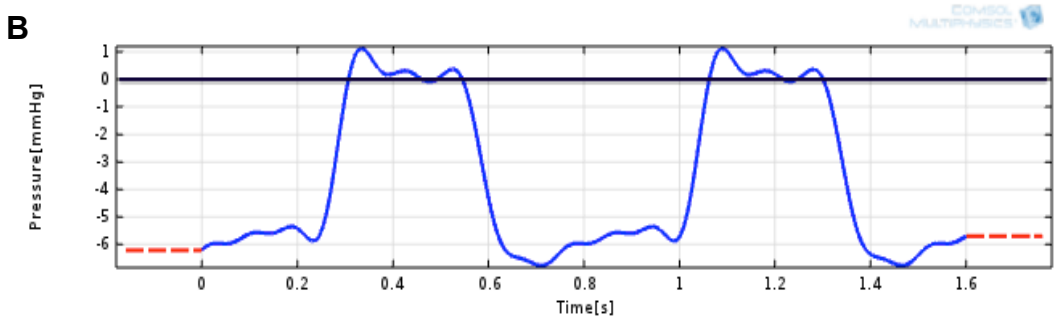

Figure 3.8. Boundary Conditions: A. Realistic outlet boundary condition representing the transvalvular pressure condition. B. Inlet (0 mmHg) and outlet boundary conditions (Physiologic Pressure Profile with two cardiac cycles), applied on *Comsol Multiphysics*.

3.2.4. Domains, constraints and smoothing adopted

In the *FSI* section, it was selected a *Time Dependent* study, where five different domains were used (one as the fluid domain, and other four domains for the valve leaflets and the aortic wall), which can be observed in Figure 3.9 A., as well the fixed constraints applied on the specific boundaries, Figure 3.9.B.

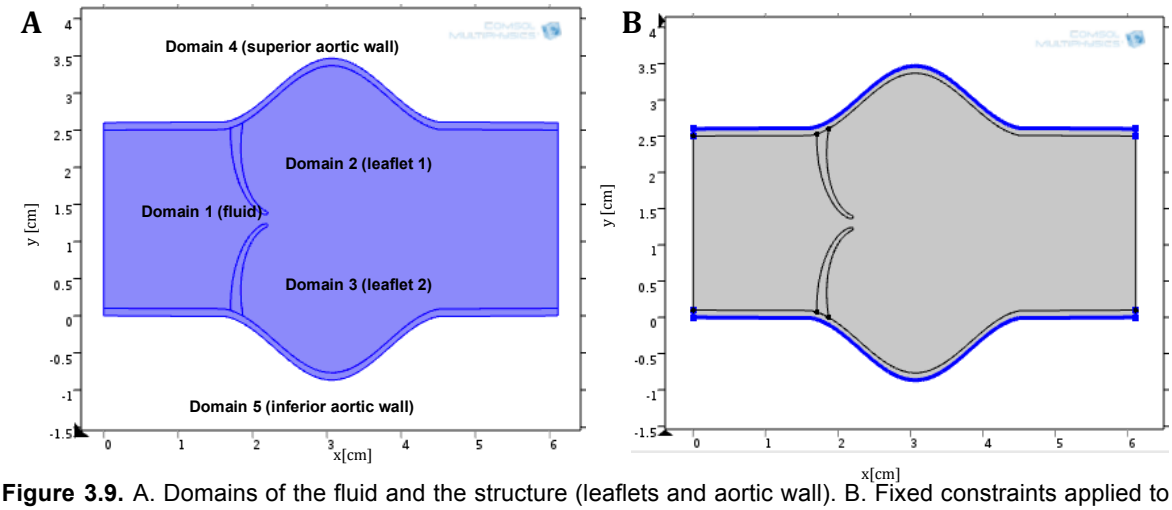

Figure 3.9. A. Domains of the fluid and the structure (leaflets and aortic wall). B. Fixed constraints applied to the computational domain.

In our geometry we have domains with free displacement, and the *Moving Mesh Interface* that solves an equation which smoothly deforms the mesh from the constraints placed on the geometry boundaries. In the *Free Deformation Settings* (*FSI* Module of the software COMSOL) we have used

the *Yeoh Mesh Smoothing,* which is inspired in hyperelastic materials, being a generalization of a neo-Hookean material, because it uses a strain energy of the form:

$$W = \frac{1}{2}\int_{\Omega} C_1(I_1 - 3) + C_2(I_2 - 3)^2 + C_3(I_1 - 3)^3 + \kappa(J - 1)^2 dV \quad (27)$$

where J and I_1 are invariants, given by the following equations:

$$J = \det(\nabla_X x) \quad (28)$$

$$I_1 = J^{-\frac{2}{3}} tr((\nabla_X x)^T \nabla_X x) \quad (29)$$

In equation (27), κ is an artificial bulk modulus, C_1 ,C_2 and C_3 are other artificial material properties. Note that C_1 is assumed by default as equal to 1; C_2 controls the nonlinear stiffness of the artificial material (which in this case was specified using a stiffness factor of 100) and C_3 is assumed by default as 0. In equations (28) and (29), x is the spatial coordinate in the spatial reference system.

The *Yeoh* smoothing method is nonlinear. It creates a single coupled system of equations in all directions, and for this reason it is computationally more expensive to solve them. This type of smoothing produces the best results, allowing the largest displacement of boundaries before mesh elements become inverted. However, due to this strong nonlinearity it can cause convergence problems, mainly, for time dependent studies (as in this case).

3.2.4. Mesh Generation

Table 3.3. and Figure 3.10 present information about the mesh generation for the TAV model, having a progressive manual refinement (with focus on the boundaries of the wall and leaflets) from mesh 1 to mesh 5.

Table 3.3. Mesh generation for TAV model.

Quality of mesh configuration	Total degrees of freedom solved	Number of mesh elements	Average element quality	Lagrange Element Type
Mesh 1	38766	12468	0.9612	Quadratic (Explained in Section 3.2.5)
Mesh 2	51124	17447	0.9642	
Mesh 3	61456	21526	0.9699	
Mesh 4	107213	33101	0.9702	
Mesh 5	215882	76522	0.9777	

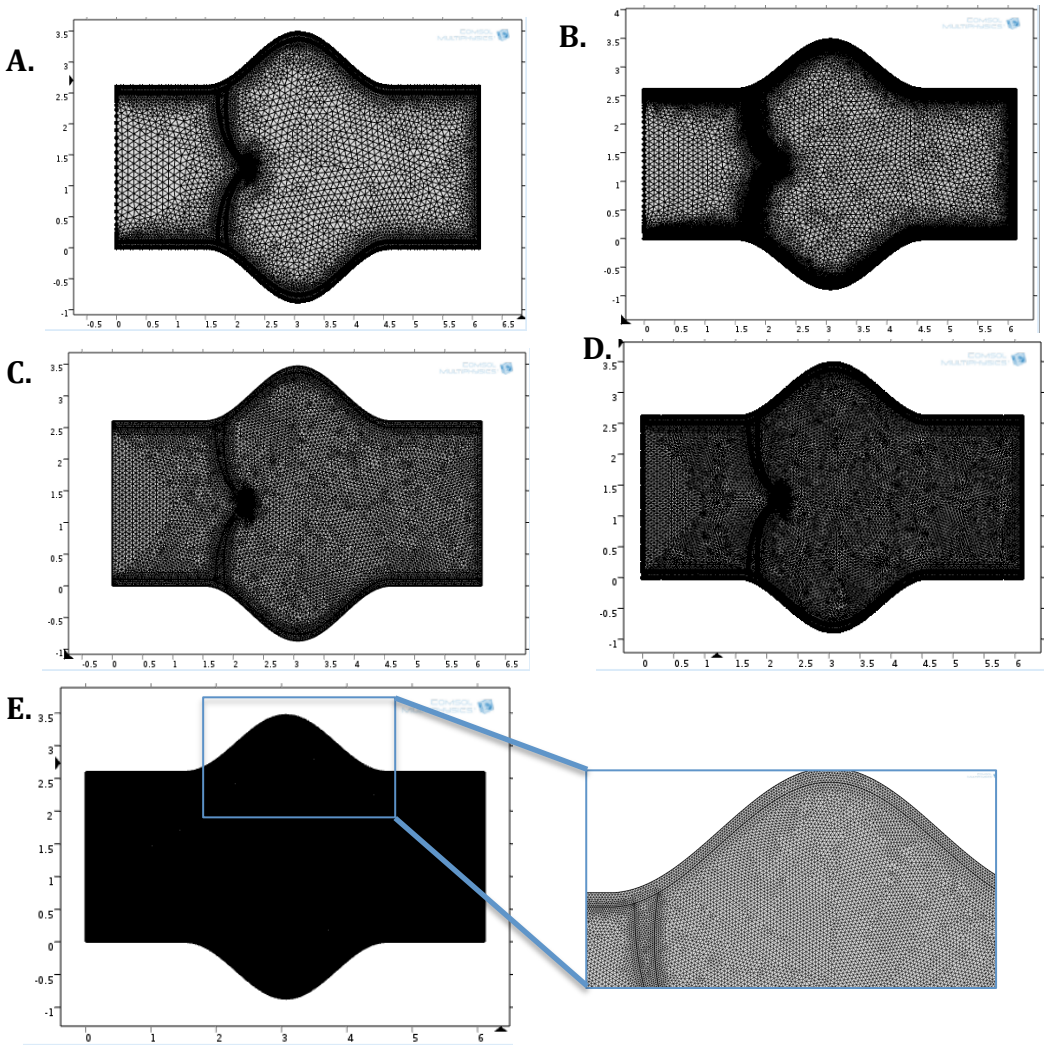

Figure 3.10. Mesh Generation applied to the TAV model: A. Mesh 1(Coarse), B. Mesh 2 (Normal), C. Mesh 3 (Fine), D. Mesh 4 (Finer), E. Mesh 5 (Extremely Fine) with a detail about the boundary layers. The dimensions of all geometries are in centimeters.

It must be noted the detail about the boundary layers in Figure 3.10. Boundary layers generate structured layers of elements along specified no-slip boundaries. Each boundary layer has a mesh with dense elements distribution. In 2D, a layered quadrilateral mesh is used, which is typical in the case of fluid flow problems. After the progressive mesh refinement, important for the numerical validation, we present the results of our convergence study.

3.2.5. Convergence Study

As already mentioned, the FEM is used to approximate the solution of PDE problems (briefly explained in Section 2.4.1 of Chapter 2). The FEM solution u_h will generate an error, in relation to the true solution u of the PDE. This error, $u - u_h$, can be quantified by the corresponding norm, where h is the mesh size of the FE mesh, and can be estimated by $\|u - u_h\| \leq C\, h^q$, where C is a problem-dependent constant independent of h, and q indicates the order of convergence of the FEM ($q = 1$ for linear convergence, $q = 2$ for quadratic convergence)[76]. Higher values of q are associated to a faster convergence. The convergence order of the FEM is dependent of the degree of the polynomial functions used in each finite element. The higher is the polynomial degree better is the convergence. COMSOL[18] uses Lagrange finite elements of degree *p* (with $p = 1, \ldots, 5$), which approximate the PDE solution at the nodes of each element of the mesh. Considering the norm in the L^2 (Ω) space and linear (degree p=1) Lagrange elements, it is expect an error such that $\|u - u_h\|_{L^2(\Omega)} \leq C\, h^2$ [76]. However, for Lagrange finite elements of higher degree ($p \geq 1$) it is expected an error of $\|u - u_h\|_{L^2(\Omega)} \leq C\, h^{p+1}$ [76] (as in the case of the current study).

In order to validate the FEM method, on COMSOL, an *Integral Probe* was used to evaluate the velocity magnitude. Figure 3.11. shows the respective results, having an evident convergence in temporal instants where the valve is closing (in 0.4s,0.5s,1.2s, 1.3s).

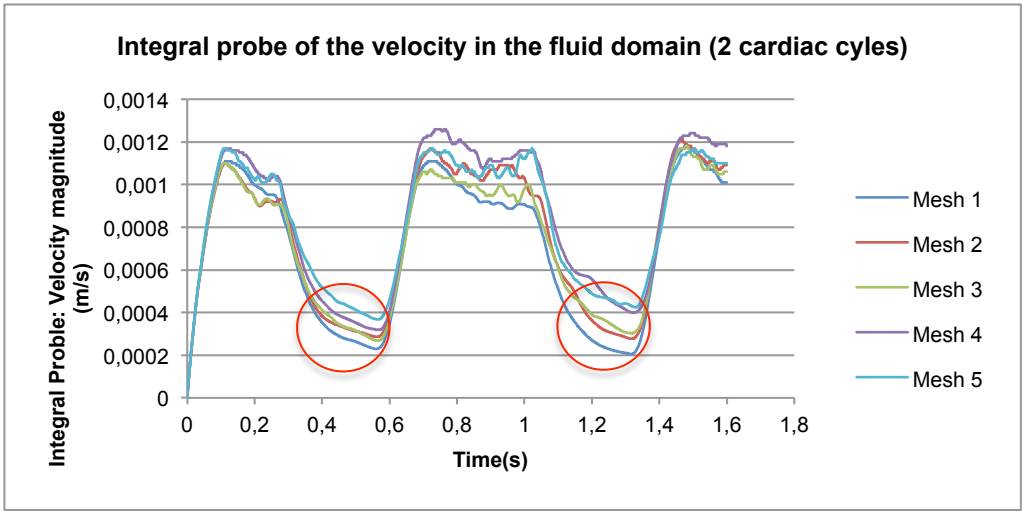

Figure 3.11. Convergence study: integral probe to evaluate the velocity in the fluid domain.

Figure 3.12.A. shows the convergence of the velocity field for the previous created meshes. Figure 3.12.B. shows the respective errors comparing the results obtained in the more refined mesh (mesh 5) with those obtained in other meshes. Consequently, it is observed that best results are obtained in meshes with more degrees of freedom (mesh 5-mesh 4, with relative errors between 6.41% and 14.54%), in comparison with less refined meshes (mesh 5-mesh 1, with relative errors between 31.9% and 52.4%).

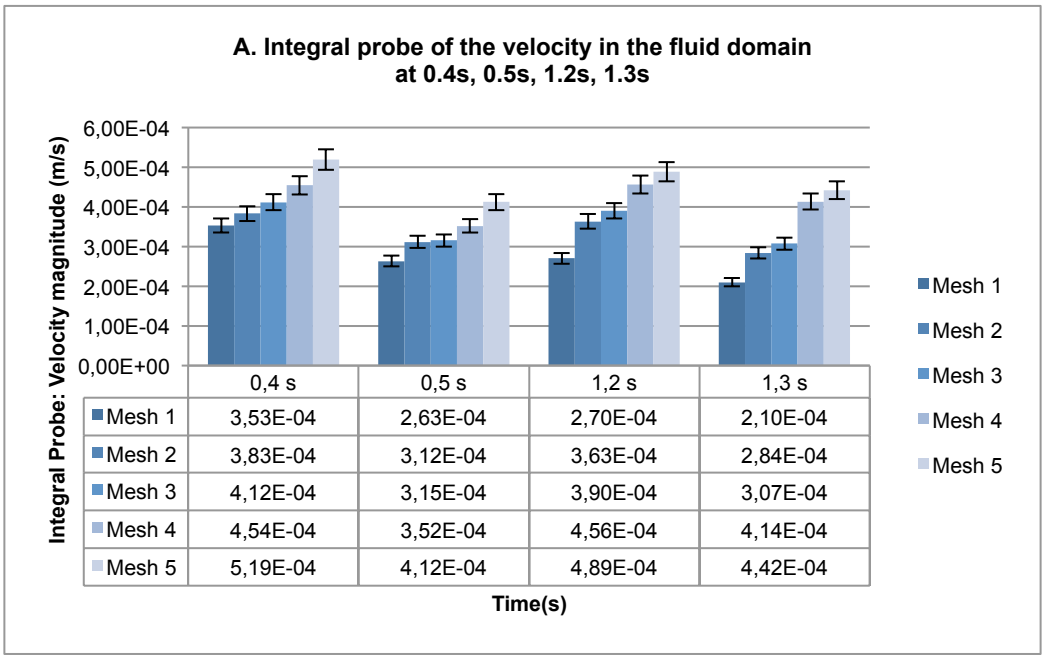

	0,4 s	0,5 s	1,2 s	1,3 s
Mesh 1	3,53E-04	2,63E-04	2,70E-04	2,10E-04
Mesh 2	3,83E-04	3,12E-04	3,63E-04	2,84E-04
Mesh 3	4,12E-04	3,15E-04	3,90E-04	3,07E-04
Mesh 4	4,54E-04	3,52E-04	4,56E-04	4,14E-04
Mesh 5	5,19E-04	4,12E-04	4,89E-04	4,42E-04

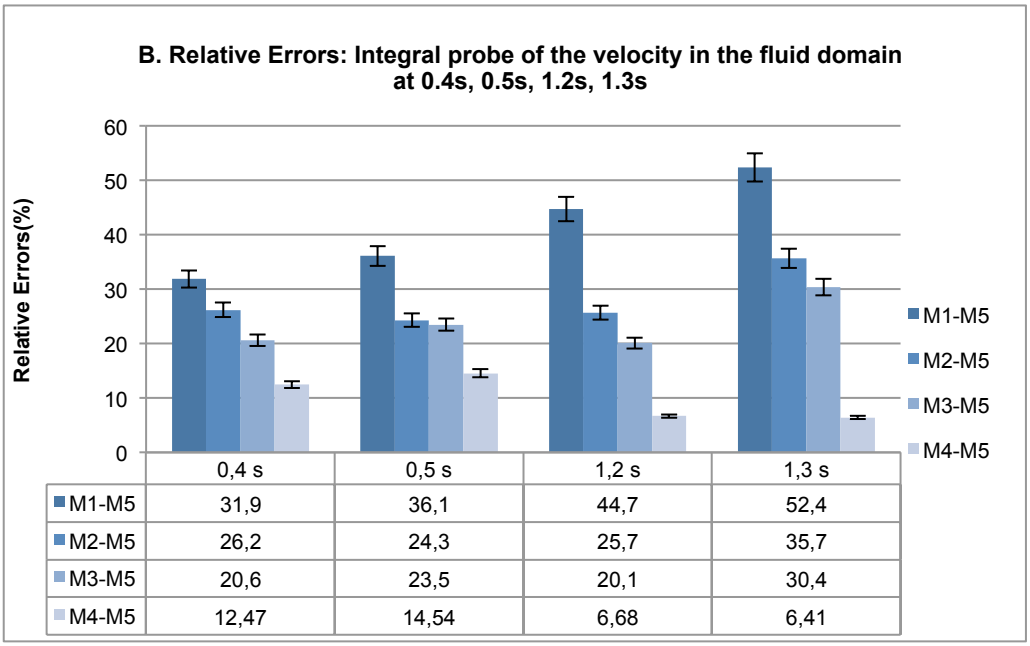

	0,4 s	0,5 s	1,2 s	1,3 s
M1-M5	31,9	36,1	44,7	52,4
M2-M5	26,2	24,3	25,7	35,7
M3-M5	20,6	23,5	20,1	30,4
M4-M5	12,47	14,54	6,68	6,41

Figure 3.12. Convergence study**:** A**.** Integral probe of the velocity in the fluid domain at 0.4s, 0.5s, 1.2s and 1.3s. B. Relative errors evaluation considering the respective results.

3.3. BAV Study and Models Development

3.3.1. Acquisition of aortic root dimensions

Santa Marta Hospital provided data corresponding to six MR exams, from BAV patients (three children and three adults) with different ages. MR exams allow precise measurements. However, patient motion can be challenge, producing non-intuitive artifacts in the transformed images[2].

The acquisition data of aortic dimensions was possible through *The Codonics Clarity Viewer*™. This is an application used for viewing and manipulating digital medical images from different exams sources, such as, CT, MR, for example. *The Condonics* displays patient information, such as patient name, patient ID, birth date and sex, as well as a list of the study folders and patient images. Figure 3.13. shows the different views that were explored on *The Condonics*.

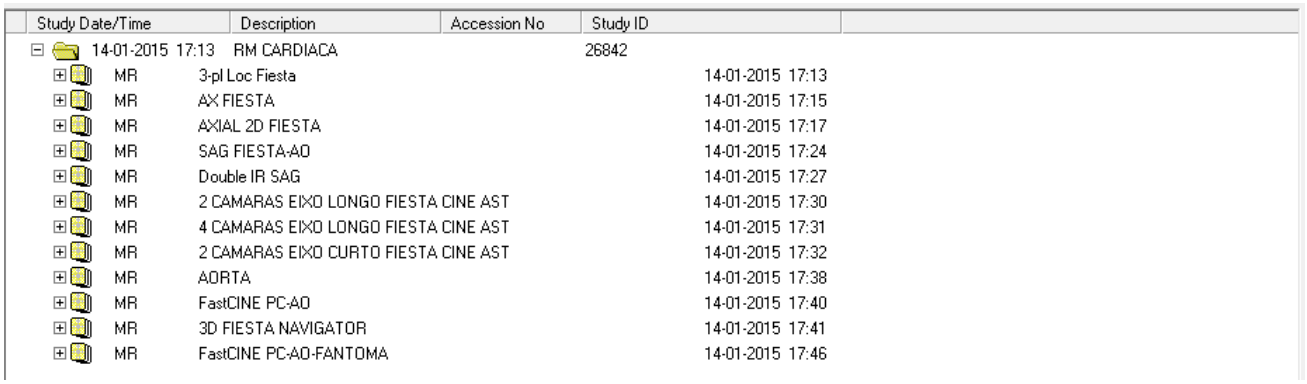

Figure 3.13. MR views available from one specific patient (data provided by Santa Marta Hospital).

To do the measurement process it was necessary to have medical support, because the acquisition data of aortic dimensions is demanding and highly dependent of medical experience. Using the distance measurement tool it was possible to determine the distance between two points in the active images provided, for the different regions of interest. From all available images, two specific MR views were used:

- Aortic valve, which finds the axial slice where the aorta and left ventricle meet, prescribing a plane that passes through both of them. This will result in an oblique coronal scout of the ascending aorta.

- 4 Chambers Long Axis Fiesta, which shows the aortic valve and it is the best for evaluating the septal and lateral walls and apex of the left ventricle, right ventricular free wall, and chamber size.

These images can be observed in Figure 3.14: (i) the image of the aorta allows the observation and an accurately measuring of the aortic annulus (solid blue line), aortic sinuses of Valsalva (solid white line), sinotubular junction (dashed blue line) and mid ascending aorta (dashed white line); (ii) the image of the long axis four chambers (FIESTA Cine) shows the aortic root components and leaflets can be observed (note the highlighted blue region).

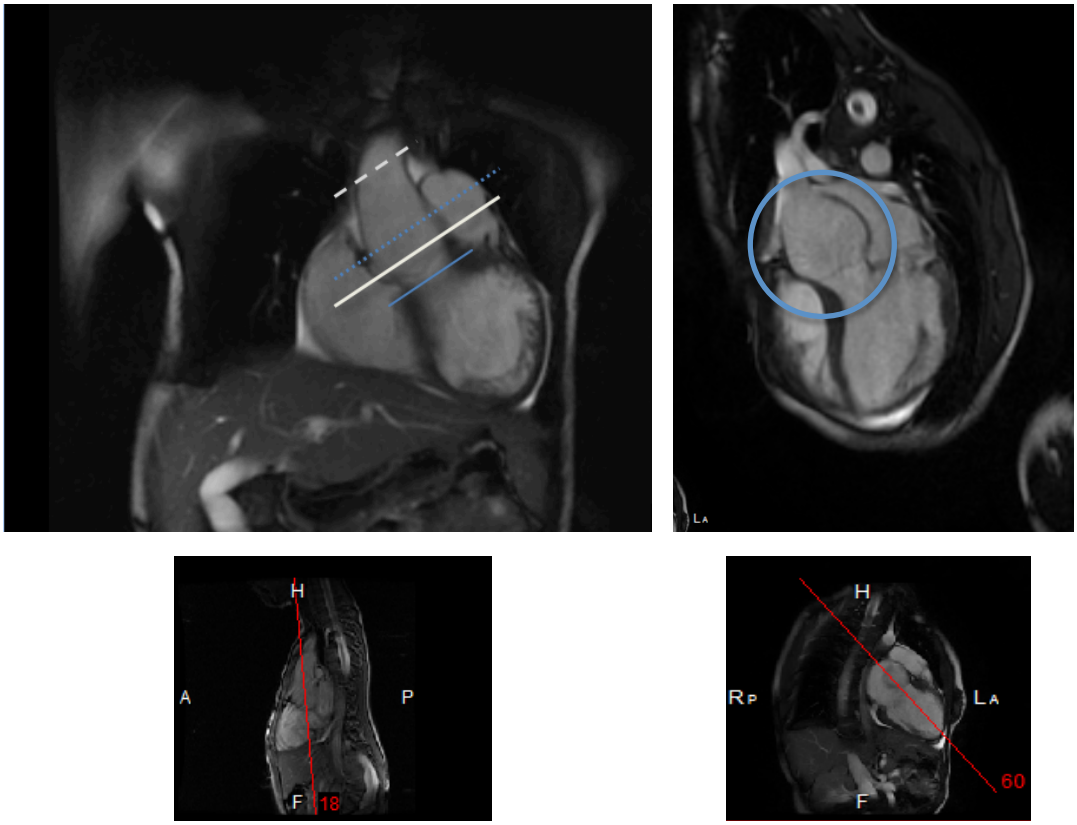

Figure 3.14. Magnetic Resonance exam: procedure performed on a Patient to obtain the aortic dimensions. (a) Aorta image (b) Long axis four chambers image (FIESTA Cine). Images were provided by Santa Marta Hospital.

Figure 3.15. presents the aortic dimensions for 6 patients with BAV. According to the medical doctors some assumptions were made in the measurement process: (1) when the diameter of the sinotubular junction is greater than the annulus diameter then aortic root dilatation (at the sinus of

Valsalva level) is verified; (2) when the diameter of the ascending aorta is greater than the standard value for the patient age, then the dilatation of ascending aorta is verified.

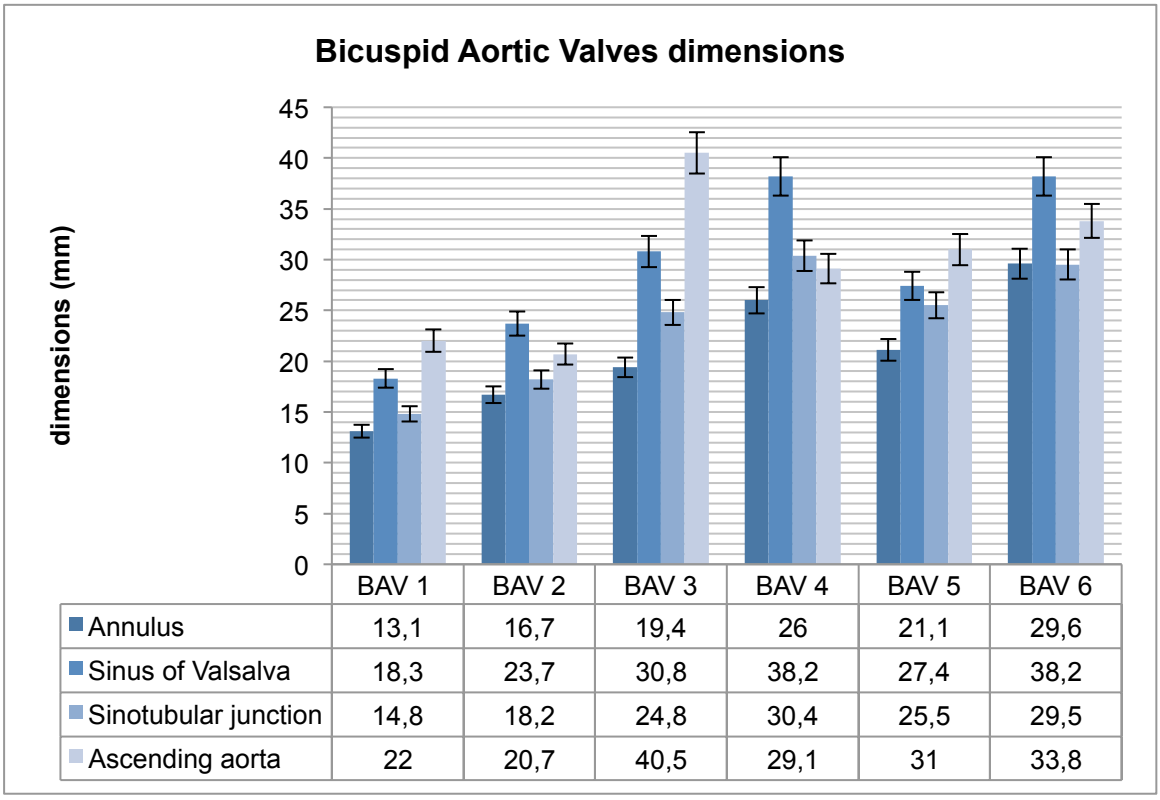

	BAV 1	BAV 2	BAV 3	BAV 4	BAV 5	BAV 6
Annulus	13,1	16,7	19,4	26	21,1	29,6
Sinus of Valsalva	18,3	23,7	30,8	38,2	27,4	38,2
Sinotubular junction	14,8	18,2	24,8	30,4	25,5	29,5
Ascending aorta	22	20,7	40,5	29,1	31	33,8

Figure 3.15. Aortic dimensions for different patients with BAV disease.

As we know each patient presents specific measurements for each aortic root component. However, we decided to observe the aortic dimensions pattern based on literature data[48,77]. For the first four patients, according to the study of the Beroukhim et al. (2006) (Table 3.4), we have: (a) patient 1 (2 years old, male) showed only the diameter of the ascending aorta out of the normal range (0.21 cm above the expressed value); (b) patient 2 (6 years old, female) showed all components in an adequate range; (c) patient 3 (11 years old, female) showed the diameter of the ascending aorta and the sinus of Valsalva are out of range (1.07 cm and 0.15 cm above the expressed value, respectively); and (d) in patient 4 (19 years old, male) the annulus, the sinus of Valsalva and the sinotubular junction are out of range (0.06 cm, 0.56 cm, and 0.24 cm above the expressed value in this study, respectively).

Table 3.4. Aortic dimensions according with age: 0-19 years old[77].

Age Group (years)	Component	Patients with BAV	Controls	P Value
0-4.9		n=25	n=34	
	Annulus (cm)	1.29 ± 0.24	1.08 ± 0.19	0.0002
	Sinus of Valsalva (cm)	1.70 ± 0.31	1.46 ± 0.27	0.0007
	Sinotubular junction (cm)	1.40 ± 0.30	1.16 ± 0.22	0.0005
	Ascending aorta (cm)	1.64 ±0.35	1.30 ± 0.24	<0.0001
5-9.9		n=28	n=20	
	Annulus [cm]	1.72 ± 0.28	1.52 ± 0.14	0.0008
	Sinus of Valsalva (cm)	2.27 ± 0.37	2.04 ±0.25	0.003
	Sinotubular junction (cm)	1.89 ± 0.33	1.68 ± 0.21	0.003
	Ascending aorta (cm)	2.18 ±0.34	1.81 ± 0.23	<0.0001
10-14.9		n=33	n=22	
	Annulus (cm)	2.00 ±0.25	1.78 ± 0.21	<0.0001
	Sinus of Valsalva (cm)	2.62 ± 0.31	2.43 ± 0.20	<0.0001
	Sinotubular junction (cm)	2.14 ± 0.34	2.01 ± 0.22	0.03
	Ascending aorta (cm)	2.55 ± 0.43	2.16 ± 0.21	<0.0001
15-19		n=15	n=27	
	Annulus (cm)	2.27 ± 0.27	2.01 ± 0.27	0.002
	Sinus of Valsalva (cm)	2.93 ± 0.33	2.68 ± 0.33	0.01
	Sinotubular junction (cm)	2.47 ± 0.33	2.23 ± 0.25	0.02
	Ascending aorta (cm)	2.91 ± 0.47	2.41 ± 0.26	<0.0001

Note that the p-value is used in the context of null hypothesis testing in order to quantify the idea of statistical significance of evidence, therefore, the lower is the p-value, the more evidence we have.

According to Jackson et al. (2013)[48], patients 5 (22 years old, female) and 6 (27 years old, male), the aortic dimensions for BAV are in the range of values of Table 3.5.

Table 3.5. General ages: Aortic Dimensions in Patients with BAVs[48].

Component	Patients with BAV	P value
	n=62	
Annulus (cm)	2.50 ± 0.40	>0.2
Sinus of Valsalva (cm)	4.10 ± 0.80	>0.2
Sinotubular junction (cm)	3.85 ±0.90	>0.057
Ascending aorta (cm)	5.20 ± 0.40	>0.108

3.3.2. Construction of six patient-specific geometries

After data acquisition and measures validation from comparison with literature, we constructed six geometries on COMSOL. The same tools described in Section 3.2.1 were used to construct the TAV model. Table 3.6 presents the dimensions considered to construct each one of them and Figure 3.16 shows the respective geometries.

Table 3.6. Dimensions used to construct the idealized geometries of patients with BAV.

Dimensions	BAV 1	BAV 2	BAV 3	BAV 4	BAV 5	BAV 6
Computational domain length (mm)	36	46	48	65	55	67.5
Entry length [mm]	10-20 (Adapted according with Reynolds number)					
Exit length [mm]*	11	15	17.5	23	22	19
Thickness [mm]						
(a) N.C. cusp	0.2-0.8					
(b) Fused cusp	0.4-1.1					
(c) Aortic wall	<1					
Leaflets length [mm]						
(a) N.C. cusp	≈4	≈5	≈7	≈8	≈5	≈12
(b) Fused cusp	≈7	≈9	≈12	≈17	≈13	≈18

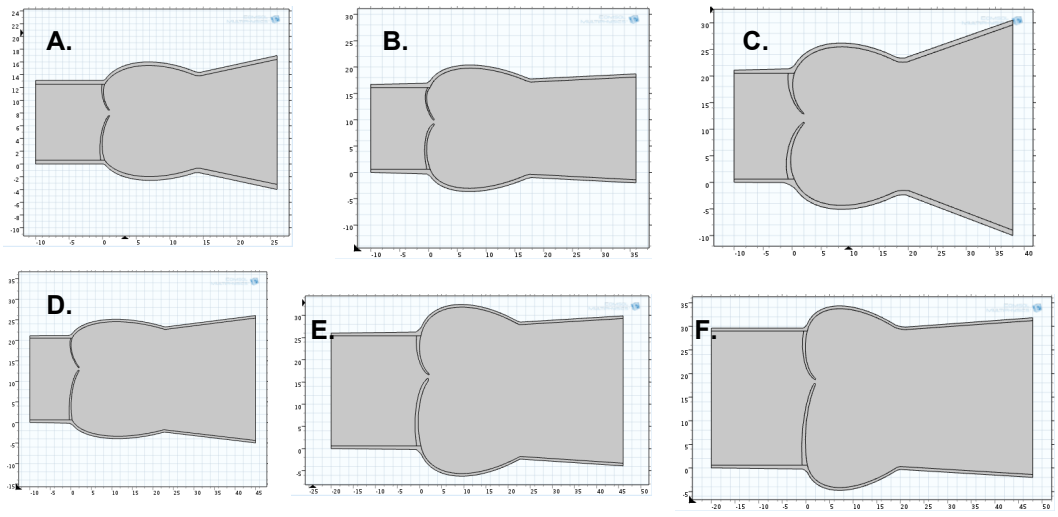

Figure 3.16. Patients: A. Patient 1 (male, 2 years old). B. Patient 2 (female, 6 years old). C. Patient 3 (female, 11 years old). D. Patient 4 (male, 19 years old). E. Patient 5 (female, 22 years old). F. Patient 6 (male, 27 years old).

3.3.3. Materials and boundary conditions

Regarding the materials applied to BAV models, the non-coronary cusp of each model was considered with less stiffness (Young modulus of 0.37 MPa) in relation to the other fused cusps. (Young modulus was increased to 0.74 MPa) (Table 3.7).

Table 3.7. Material properties for different models of patients with BAV[17].

Model name	Cusp symmetry	Cusp	Young modulus (MPa)	Poisson ratio
BAV models	No	Non-coronary cusp	0.37	0.49
		Fused cusp	0.74	

Note that boundary conditions used in BAV models are explained in section 3.2.3.

3.3.4. BAV models: mesh generation

The procedure used for mesh generation was the same and adapted to each created BAV model. The number of degrees of freedom was selected taking into account the convergence study made for TAV. The respective results can be observed in Table 3.8.

Table 3.8. Mesh generation for six valve patients with BAV disease.

Patients	Total degrees of freedom solved	Number of mesh elements	Average element quality
BAV 1	50933	17444	0.9647
BAV 2	59506	20105	0.9651
BAV 3	98404	34725	0.9715
BAV 4	93516	31928	0.9673
BAV 5	81106	28056	0.9682
BAV 6	83037	30192	0.9705

3.4. Solver parameters used in the simulations

As already mentioned COMSOL Multiphysics[18] was used to solve all the different models (TAV model and BAV models) previously created. Regarding the solver configurations, it was chosen the *MUMPS* (multifrontal massively parallel sparse direct solver). It estimates how much memory the system requires (the default is 1.2). The *Preordering algorithm* was *Automatic* (the default automatically selected by the MUMPS solver). *Row preordering* was used to control the maximum weight matching strategy. *Use pivoting* was applied to controls whether pivoting should be used). The default was kept (*On*), being the Pivot threshold number the default (0.1). It means that "in any given column the algorithm accepts an entry as a pivot element if its absolute value is greater than or equal to the specified pivot threshold times the largest absolute value in the column"[18].

The *Fully Coupled* attribute was used with the *Time-Dependent Solver*. It uses a damped version of Newton's method. Constant (Newton) was chosen, being necessary some specifications: the *Damping factor*, the *Limit on nonlinear convergence rate*, the *Jacobian update* and the *Termination technique*. The *Damping factor* is applied to specify a constant damping factor for the Newton's method (the default 1 was used). The *Limit on nonlinear convergence* rate was implemented to force the nonlinear solver to terminate as soon as the convergence is estimated to be too slow (the default was implemented, 0.9). To limit the convergence rate we selected the option once per time step. With respect to the *Termination Technique*, it is useful to control how the Newton iterations are terminated (with the *Tolerance* and with the *Maximum number of iterations*). *Tolerance* is useful when the estimated relative error is smaller than a specified tolerance. When the maximum number of iterations has been performed Newton's method is terminated even if the tolerance is not fulfilled.

Table 3.9. clarifies some solver specifications used in COMSOL[18]:

Table 3.9. Solver Specifications.

Solver specifications	Time dependent solver
Null-space function	Automatic
Default assembly block size	Checked (1000)
Stop if error due to undefined operation	Selected
Solution form	Automatic
Scaling variables	Automatic
Row equilibration	Checked
Matrices reassembly	Automatic
Time steps	Free or Strict
Initial time step	1e-3 s
Maximum time step	1e-4 s
Backward differentiation formula	2

Table 3.9. refers to the use of the backward differentiation formula (BDF), which is a family of implicit multisteps for the numerical integration of ordinary differential equations.

3.5. Development of a 3D TAV model

After the construction of the 2D models on COMSOL, we decided to develop a 3D prototype of a TAV considering the sinuses and the leaflets. In order to do that we studied the available bibliography. For example: (i) Thubrikar et al. (1990) introduced a 3D geometry description of the aortic valve using the intersection of a cone with inclined planes as the geometric model with the purpose of investigating the optimal dimensions with appropriate coaptation, with a minimal volume and an efficient use of energy[15]. (ii) Rankin (2008) evaluated the three dimensional anatomy of the sinuses of Valsalva, describing them as three identical hemispheres intersecting a cylinder with equivalent radius, in normal human hearts (of eight human cadaver hearts)[78].

To construct our 3D idealized geometry (Figure 3.17) we used the dimensions obtained in the literature (Chandra et al. (2012) and Marom et al. (2012))[15,17]. This construction was challenging. Figure 3.14. shows the prototype designed on Solidworks 2014. Different tools were used, namely, *Surface-Loft* (to develop the sinuses surface, as well the leaflets), *Surface Extrude* (to develop the structure), *Split Line* (to construct the sinuses of Valsalva from an initial cylinder), *DeleteFace*, *Body-Delete*, *SurfaceKnit*, *Surface-Fill*, *CircularPattern*, *Thicken*.

The 3D geometry constructed was imported to Comsol as an IGS model (a 3D CAD file). Then, we needed some adjustments to apply the FSI methodology to our geometry, such as in particular, its subdivision into different subdomains.

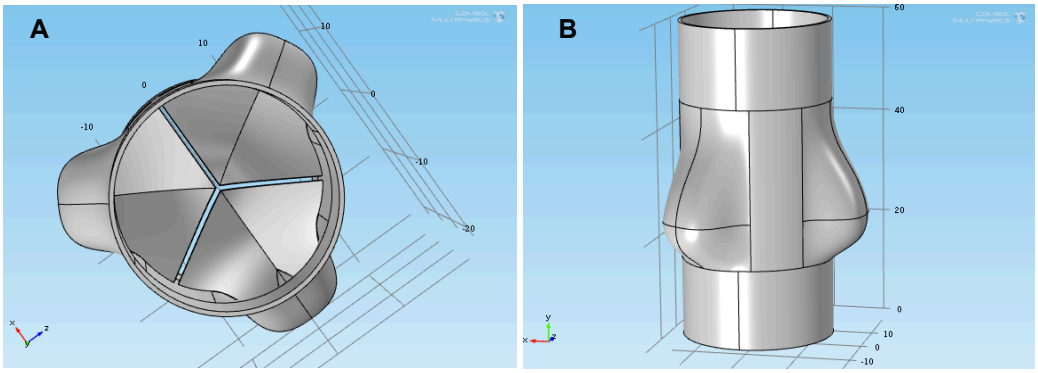

Figure 3.17. Prototype of a TAV geometry constructed in SolidWorks and imported to COMSOL[18].

Regarding the materials properties, blood and structure were defined on the 2D TAV model. However, with respect to boundary conditions, we decided to simplify (Figure 3.18) since the implementation of a cardiac cycle or of two cardiac cycles (as in the previous 2D models) is challenging and involves limitations that will be explored in the next Chapter.

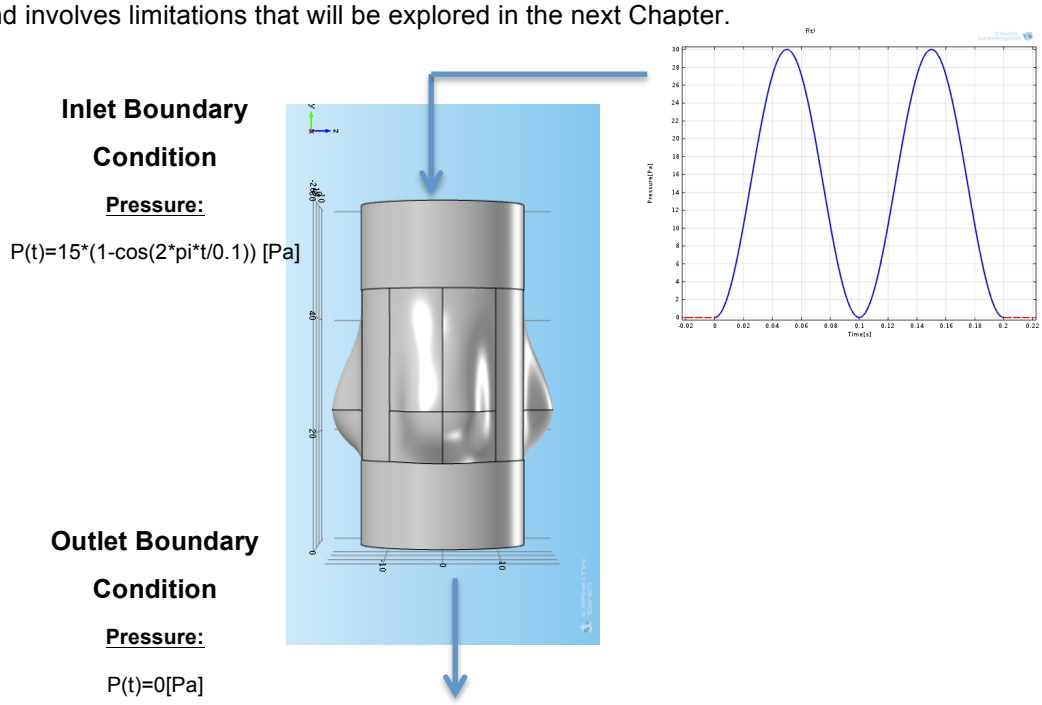

Figure 3.18. Boundary conditions applied to the 3D TAV model.

Figure 3.19. A. shows the interior (fluid domain) and the exterior domain (structure) of the geometry and Figure 3.19.B. shows the mesh generated (541 139 degrees of freedom).

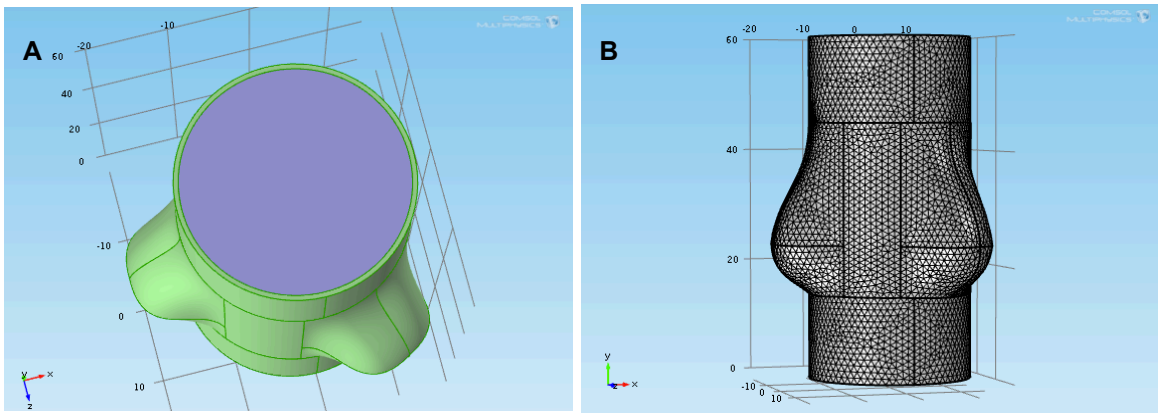

Figure 3.19. 3D TAV model: A. Domains created to apply the FSI method. B. Mesh created.

After these steps we adjusted the solver parameters (explained in section 3.4 of this Chapter) and the simulation was initiated.

CHAPTER 4

Results and Discussion

Chapter 4 is dedicated to the numerical results performed in 2D idealized geometries. Simulations were carried out considering blood (as an unsteady Newtonian fluid) and the structure as a linear elastic isotropic material. Systematic quantitative and qualitative comparisons were executed. From the anatomical point of view, differences between a TAV model (completely idealized geometry) and six BAV models (idealized geometries constructed from realistic provided data) were tested. Tests and analysis were done using the FSI based on an ALE formulation. The boundary conditions at the upstream (left ventricle) and downstream (aorta) were considered to evaluate 2 cardiac cycles. Comparisons related with the aortic root model flow patterns, flow velocity and respective streamline fields, leaflet deformations, WSS and OSI were made, and the respective results will be presented and discussed. To finalize this Chapter a 3D TAV model imported and implemented on COMSOL is briefly explained.

4.1. 2D TAV Model

Considering the constructed TAV model, two studies were made: (i) TAV model 1, with boundary conditions where the blood flows through the aortic valve with a peak velocity of 1.35 m/s[54](normal physiological condition); (ii) TAV model 2, with boundary conditions where velocities approximately 23,8% above of the peak velocity. Figure 4.1 (the aortic root model of TAV 1) and Figure 4.2 (aortic root model of TAV 2) describes the respective aortic valve behavior. At t=0 s both TAV models are completely close. From this moment (t=0s) the acceleration phase is verified, the leaflets open, starting the ventricular systole (t=0.024s, the maximum velocity magnitude verified is 0.47 m/s for TAV 1, and an increase of 27.7%, 0.65 m/s, was observed for TAV 2). The valve opens due to the gradient of pressure imposed across the valve that contributes to increase the flow. At t=0.076s a blood jet is formed from the valvular orifice. This jet remains in the aortic valve from t=0.076s (with the maximum

velocity magnitude of 1.2 m/s for TAV 1, and with an increase of 22,6%, 1,55 m/s, for TAV 2) until 0.26s for TAV 1 (with a maximum velocity magnitude of 1.18 m/s in TAV 1) and until 0.28 s in TAV 2 (with an increase of 20.8%, 1.49 m/s, in TAV 2). Leaflets are completely opened at t=0.116s (the maximum velocity magnitude is 1.25 m/s in TAV 1, with an increase of 26.4%, 1.7 m/s in TAV 2). At the peak of systole, from t=0.168s until 0.180s, the jet has as maximum velocity magnitude of 1.30 m/s in TAV 1 and with an increase of 23,5%, 1.7 m/s, in TAV 2. There is a decreasing of the velocity magnitude until the coaptation moment (t=0.469 s). The aortic valve starts to close from t=0.469s (maximum velocity magnitude 0.45 m/s in TAV 1, with an increase of 22.4%, and 0.58 m/s for TAV 2) until t=0.557s (maximum velocity magnitude 0.36 m/s for TAV 1, with an increase of 25% and 0.48 m/s for TAV2), simulating the ventricular filling due to the inversion of the pressure gradient. From t=0.561s until t=0.80s the valve opens (with maximum velocity magnitudes for both valves), originating the blood flow jet from the valvular orifice.

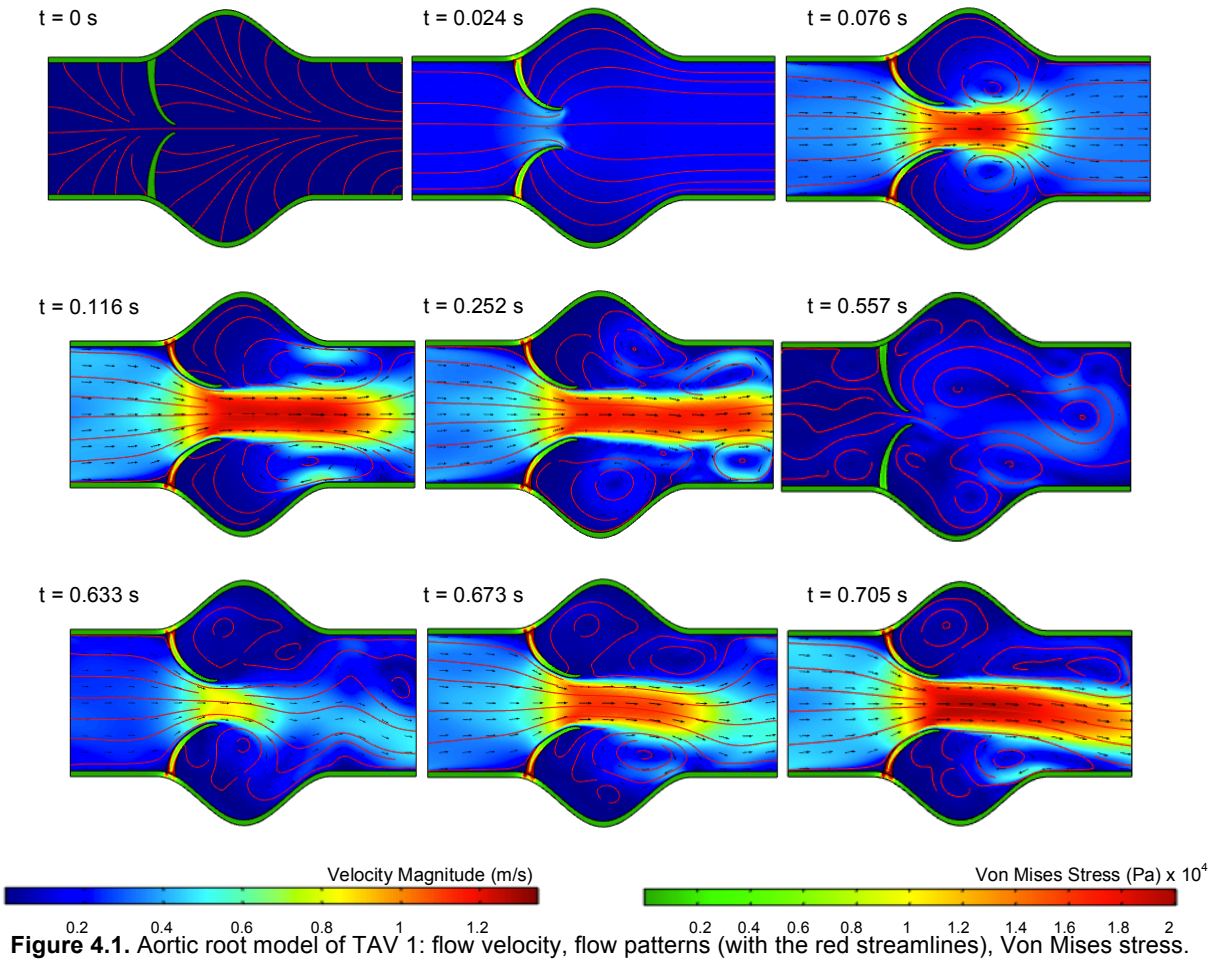

Figure 4.1. Aortic root model of TAV 1: flow velocity, flow patterns (with the red streamlines), Von Mises stress.

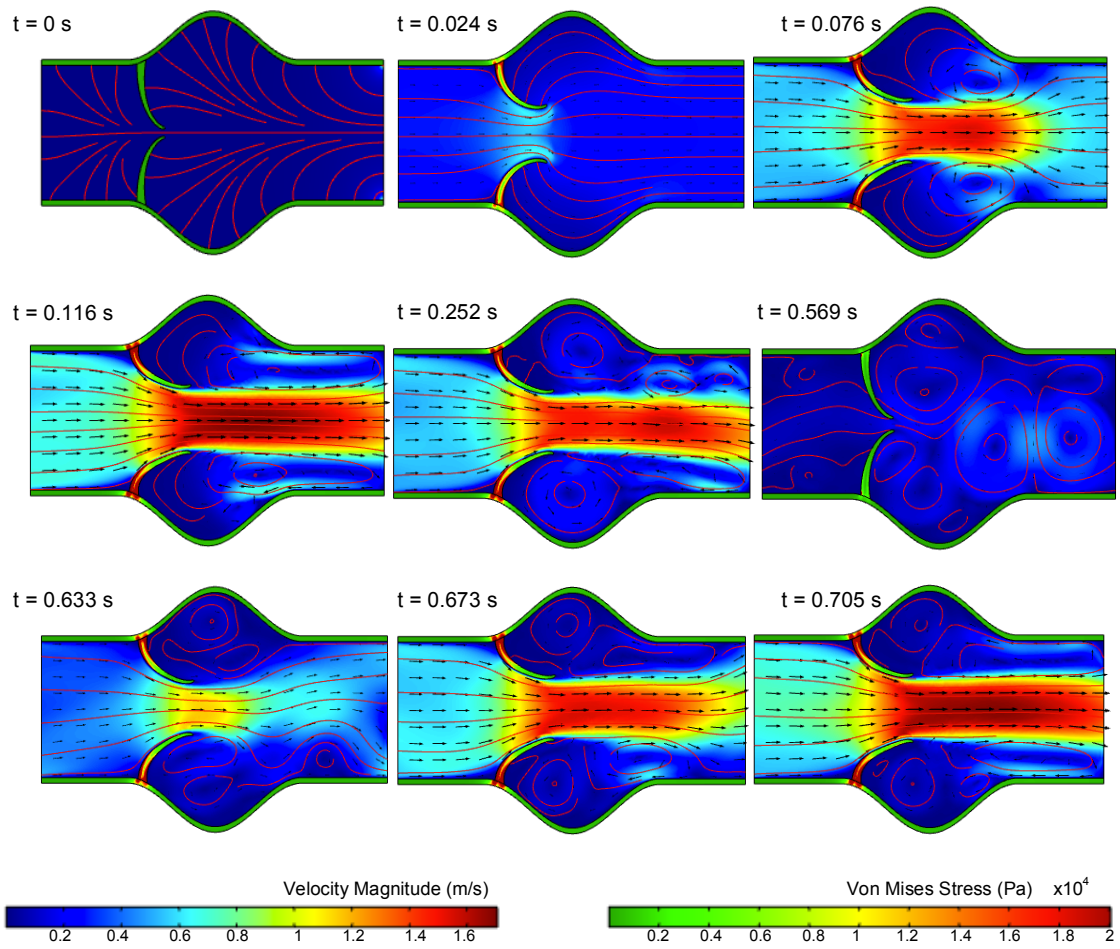

Figure 4.2. Aortic root model of TAV 2: flow velocity, flow patterns (with the red streamlines), Von Mises stress.

During the cardiac cycle it was observed: (i) a recirculation area in the sinuses with the presence of vortices (Figures 4.1 and 4.2, t=0.076 s, t=0.116 s) and (ii) high velocities are needed to align the jet formed along the center of the aorta.

Regarding the Von Mises stress, the highest values are on the base of the cusps (Figure 4.1 and 4.2, red regions) and the lowest stresses towards their respective free edges (Figure 4.1 and 4.2, green regions). At the peak velocity, the highest Von Mises stress corresponds to 275 KPa (base of cusps is the critical region). Similar values, between 243 KPa and 277 KPa, were observed in Espino et al. (2015) study[73]. As it can be verified in the snapshots sequence (Figure 4.1 and Figure 4.2): (i) the two leaflets deformed in a symmetric way in the aortic root model; (ii) the greatest cusp deflection occurred at cusp-free edges.

Regarding the WSS effects, they were verified at the boundaries (leaflets and wall), but they were verified more pronounced on the leaflets in both TAV models (Figure 4.3). The increase of velocity contributes to evident effects in the WSS on the leaflets (Figure 4.3). For example, at 0,116 s, values of velocity magnitude are close to 1.25 m/s, the WSS is around 7.13 N/m^2 (TAV 1); consequently, for velocities around 1.7 m/s in TAV 2, the WSS is 10.4 N/m^2, having an increase of 31.42% in the WSS. Observing Figure 4.3. the maximum values of the WSS are verified on the belly and on the tip of leaflets. Thus, high WSS in these regions can accelerate the calcification.

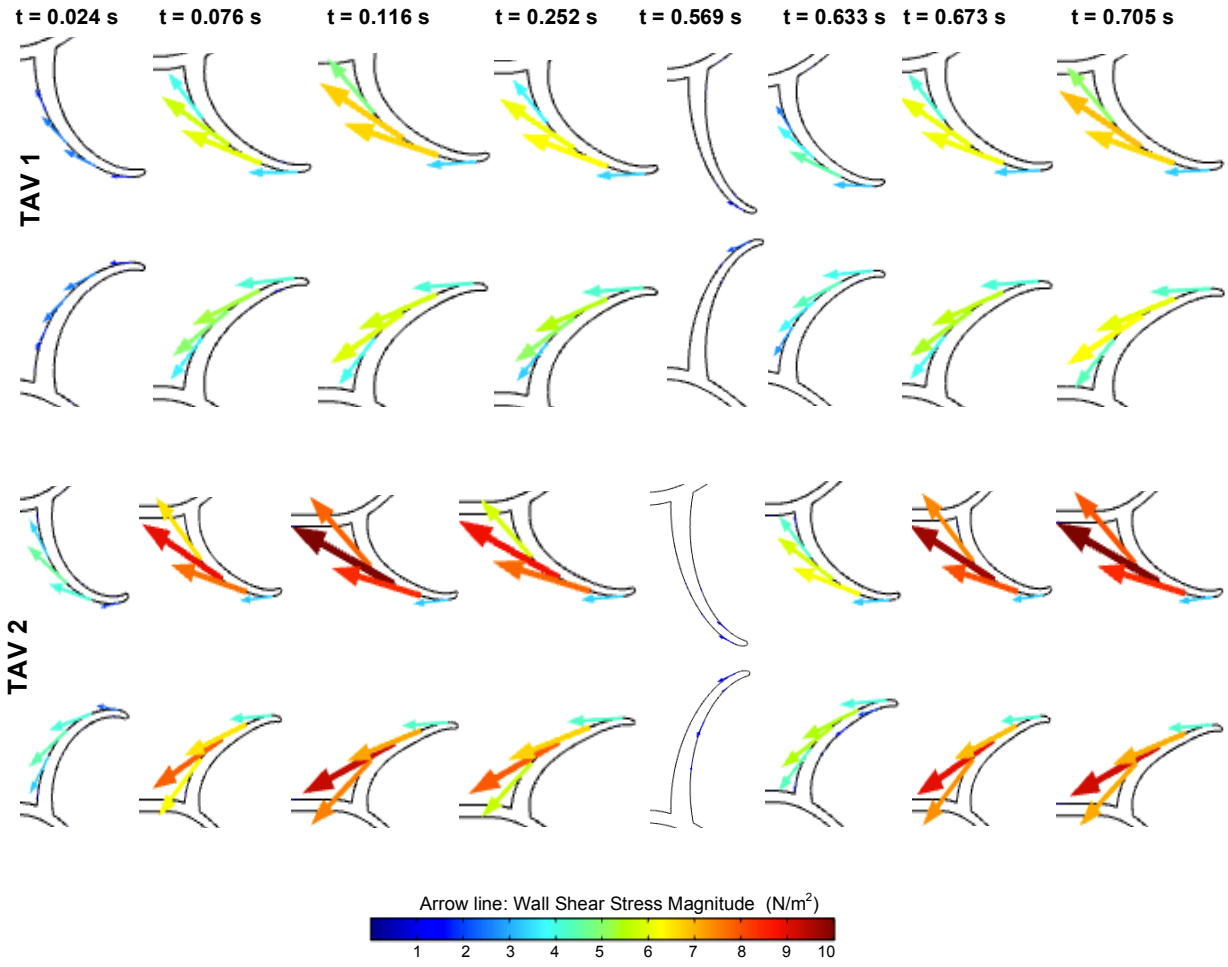

Figure 4.3. TAV 1 and TAV 2: A. wall shear stress (N/m^2) on the leaflets.

Until now, we observed the results for one cardiac cycle. Figures 4.4. – 4.7. describe results for two cardiac cycles in TAV 1 and TAV 2. Figure 4.4. shows that: (i) the behavior of the valves (they start closed, then open, and this proceeds alternately); (i) the maximum velocity flow values (magnitude),

are 1.3 m/s in the TAV 1 and 1.7 m/s in the TAV 2, for both cardiac cycles; (i) the minimum velocity flow values (magnitude) below 0.5 m/s in TAV 1 and above 0.5 m/s in TAV 2 for the first cardiac cycle and in the second cardiac cycle 0.34 m/s in both TAVs.

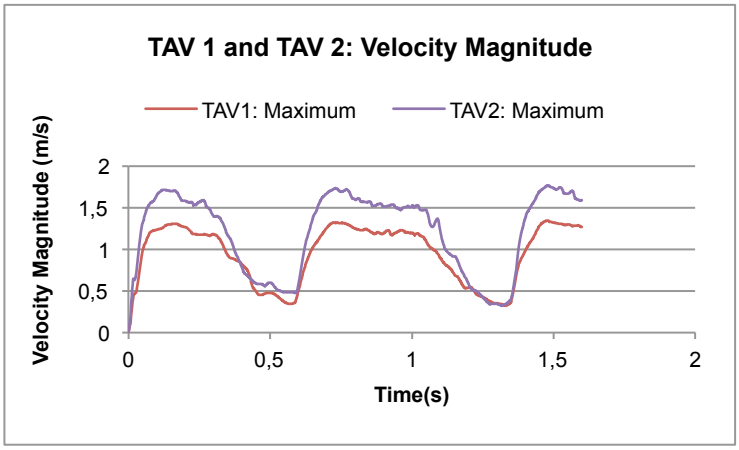

Figure 4.4. TAV 1 and TAV 2: velocity magnitude (m/s) during two cardiac cycles.

Regarding the Von Mises stress, high values are verified with maximum velocities, that are observed when leaflets are completely open (Figure 4.5, between t=0 s – 0.4 s, t = 0.6 s – 1.2 s, t = 1.4 s – 1.6 s). Consequently, when the leaflets are closed the velocities are lower and the Von Mises stress values decrease (Figure 4.5, between t= 0.4 s-0.6 s, and, t =1.2 s-1.4 s). Von Mises stresses on the leaflets are 80% greater in comparison with the values on the aortic wall. According to our results, inferior leaflets of TAVs are more susceptible to higher Von Mises stress (Figure 4.5, green and violet lines). With respect to the wall, TAVs Von Mises stress values are below 1,0x10^5 Pa.

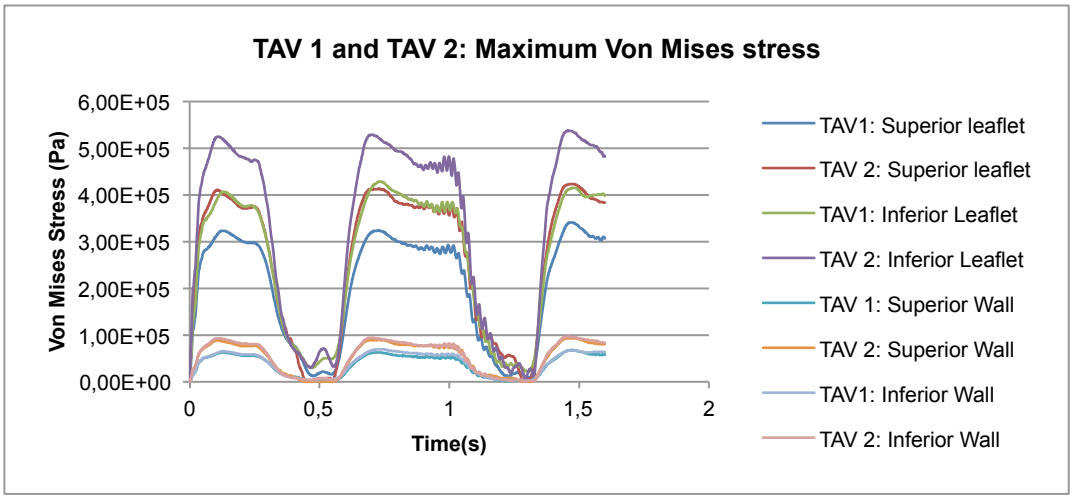

Figure 4.5. TAV 1 and TAV 2: maximum Von Mises stress (Pa) during two cardiac cycles.

WSS was tested due to the interaction between the wall and blood flow in the lumen and also between the leaflets and the blood flow. High velocities imply high WSS. For TAV 1 and TAV 2 (Figure 4.6, A and B, show red line and blue lines for leaflets), we observe a maximum WSS average of 2.5 N/m^2 in TAV 1[79] and a maximum WSS average of 3.5 N/cm^2 in TAV 2. This WSS is related to the leaflets (belly and tip region, Figure 4.3). Inferior aortic wall is more affected to high velocities, in comparison with superior wall in the TAV 1 (Figure 4.6, A). Regarding the TAV 2, WSS for superior and inferior aortic wall is similar (observe the green and violet lines of Figure 4.6, B).

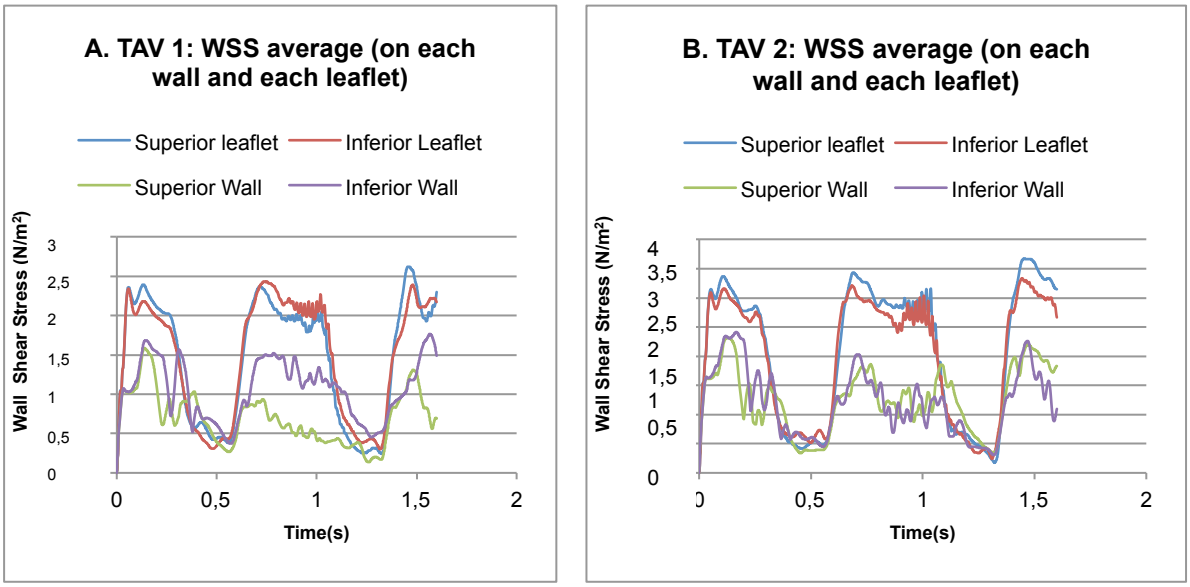

Figure 4.6. WSS average (superior and inferior leaflets, superior and inferior wall), in TAV 1 (A) and TAV 2 (B) during two cardiac cycles.

With respect to the WSS before the leaflets and after the leaflets (Figure 4.7): (i) before the leaflets WSS average values are close in each TAV, with a maximum WSS average around 2.5 N/m^2 in TAV 1 (blue line and red line) and around 1.7 N/m^2 in TAV 2 (green and violet lines); (ii) after the leaflets there is an obvious dispersion of WSS values during the cardiac cycles in both TAVs - the maximum values decrease, the minimum values increase throughout the cardiac cycle.

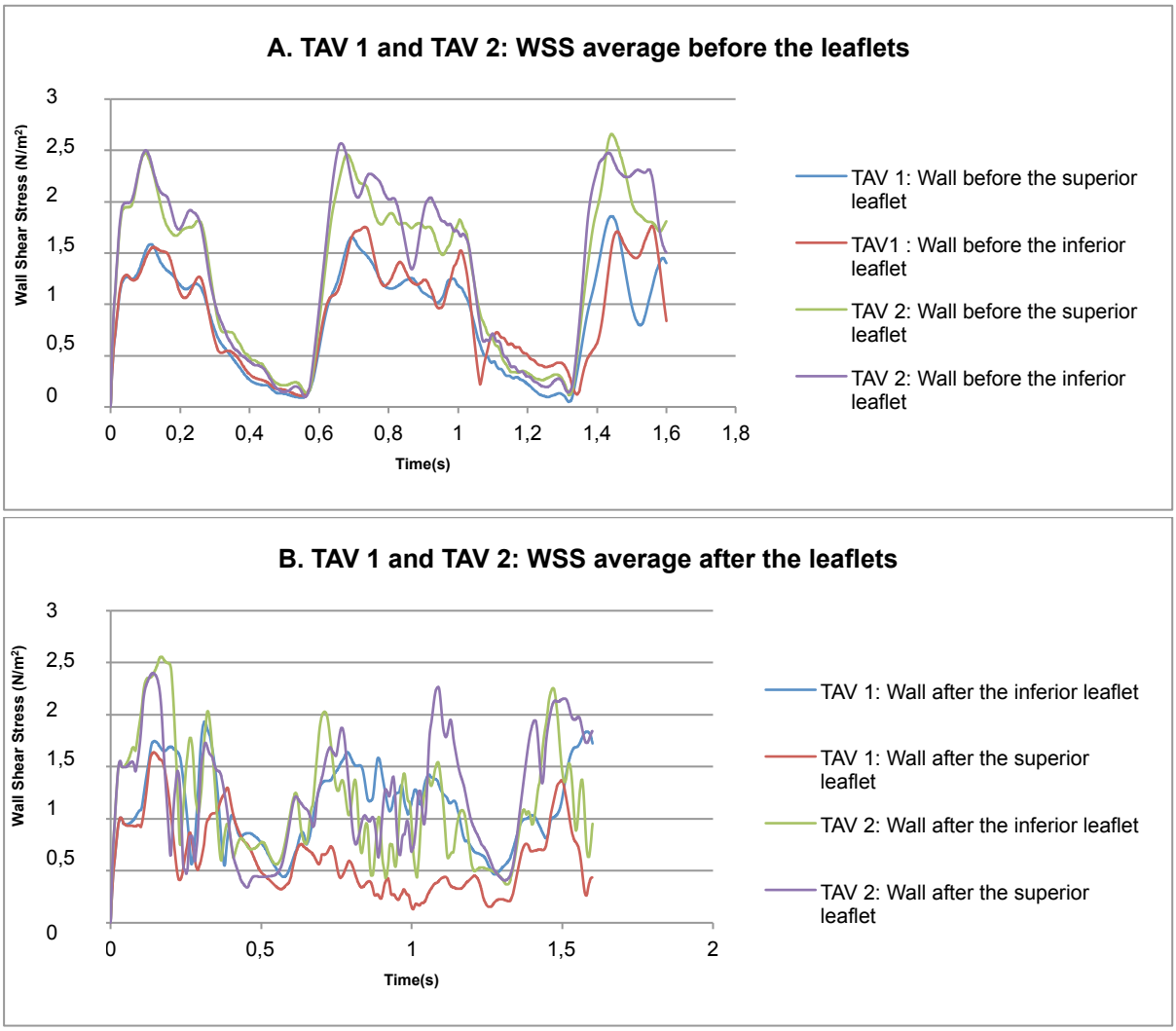

Figure 4.7. WSS average analysis along the aortic wall, before and after the leaflets, in TAV 1 (A) and TAV 2 (B) during two cardiac cycles.

A topic of discussion reported by Espino et al. (2015)[73] was the inclusion of the aortic arch in our model, because it becomes possible the prediction of the recirculation in the ascending thoracic aorta, away from the aortic root. With the aortic root model, this prediction can be difficult, however, in the following BAV analysis we decide to include the ascending thoracic aorta to observe the results.

4.2. Patients with Bicuspid Aortic Disease (2D models)

After the analysis on the TAV1 and TAV2 models, this section describes a comparison between the velocities obtained for each patient with BAV disease and those obtained for the TAV 2 model. Figure

4.8. shows the velocity magnitude variation between BAV patients and TAV 2, where the main differences are verified when leaflets are opening and closing (Figure 4.8, orange highlighted), the velocities in both cases being higher (when compared with TAV 2). The velocity analysis was the base to focus on Von Mises stress, WSS and OSI.

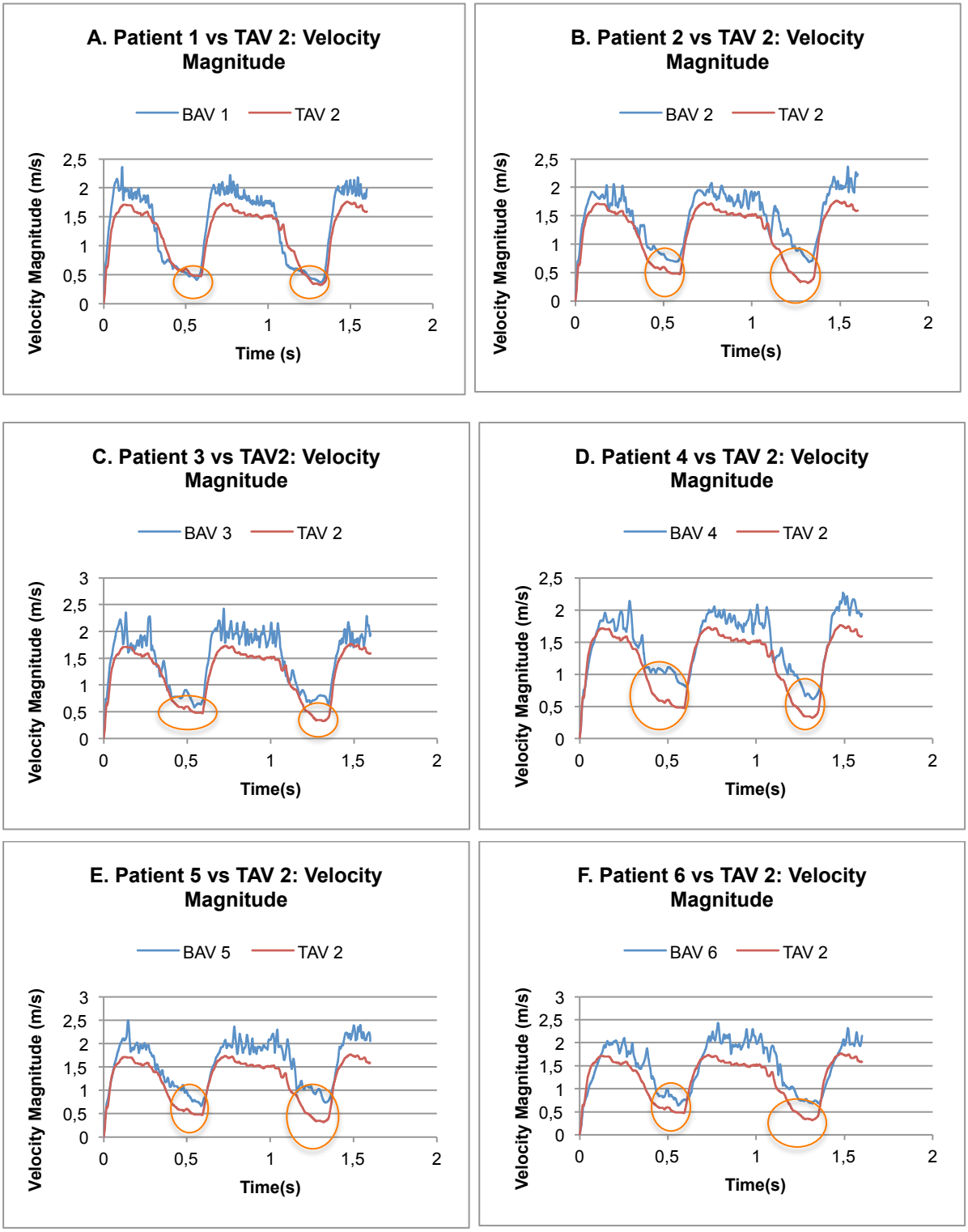

Figure 4.8. Velocity Magnitude (m/s) comparison results for TAV 2 and with BAV disease each patient.

4.2.1. Patient 1 (2 years old, male)

Figure 4.9. (BAV 1, aortic root model of patient 1) describes the respective valve behavior during one cardiac cycle. As in the previous description, at t=0 s BAV 1 is closed (as in the next five BAVs to be described). From this moment (t=0s), due to the traction condition on the outlet, the acceleration phase starts. At t=0.024s (Figure 4.9), the maximum velocity magnitude verified is 1.07 m/s in BAV 1, an increases of 39.25% in comparison with the maximum velocity magnitude flow verified in TAV 2 (0.65 m/s). Note the formation of a blood recirculation area in each sinus (Figure 4.9, t=0.024s) to promote the blood jet genesis. At t=0.076s (Figure 4.9) the blood jet is completely formed, with the leaflets completely open, leading to a maximum velocity flow of 2.12 m/s (corresponding to an increase of 26.88% in comparison with TAV 2). At t =0.076s, there are vortices in the region of the ascending thoracic aorta that cause instabilities in the blood flow. This jet remains with maximum velocity magnitudes (between 1.98 and 2m/s) until approximately t=0.22s. At t=0.112s it is reached the maximum velocity magnitude 2,36 m/s (an increase of 44.91% in comparison with the maximum velocity verified in TAV 2, 1.30 m/s). With the decrease in the velocity there is an evident blood flow asymmetry (Figure 4.9, at t=0.116s the maximum velocity magnitude is 2.06 m/s; at t=0.276s it is 1.69 m/s; and at t=0.336s, it is 0.91 m/s) to the superior ascending thoracic region. These results may be related with the asymmetry imposed between the non-coronary and the fused leaflets, and with the increased stiffness of the fused leaflet (from the 0.37 MPa to 0.74 MPa). Vortices are created since t=0.076s (acceleration phase) and remains in the valve until the coaptation moment (Figure 4.8, t=0.453s – 0.469s, where the maximum velocity magnitudes are close to 0.56 m/s, with only an increase of 14.28% in comparison with TAV 2, 0. 48 m/s). At t=0.276s small vortices (previously created) that appear close to the tip of the leaflets can be observed, but also the genesis of a bigger vortex close to the ascending thoracic aorta. Thus, coaptation is perturbed by recirculation (the bigger vortex appears at the ascending thoracic aorta) (Figure 4.8, t=0.336s, t=0.469s). The recirculation (and the respective rolling of the streamlines around the vortex) can have consequences in the aortic

wall because the flow doesn't have a normal behavior through the aorta[73] and also leads to prevent the effective coaptation of the leaflets[17]. From t=0.573 s until t=0.80 s the valve opens, and the blood flows through the valvular orifice, as can be observed in Figure 4.8, at t=0.633 s (maximum velocity magnitude of 1.51 m/s), t=0.673s (maximum velocity magnitude of 2.02 m/s), t=0.745s (maximum velocity magnitude of 1.93 m/s). Regarding the Von Mises stress, as it was observed in TAVs, the highest values are on the base of cusps and the lowest stresses are located near their respective free edges. At the peak velocity, the highest Von Mises stress values represent an increase of 37.5%, 440KPa (Figure 4.8, t=0.076s), in comparison with the 275 KPa verified for TAV 2.

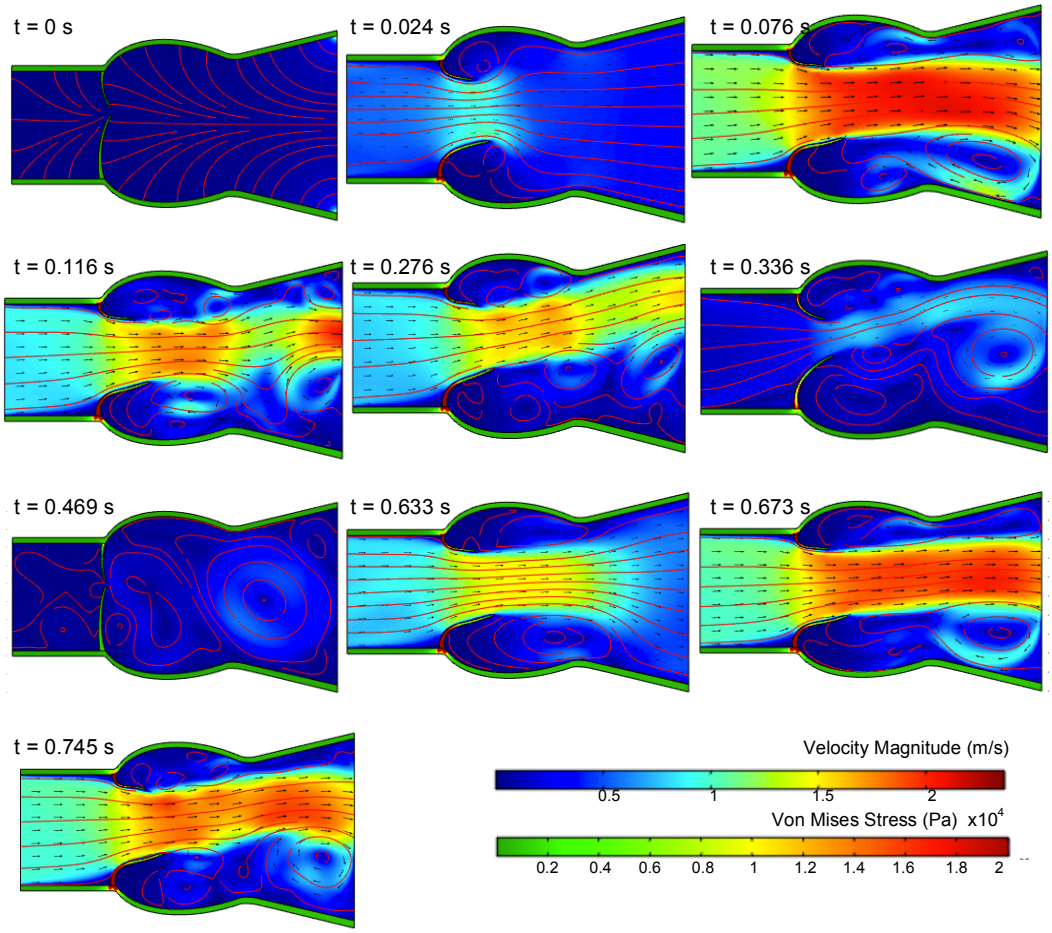

Figure 4.9. Aortic root model of BAV1: flow velocity, flow patterns (with the red streamlines) and Von Mises stress.

The WSS was analyzed on the boundaries (leaflets and wall), with effects on the leaflets and on the ascending thoracic region (Figure 4.10). As it was previously explained, velocity increases, promotes effects on the WSS results, but also on the recirculation areas verified during the cardiac cycle (Figure

4.9, highlighted regions: sinuses end and ascending thoracic region). As on the TAV models, WSS effects on leaflets are verified at the belly and the tip (figure 4.10). For example, at 0.076 s, the maximum velocity magnitude is 2.12 m/s, the WSS is 40 N/m^2 representing an increase of 77.68%; and, at 0.116s, values of the velocity magnitude are close to 2,06 m/s, the WSS is around 26.8 N/m^2, representing an increase of 61,19% comparing with TAV 2.

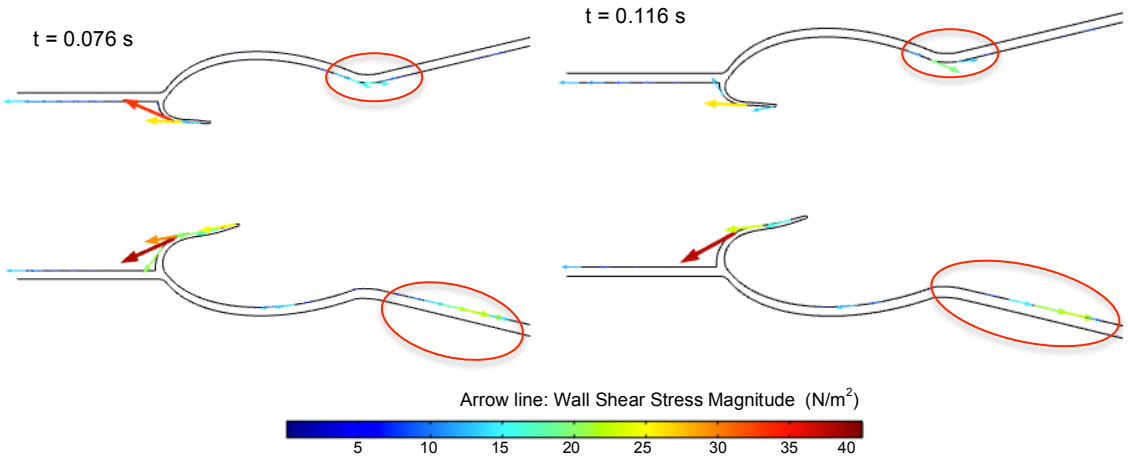

Figure 4.10. BAV 1: Wall Shear Stress (N/m^2) for the valve.

Higher Von Mises stress values are verified for maximum velocities when leaflets are open (Figure 4.11) and lower Von Mises stress when leaflets are closed. Von Mises stresses are higher on fused leaflet (the maximum Von Mises stress value is approximately 8.0x10^5 Pa), than on the non-coronary leaflet (where the maximum Von Mises stress value is approximately 6.0x10^5 Pa). This result shows that a calcified leaflet is subject to more stresses (Figure 4.11, red line). Von Mises stresses on the leaflets are 87.5% higher in comparison with the aortic wall (more 7.5% in relation to TAV 2). As in TAVs, on the wall (Figure 4.11, green line and violet line), Patient 1 presents Von Mises stress values below 1.0x10^5 Pa, being the inferior wall connected to the fused leaflet more affected (with high Von Mises stress).

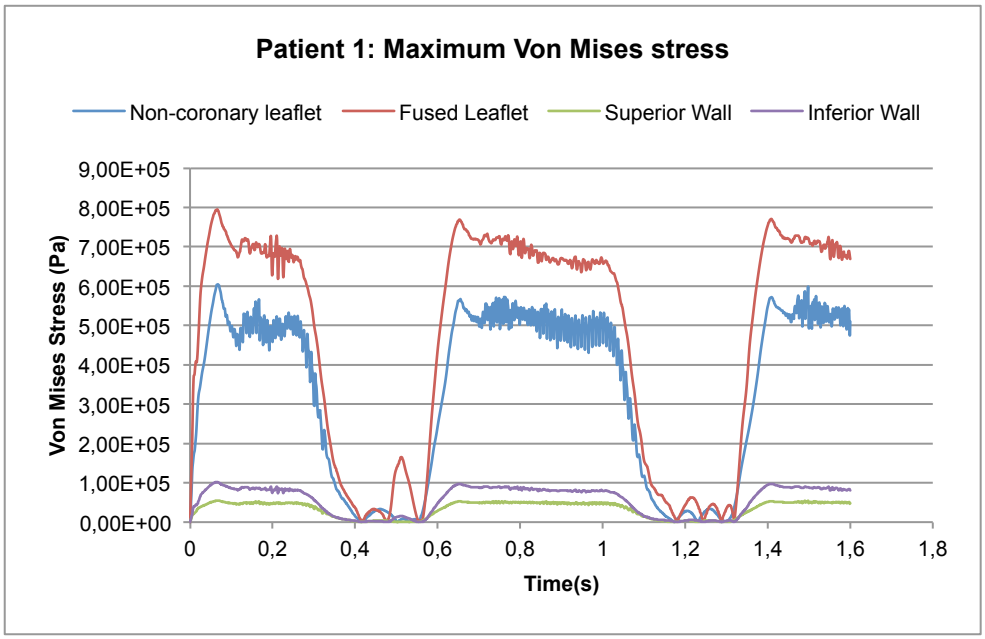

Figure 4.11. BAV 1: maximum Von Mises stress (Pa) during two cardiac cycles.

As in the case of TAVs, WSS was tested on the wall and on the leaflets with the same conclusion: high velocities imply high WSS. Non-coronary leaflet and fused leaflet present a maximum WSS average between 12 and 13.8 N/m^2 which corresponds to an increase greater than 70% (maximum WSS average was 3.5 N/m^2 in TAV 2). Superior aortic wall (Figure 4.12,A, green line) is more affected (maximum WSS average 6.0 N/m^2) due to the asymmetric flow (Figure 4.8, t=0.276s) in relation to the inferior aortic wall (Figure 4.12,A, violet line). Regarding the WSS before the leaflets (Figure 4.12, B), differences between both leaflets are around 2.0 N/m^2 with a maximum WSS value in average between 8 and 14 N/m^2; (ii) considering the wall after the leaflets, the superior wall is more affected during the cardiac cycle (Figure 4.12, C, blue line corresponding to the superior wall after the non-coronary leaflet).

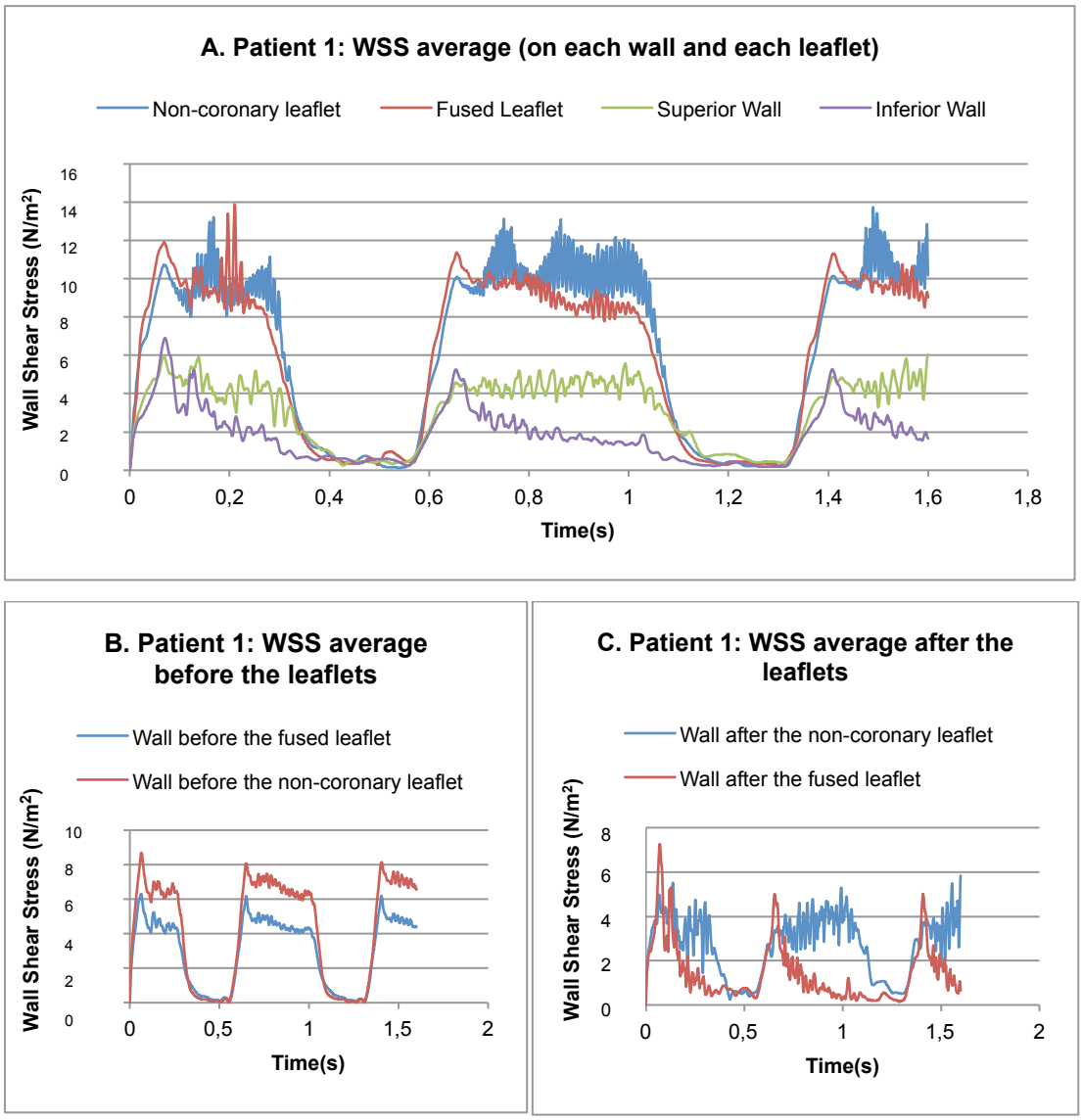

Figure 4.12. WSS average (superior and inferior leaflets, superior and inferior wall), for patient 1. (A) WSS average analysis along the aortic wall, before (B) and after the leaflets (C) during two cardiac cycles.

4.2.2. Patient 2 (6 years old, female)

Figure 4.13. (BAV 2, aortic root model of patient 2) shows the valve behaviour along one cardiac cycle. At t=0s the valve is closed, then at t=0.024s, due to the pressure gradient between outlet and inlet boundaries leaflets start opening, with a maximum velocity magnitude of 0.88 m/s, corresponding to an increase of 26.14% in comparison with the maximum velocity magnitude verified for TAV 2 (0.65 m/s). From this moment, there is a constant increase of the velocity and, consequently, at t=0.076s a maximum velocity magnitude 1.99 m/s is verified and a blood flow jet through the valvular orifice

(representing an increase of 22.1% in relation to TAV2). At t=0.116 s with a maximum velocity magnitude of 1.86 m/s (increase of 8.6% in relation to TAV2), the systolic jet that is formed is asymmetric due to the fused leaflet (longer length, larger thickness and increased stiffness compared with the non-coronary leaflet), that contributes to create vortices in the end of the inferior sinus. The maximum velocity magnitude of 2.02 m/s is verified at t=0.176 s (an increase of 35.64% in relation to TAV 2), having vortices that migrated from the tip of the leaflets to the ascending thoracic region. From this moment, the velocity magnitude starts to decrease having a constant deceleration phase, with the initial vortices migration along the BAV geometry (t=0.328 s to 0.557 s, maximum velocity magnitude of 1.43 m/s and 0.7 m/s, respectively). In Figure 4.13 we observe that the initial vortices created close to sinuses, give rise to the formation of new vortices, in particular, one vortex placed after each sinus and one bigger vortex close to the ascending thoracic aorta until the coaptation moment (t=0.328 s and t=0.557 s). At the coaptation moment, in comparison with TAV 2, BAV 2 presents an increase of 31.42% (from 0.48 m/s to 0.7 m/s). The created recirculation areas (t=0.557 s) have a close damaging effect on leaflets, due to the blood flow instabilities verified at the ascending thoracic aorta region. From t=0.568 s until 0.80s the valve opens, and the blood flows through the valvular orifice at t=0.633 s (the maximum velocity magnitude 1.31 m/s), at t=0.673s (it is 1.82 m/s), and at t=0.745 s (it is 1.94 m/s). Regarding the Von Mises stress, highest stresses are verified in the base of the cusps (when leaflets are opening) and the lowest stresses towards their respective free edges. For example, in the acceleration phase at t=0.076s and 0.116s, the maximum values are 590 KPa and 579 KPa, respectively, corresponding to an increase of 43.79% in relation to TAV2.

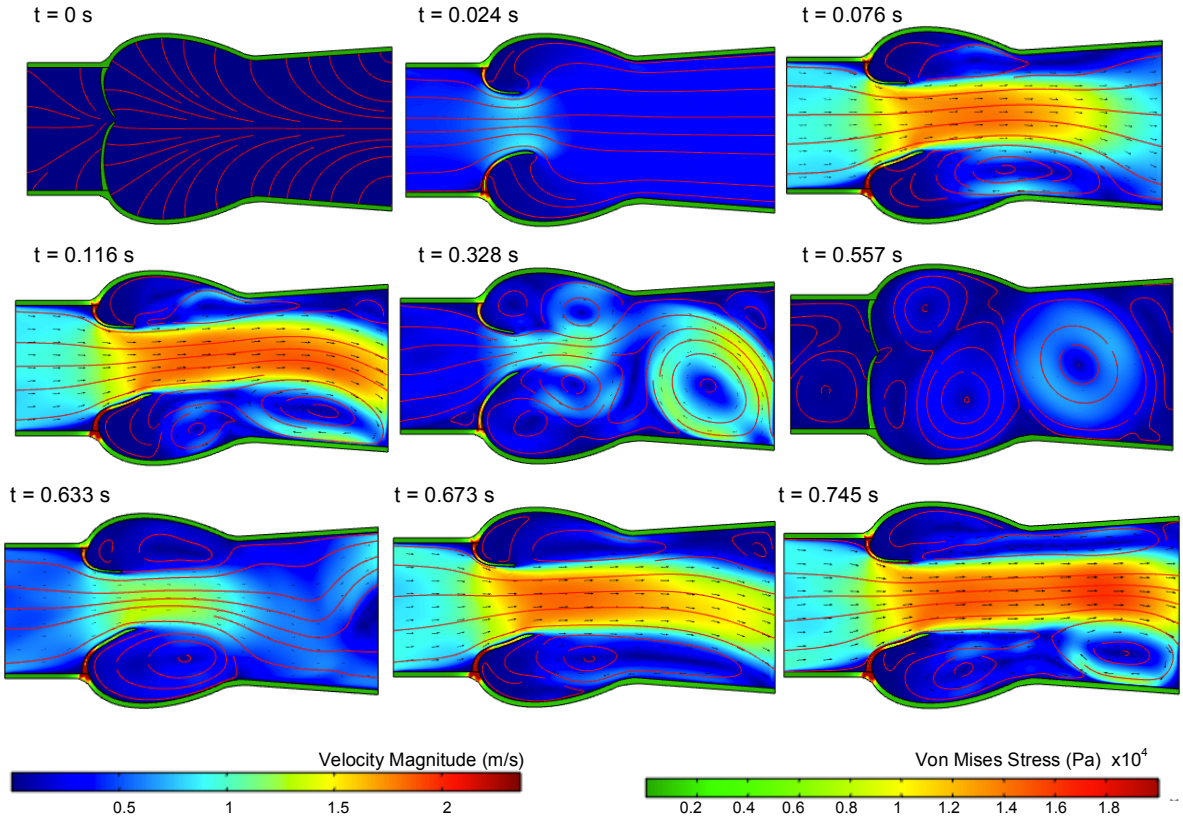

Figure 4.13. Aortic root model of BAV2: flow velocity, flow patterns (with the red streamlines) and Von Mises stress.

Figure 4.14 shows the WSS on the boundaries (leaflets and wall). Velocity increases, vortices and respective recirculation areas promote WSS effects (Figure 4.14, highlighted regions: sinuses end and ascending thoracic area). As on TAV models, WSS effects on leaflets are verified at the belly and the tip (Figure 4.10). At 0.076 s, maximum velocity magnitude is 1.8 m/s, the maximum WSS will be 59.0 N/m^2, representing an increase of 85.88%; and, at 0.116 s, values of velocity magnitude are close to 1.86 m/s, the WSS will be around 57.9 N/m^2, representing an increase of 82.03% comparing to TAV 2.

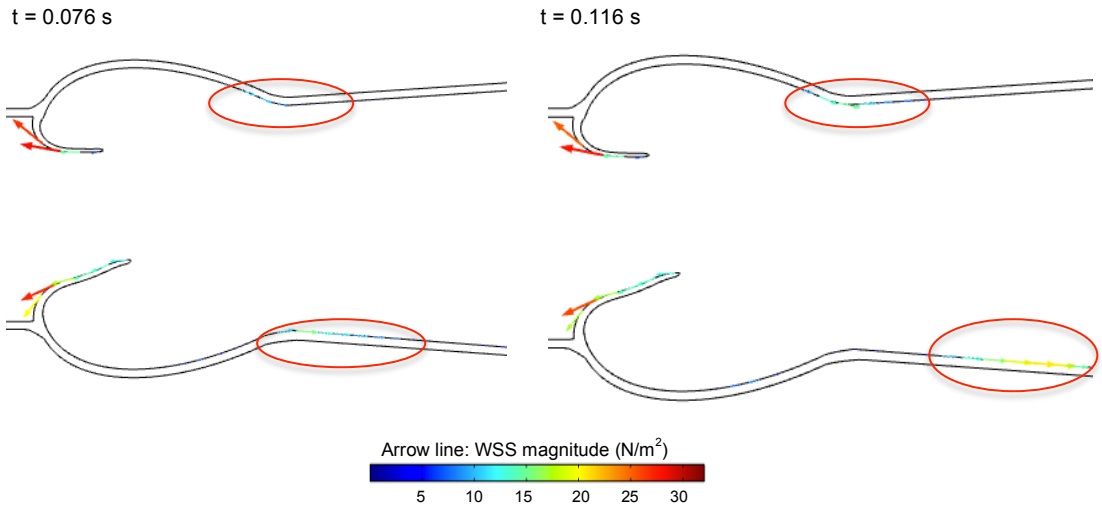

Figure 4.14. BAV 2: wall shear stress (N/m^2) for the valve.

Figure 4.15. shows the Von Mises stress on BAV 2 observed during two cardiac cycles. Fused leaflet (Figure 4.15, red line) has maximum Von Mises stress greater than 9.0x10^5 Pa (more 83.3% than on the inferior wall), the non-coronary leaflet (blue line in Figure 4.15) has maximum Von Mises stress close to 4.0x10^5 Pa (more 81.25% than on the superior wall). There is an evident difference between the stresses applied to the non-coronary leaflet and the fused leaflet (5.0x10^5 Pa – Figure 4.15, between the red and blue line). Von Mises stress on the fused leaflet increased 44.4% compared with TAV 2, and on the non-coronary leaflet is approximately the same (around 4.0x10^5 Pa). This explains the stresses differences between an healthy leaflet and a pathologic one. Regarding the walls, the inferior wall (Figure 4.15, violet line), connected with the fused leaflet is more affected.

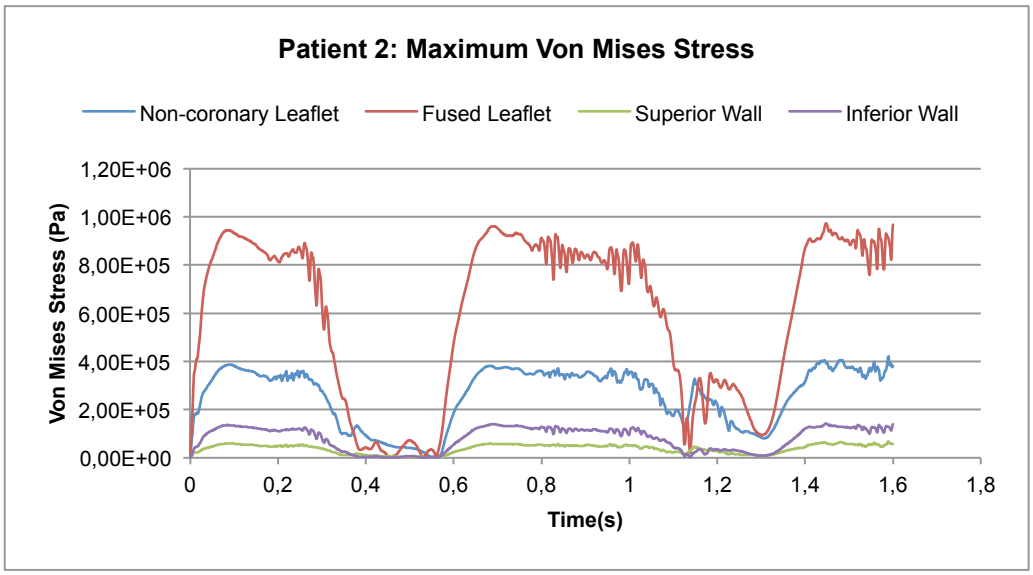

Figure 4.15. BAV 2: maximum Von Mises stress (Pa) during two cardiac cycles.

As we verified previously, high velocities imply high WSS. The WSS was tested on the leaflets and on the wall during two cardiac cycles. Non-coronary and fused leaflets present a maximum WSS average between 8.0 and 10.0 N/m^2 which corresponds to an increase greater than 65% (maximum WSS average was 3.5 N/m^2 for TAV 2). Superior and inferior aortic wall (Figure 4.16, A, green and violet lines) are affected (maximum WSS average of 6.0 N/m^2) due to the asymmetric flow caused by recirculation regions. WSS before the leaflets (Figure 4.16 B): (i) instabilities (between t=1 and t=1.5 s) are verified; they are promoted by asymmetric blood flow from the first cardiac cycle, with maximum WSS in average between 6.0 and 8.0 N/m^2; (ii) considering the wall after the leaflets, the inferior wall is affected when leaflets are opening (Figure 4.16.C, red line) and low WSS values are verified when leaflets are closed.

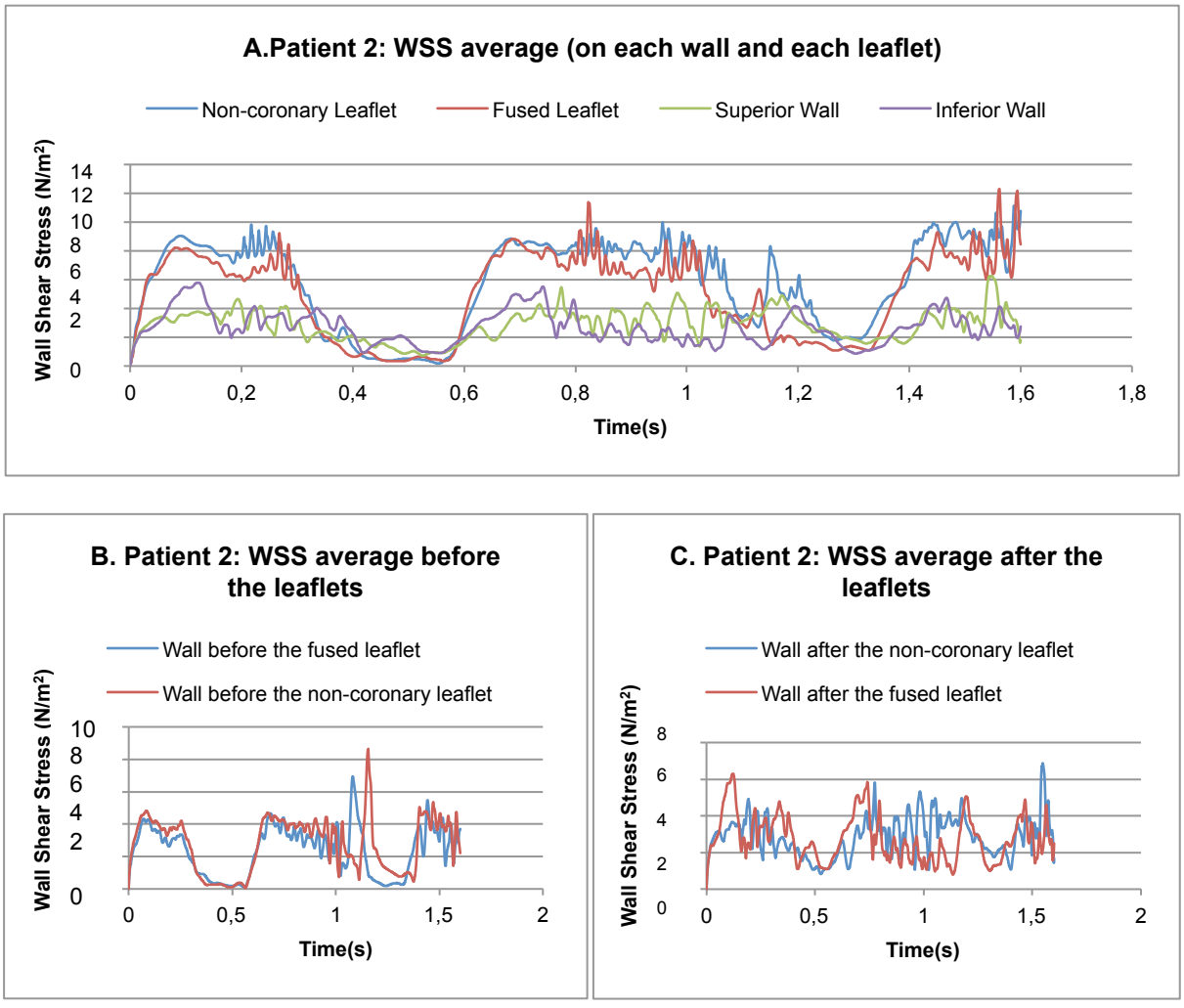

Figure 4.16. WSS average (superior and inferior leaflets, superior and inferior wall), for patient 2. (A) WSS average analysis along the aortic wall, before (B) and after the leaflets (C) during two cardiac cycles.

4.2.3. Patient 3 (11 years old, female)

Figure 4.17. (BAV 3, aortic root model of patient 3) explains the valve evolution during one cardiac cycle. At t=0 s the valve is closed, but at t=0.024s leaflets start to open (maximum velocity magnitude of 0.95 m/s, with an increase of 31.57% in relation to TAV 2). At t=0.076 s (maximum velocity magnitude is 1.99m/s, with an increase of 22.11% in relation to TAV 2). At this moment the systolic jet formed is asymmetric, due to the characteristics of the fused leaflet, and at the same time vortices are created due to the blood flow through the valvular orifice. There are constant velocity oscillations, for example, at t=0.116s the maximum velocity magnitude is 1.77 m/s (velocity decreases 3.95% in relation to TAV 2), at t=0.252s the maximum velocity magnitude is 1.83 m/s (it increases 14.21% in relation to TAV 2) and at t=0.308s it is 1.56 m/s (it increases 10.89%). These instabilities on the flow, with constant oscillations, promote recirculation regions that change during the cardiac cycle and that are formed in different places, preventing a normal coaptation moment. After t=0.308 s, the velocity peak happens at t=0.320 s, velocity magnitude increases to 2.33 m/s (an increase of 40.77% in relation to TAV2), and after this moment starts to decrease slowly until the coaptation moment (t=0.537s, with a maximum velocity magnitude of 0.63 m/s - an increase of 23.80% in relation to TAV 2). At the coaptation moment, recirculation regions (focused on the superior wall and close to the ascending thoracic region) amplify the asymmetry of BAV flow dynamics. Leaflets open and at t=0.673s (maximum velocity of 2.06 m/s, with an increase of 24.75% in relation to TAV 2) the blood flow asymmetry is observed, being more evident at t=0.741s (maximum velocity magnitude of 1.96 m/s, with an increase of 13.77% in relation to TAV 2). The highest Von Mises stress is verified at t=0.076 s, 706 KPa, and at t=0.116s, the maximum value is 597 KPa, representing an increase of 53.82% and 41.03% compared to TAV2, respectively.

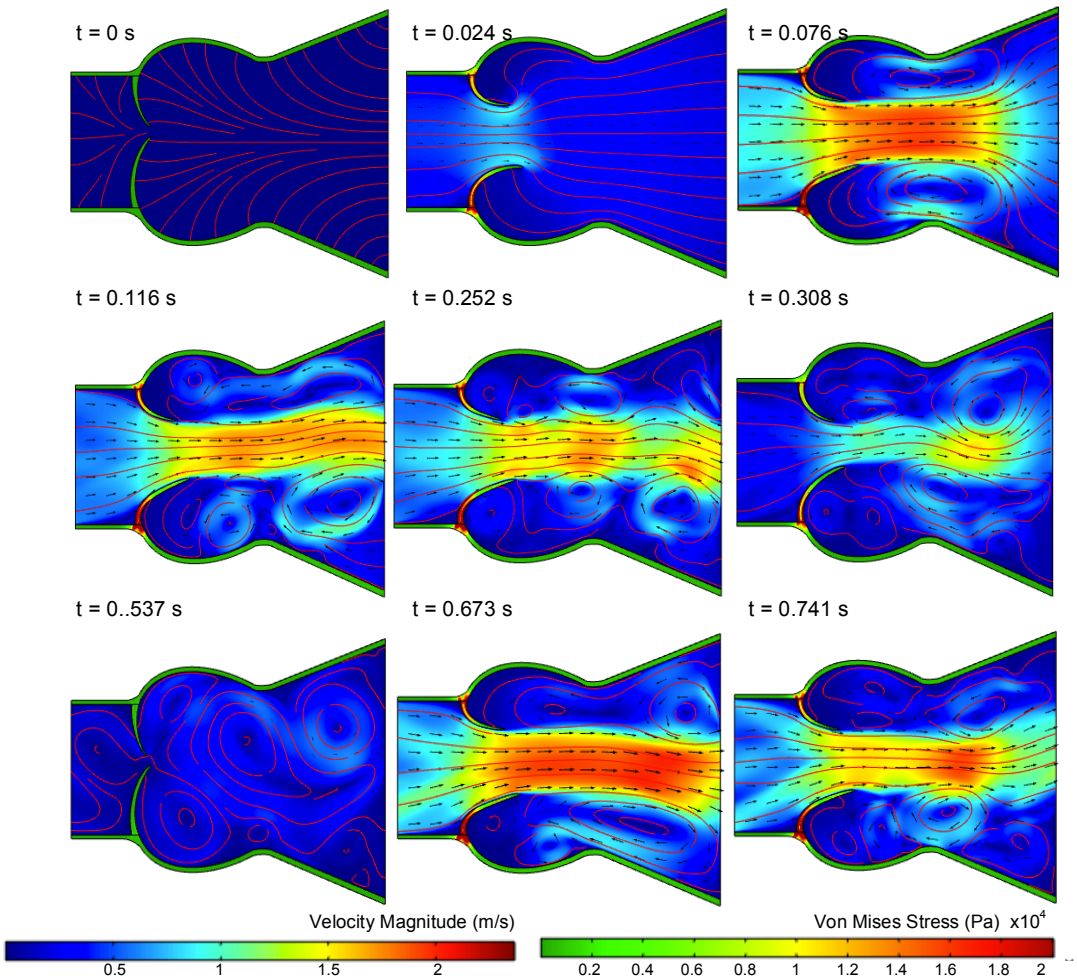

Figure 4.17. Aortic root model of BAV 3: flow velocity, flow patterns (with the red streamlines) and Von Mises stress.

WSS effects are evident on leaflets, but also on the sinotubular junction and on the wall of the ascending thoracic region (Figure 4.18) due to the recirculation regions that are created during the cardiac cycle. At t=0.076 s and t=0.252 s, the maximum WSS values are 26.6 and 27.6 N/m^2 corresponding to an increase of 66.42% and 67.75% in relation to TAV 2, respectively.

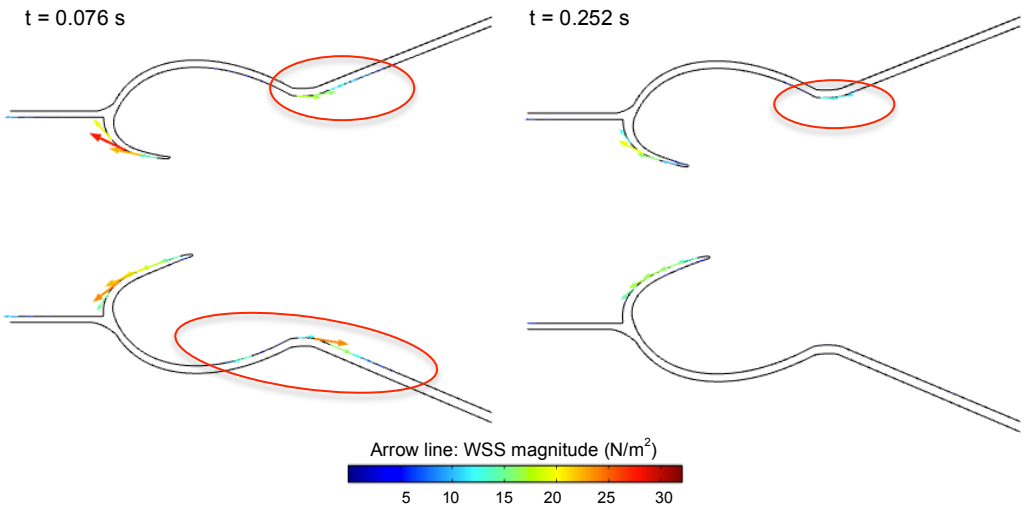

Figure 4.18. BAV 3: Wall Shear Stress (N/m^2) for the valve.

Figure 4.19. shows the Von Mises stress observed during two cardiac cycles. Von Mises stress on the fused leaflet (red line) has a maximum value close to 1.2x10^9 Pa (more 83.3% than on the inferior wall - Figure 4.9 – violet line), the non-coronary leaflet (blue line in Figure 4.19) has a maximum Von Mises stress of 5.0x10^5 Pa (more 80% than on the superior wall – Figure 4.19, green line). There is an evident difference between the stresses applied to the non-coronary leaflet and the fused leaflet (5. 0x10^5 Pa – Figure 4.15, between the red and blue lines). Von Mises stress on the fused leaflet increased 58% comparing with TAV 2, and on the non-coronary leaflet increased 20%. Regarding the walls, the inferior wall (Figure 4.19, violet line), connected with the fused leaflet, is more affected.

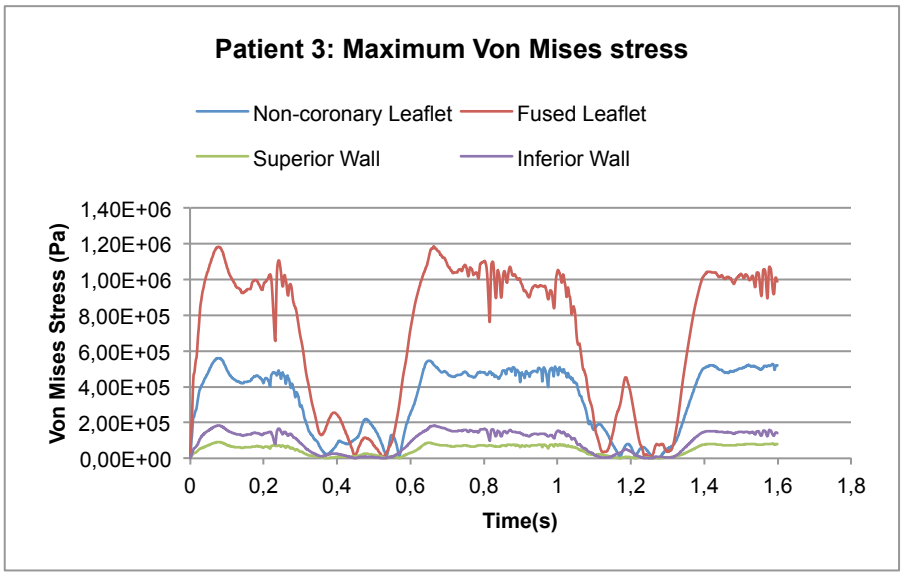

Figure 4.19. BAV 3: maximum Von Mises stress (Pa) during two cardiac cycles.

Regarding the WSS, the non-coronary leaflet and the fused leaflet present a maximum WSS average around 8.3 N/m^2 (with some WSS peaks close to 12.0 N/m^2) which corresponds to an increase greater than 57% (maximum WSS average was 3.5 N/m^2 for TAV 2). Superior aortic wall (Figure 4.20, A, green line) is more affected (maximum WSS average 4.4 N/m^2) due to the asymmetric flow (mainly in the second cardiac cycle) in relation to the inferior aortic wall (Figure 4.20,A, violet line). In the case of the WSS before the leaflets (Figure 4.20, B), there are no evident differences between both leaflets, but between t=0.6s and t=1s instabilities on the wall are verified, with maximum WSS in average of 3.4 N/m^2; (ii) considering the wall after the leaflets, the superior wall is more affected, due to the blood flow asymmetry on the ascending thoracic region, with maximum values around 5.5 N/m^2 (Figure 4.20, C, the blue line corresponding to the superior wall, after the non-coronary leaflet).

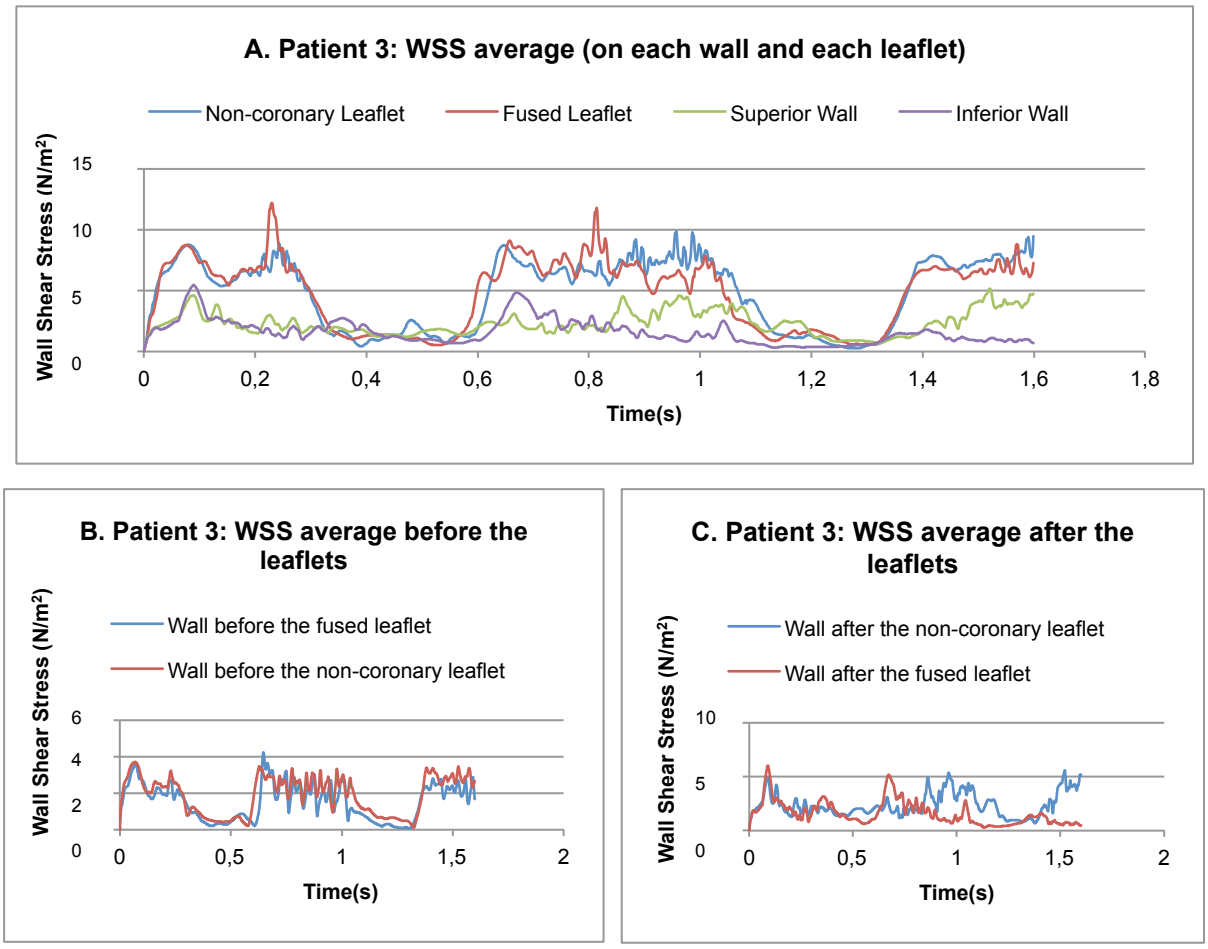

Figure 4.20. WSS average (superior and inferior leaflets, superior and inferior wall), according for patient 3: (A) WSS average analysis along the aortic wall, before (B) and after the leaflets (C) during two cardiac cycles.

4.2.4. Patient 4 (19 years old, male)

Figure 4.21. (BAV 4, aortic root model for patient 4) shows the BAV behavior during one cardiac cycle. At t=0s BAV 4 is closed. Due to the pressure traction at the outlet boundary, leaflets start opening at t=0.024s, with a maximum velocity magnitude of 0.76 m/s (an increase of 14.47% in relation to TAV 2). At t=0.116 s, with a maximum velocity magnitude of 1.86 m/s (an increase of 8.6% comparing with TAV 2), leaflets are completely opened and blood recirculation regions start to be formed inside de sinuses. At t=0.144s, with a maximum velocity magnitude of 1.96 m/s (an increase of 13.27% comparing with TAV2), a vortex caused by fused leaflet contributes to blood jet asymmetry that will have consequences on the superior wall. Velocity starts to decrease and at t=0.252s, with a maximum velocity magnitude value of 1.71 m/s (an increase of 8.19% compared to TAV2) and blood jet asymmetry is emphasized. At t=0.409s (maximum velocity of 1.06m/s, an increase of 32% comparing with TAV2) both leaflets, but mainly the fused leaflet, are responsible for the formation of new recirculation regions (observe the big vortex created at the ascending thoracic region) until the coaptation moment, at t=0.549s (maximum velocity magnitude of 0.93 m/s, an increase of 43.31%). Due to these vortices, there are blood instabilities that prevent a normal coaptation and, consequently, leaflets do not close completely. Then at t=0.649s (maximum velocity magnitude of 1.27 m/s, a decrease of 6.61% compared to TAV2) the blood jet is formed from the valvular orifice presenting asymmetry until the end, with a constant increase of the velocity at t=0.697s (maximum value 1.81 m/s, an increase of 8.29%, compared to TAV2) and at t=0.773s (maximum value 1.91 m/s, an increase of 10.47%, compared to TAV2). Note that regions of constant recirculation with the respective rolling of the streamlines around the vortices generated inside the aortic root (t=0.409s) are regions where the blood flow is stagnant or in turbulence[80]. Regarding the Von Mises stresses, the highest values are verified at t=0.116s and t=0.144s, with 576KPa and 554 KPa, respectively, representing an increase of 38.8% and 38.4% comparing with TAV2.

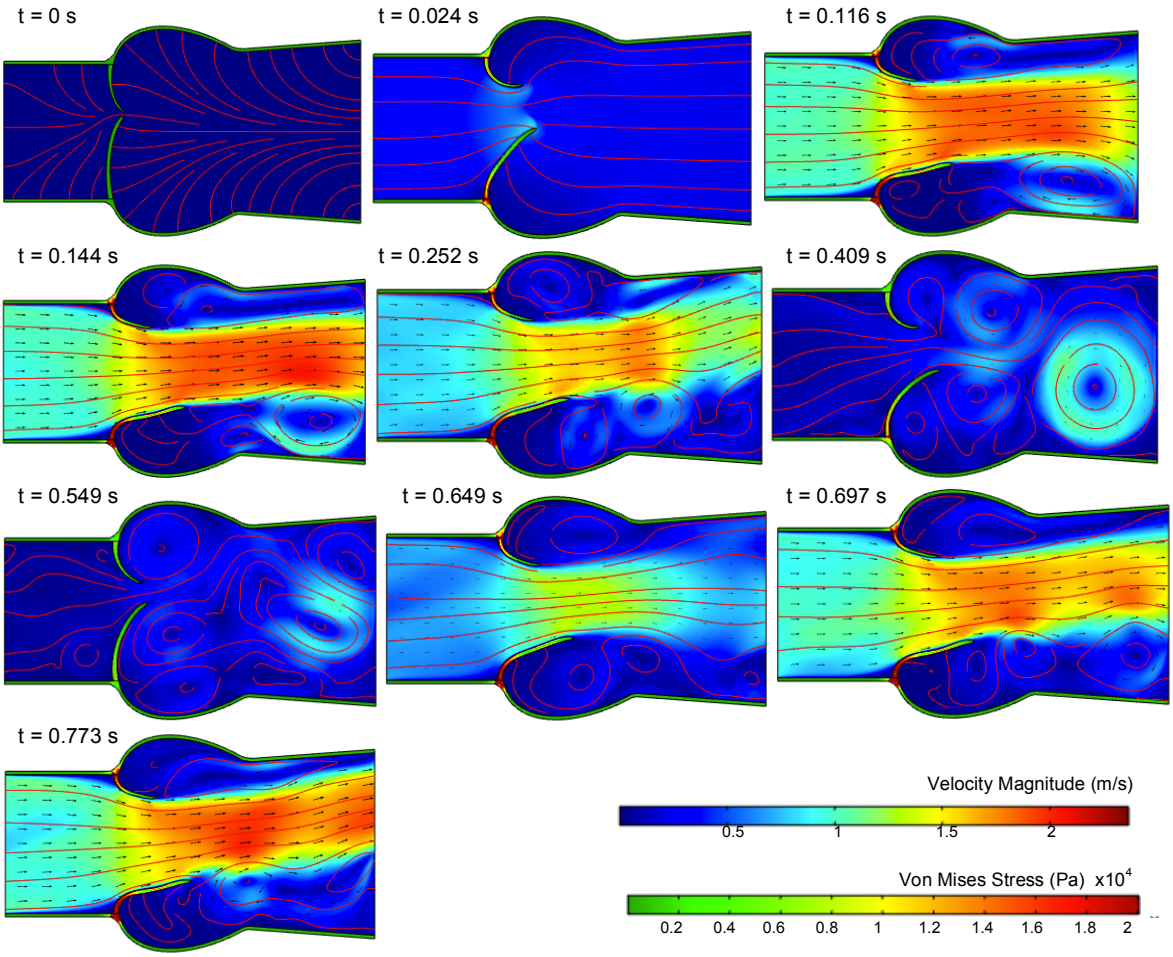

Figure 4.21. Aortic root model of BAV4: flow velocity, flow patterns (with the red streamlines) and Von Mises stress.

WSS was analyzed on the leaflets and on the wall (Figure 4.22) as in the previous BAVs cases. Leaflets due to the contact with the blood are more affected to high velocities; walls were affected by recirculation regions and by the blood flow jet asymmetry (Figure 4.22, highlighted regions placed mainly at the ascending thoracic aortic region). For example, at t=0.116s and t=0.144s, the maximum WSS was 32.3 N/m^2 (an increase of 67.88% comparing with TAV2) and 28.6 N/m^2 (an increase of 65.03% comparing with TAV2).

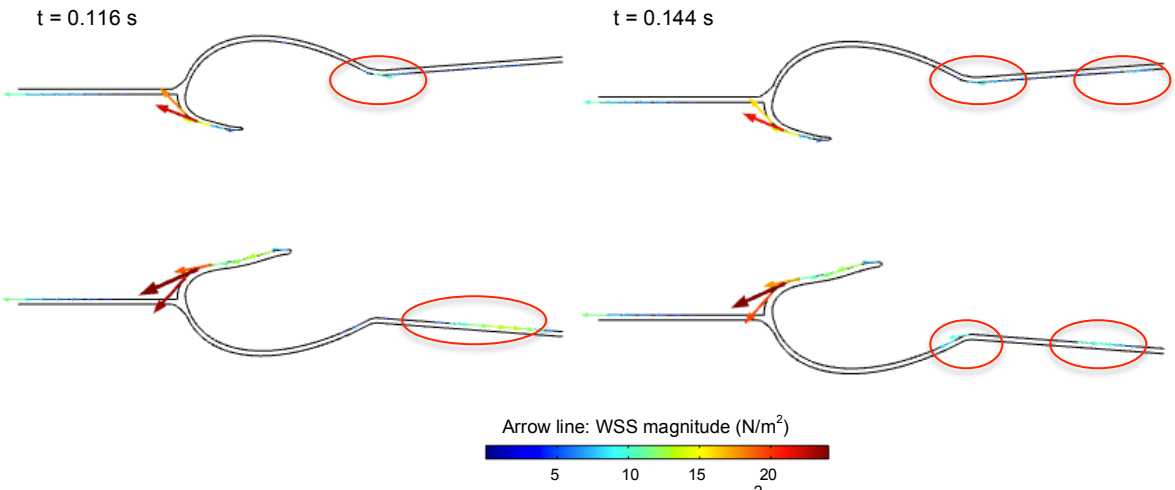

Figure 4.22. BAV 4: Wall Shear Stress (N/m^2) for the valve.

Considering two cardiac cycles, high von Mises stress values are observed with maximum velocities when leaflets are open (Figure 4.23) and low Von Mises stress when leaflets are closed. On fused leaflet (Figure 4.23, red line) maximum Von Mises stress values is higher than 1.0x10^6 Pa and on the non-coronary leaflet (Figure 4.23, blue line) the maximum Von Mises stress is approximately 6.0x10^5 Pa. Von Mises stress on the leaflets are greater than 90% in comparison with the aortic wall (more 10% in relation to TAV 2). On the wall (Figure 4.23, green line and violet line), the maximum Von Mises stress is 2.0x10^5 Pa, being the inferior (violet line) wall that is connected with the fused leaflet more affected than the non-coronary leaflet.

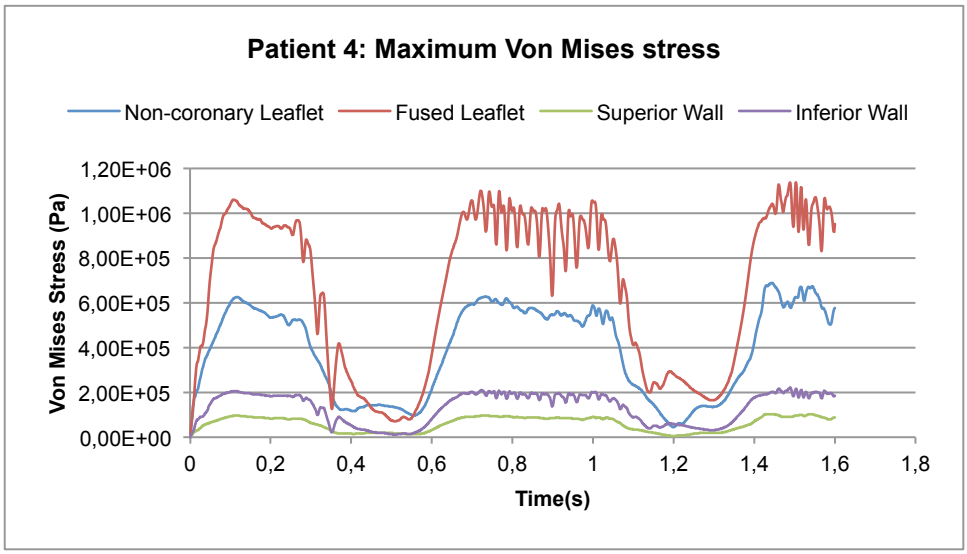

Figure 4.23. BAV 4: maximum Von Mises stress (Pa) during two cardiac cycles.

Regarding the WSS, the non-coronary leaflet and the fused leaflet present a maximum WSS average between 6.0 and 8.0 N/m^2 which corresponds to an increase greater than 41.7% (maximum WSS average was 3.5 N/m^2 in TAV 2). Superior aortic wall (Figure 4.24,A, green line) is more affected (maximum WSS average 4.3 N/m^2) due to the asymmetric flow (Figure 4.21, t=0.144s, 0.252s, 0.697s and 0.773s) in relation to the inferior aortic wall (Figure 4.24,A, violet line). WSS before the leaflets (Figure 4.24, B), shows no differences between both leaflets, with a maximum WSS in average between 5.1 and 60 N/m^2; (ii) considering the wall after the leaflets, the superior wall is more affected during all the cardiac cycle (Figure 4.24, C, blue line corresponding to the superior wall after the non-coronary leaflet) due to the asymmetric blood effects (previously justified in Figure 4.21).

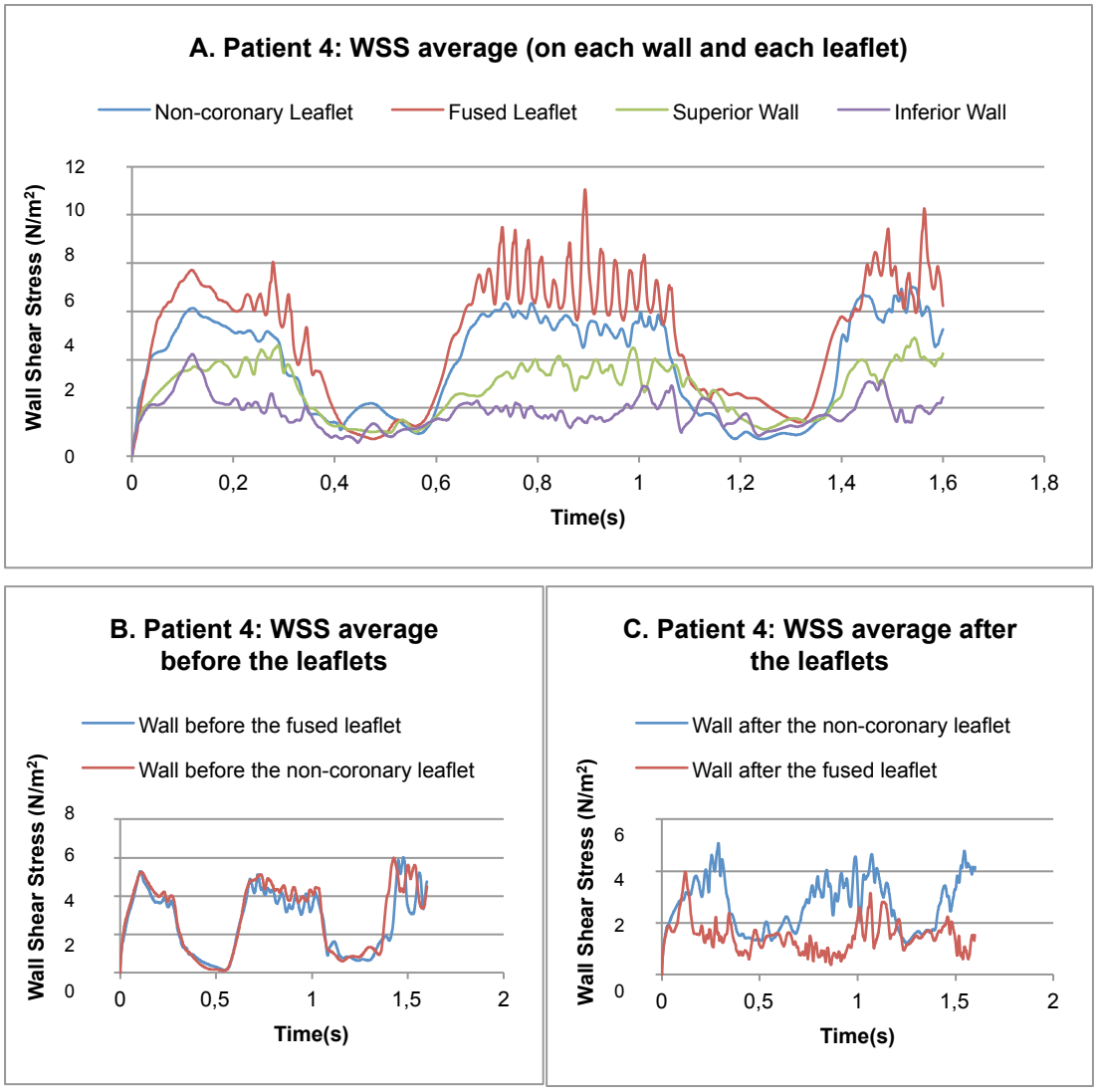

Figure 4.24. WSS average (superior and inferior leaflets, superior and inferior wall), for patient 4. (A) WSS average analysis along the aortic wall, before (B) and after the leaflets (C) during two cardiac cycles.

4.2.5. Patient 5 (22 years old, female)

Figure 4.25 (BAV 5, aortic root model of patient 5) shows the bicuspid valve behavior. At t=0s leaflets are closed, at t=0.024s leaflets are opening and there is a blood jet formation with the maximum velocity magnitude of 0.79 m/s (increase of 17.72% comparing with TAV2). Velocity magnitude increases from t=0.076s with a maximum value of 1.68 m/s (an increase of 7.74% comparing with TAV 2) until t=0.116s with a maximum velocity magnitude of 2.11 m/s (an increase of 19.43% comparing with TAV2). Recirculation regions are created since t=0.076s. The systolic jet is totally asymmetric due to the fused leaflet that causes this effect, and it also causes a vortex with larger proportions, close to the sinotubular junction, which propagates along the BAV geometry. At t=0.148 s a velocity peak of 2.48 m/s is verified. From this moment until the coaptation, there is a deceleration phase, at t=0.553 s with a maximum velocity magnitude of 0.76 m/s (an increase of 36.84%). Initial generated vortices gives rise to the formation of new vortices that prevent a normal coaptation of the leaflets, causing flow instability focused on the downstream channel (that was considered as the ascending thoracic aorta). After the coaptation moment, there is a successive increase of the velocity magnitude, generating again an asymmetric blood jet: at t=0.625s, t=0.673s and 0.729s with a maximum flow velocity of 1.07 m/s (same value to TAV2), 1.68 m/s (an increase of 7.74% comparing with TAV2) and 2.07m/s (an increase of 16.43% comparing with TAV2), respectively. Regarding the Von Mises stress, maximum values are verified when blood flow has high velocity magnitudes at t=0.076s and t=0.116s, with 808 KPa and 835 KPa, respectively.

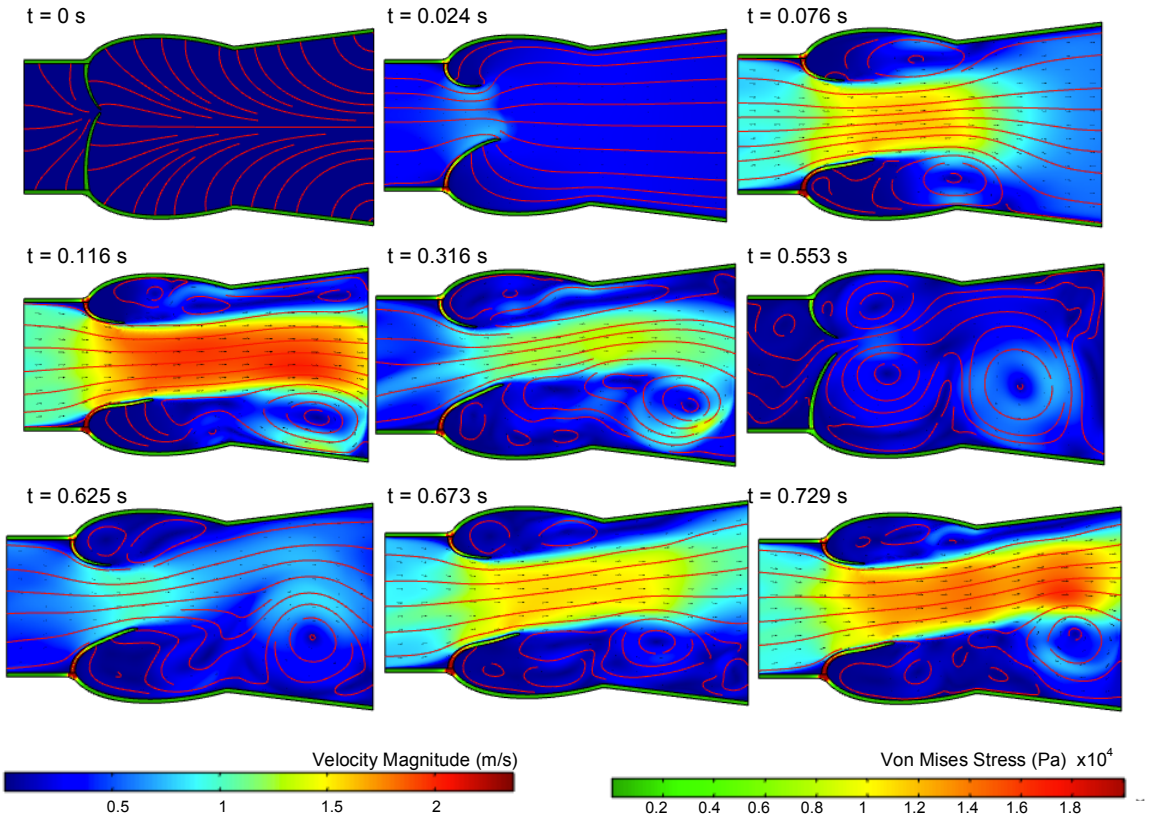

Figure 4.25. Aortic root model of BAV5: flow velocity, flow patterns (with the red streamlines) and Von Mises stress.

The WSS was analyzed in Figure 4.26, highlighting regions on the ascending thoracic region. At 0,076 s, the maximum velocity magnitude is 1.68 m/s, the WSS is 31.7 N/m^2 representing an increase of 71.82% compared to TAV2; and, at 0.116s, the value of the velocity magnitude is 2.11 m/s, the WSS is 37.0 N/m^2, representing an increase of 71,84% compared to TAV 2.

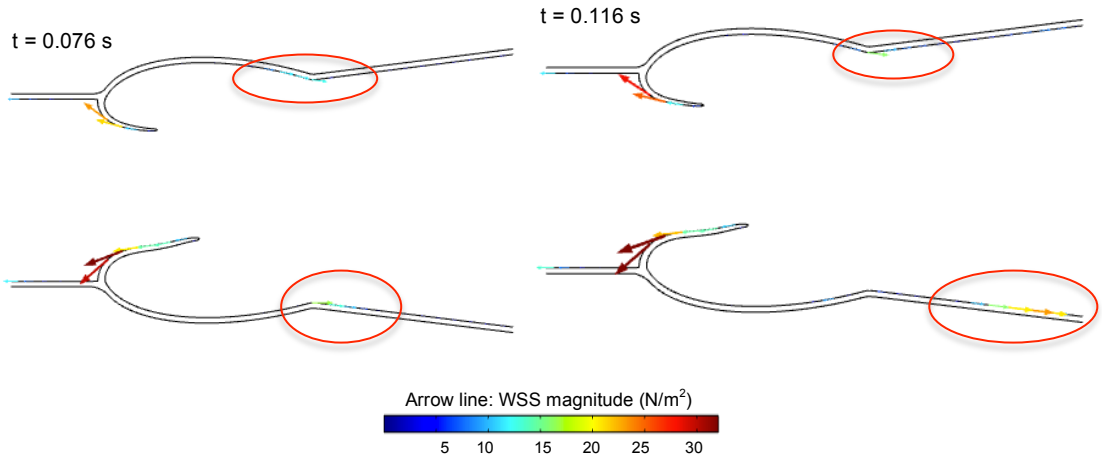

Figure 4.26. BAV 5: Wall Shear Stress (N/m^2) for valve.

As in the previous cases, considering two cardiac cycles, the maximum Von Mises stress values are greater on the fused leaflet (maximum Von Mises stress approximately $1.2x10^6$ Pa), than on the non-coronary leaflet (where the maximum Von Mises stress is approximately $6.0x10^5$ Pa). The Von Mises stress on the leaflets is 83.3% higher in comparison with the aortic wall (approximately 4% in relation to TAV 2). On the wall (Figure 4.27, green line and violet line), high Von Mises stress is approximately $2.0x10^5$ Pa.

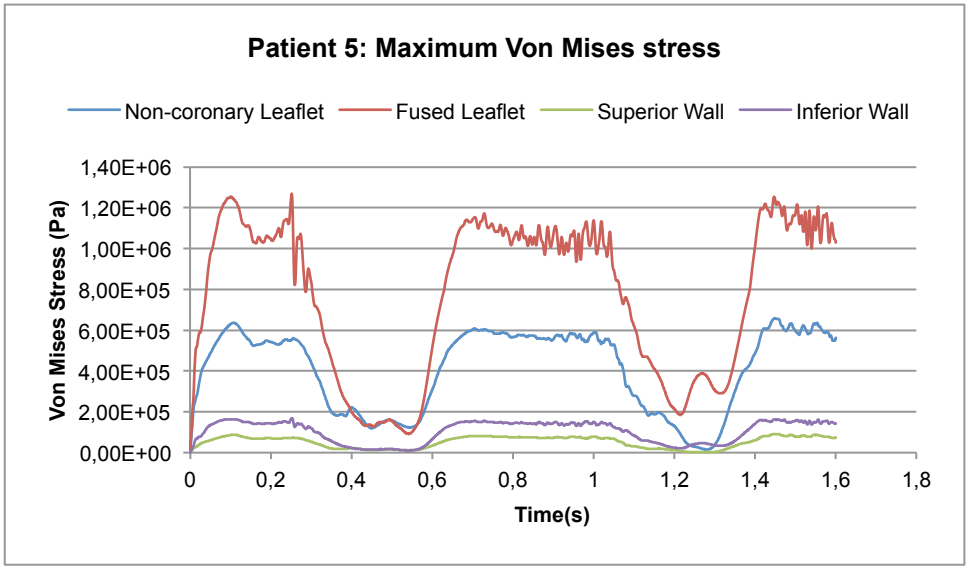

Figure 4.27. BAV 5: maximum Von Mises stress (Pa) during two cardiac cycles.

Regarding the WSS, the non-coronary leaflet and the fused leaflet present a maximum WSS average between 7.8 and 9.8 N/m^2 which corresponds to an increase greater than 67%, comparing to TAV 2. Superior aortic wall (Figure 4.28,A, green line) has high WSS values (maximum WSS average 5 N/m^2,) in relation to the inferior aortic wall during the whole cardiac cycle (Figure 4.12,A, violet line). On the wall, before the leaflets (Figure 4.28, B), WSS values are close for both leaflets, with maximum WSS in average around 5.2 N/m^2; (ii) considering the wall after the leaflets, due to the blood flow asymmetry and some instabilities on the leaflets due to recirculation regions, the superior wall is more affected (Figure 4.28, C, blue line corresponding to the superior wall after the non-coronary leaflet).

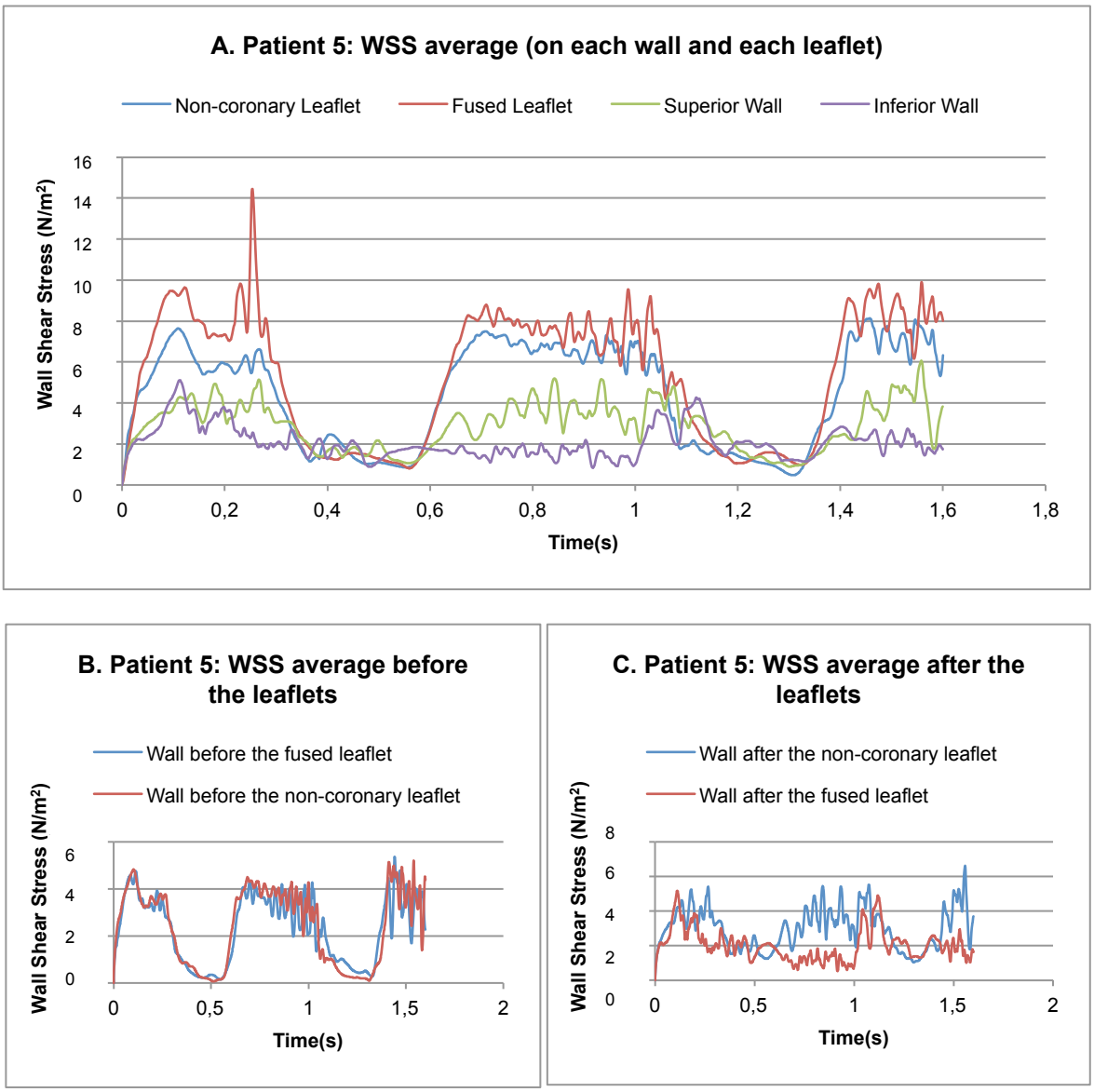

Figure 4.28. WSS average (superior and inferior leaflets, superior and inferior wall), for patient 5. (A) WSS average analysis along the aortic wall, before (B) and after the leaflets (C) during two cardiac cycles.

4.2.6. BAV 6 (27 years old, male)

Figure 4.29. (BAV 6, aortic root model for patient 6) describes the corresponding aortic valve behavior during one cardiac cycle. At t=0 s BAV 6 is closed. At t=0.036s leaflets are opening, with the maximum velocity magnitude of 0.8 m/s, an decrease of 18.37% in comparison with the maximum velocity magnitude verified in TAV 2. At t=0.116 s the blood jet is completely formed, with the leaflets completely open, leading to a maximum flow velocity of 1.7m/s (equal velocity on TAV 2). At t=0.3s

there is a velocity peak of 1.96 m/s (an increase of 28.57%, comparing to TAV2) with vortices close to the region of the ascending thoracic aorta that causes instabilities in the blood flow until the coaptation, t=0.348s and t=0.557s. Due to the gradient pressure reversion, the velocity magnitude decreases: at t=0.348s, the maximum velocity magnitude is 1.43m/s (an increase of 17.48%, comparing to TAV2) and at t=0.557s, the maximum velocity magnitude is 0.64 m/s (an increase of 25%, comparing to TAV2). Due to the aortic root dimensions, the leaflets asymmetry, respective calcification applied to fused leaflet, and the vortices effects, at t=0.557s leaflets do not close completely, having regurgitation with these boundary conditions. After this moment, at t=0.669s and t=0.733s, there is a constant increase of the velocity magnitude, with the blood jet genesis. Comparing with TAV2, at 0.699 s there is a maximum velocity magnitude of 1.33 m/s (a decrease of 12.5%) and at 0.733 s there is a maximum velocity magnitude of 2.14 m/s (an increase of 19.15%). Regarding the Von Mises stress, as in the previous analysis, at the peak velocity, the highest Von Mises stress is verified: at t=0.116s, t=0.3s, t=0.733s, with maximum values of 485 KPa, 378 KPa and 532 KPa, respectively, corresponding to an increase greater than 27.25%, comparing with TAV2.

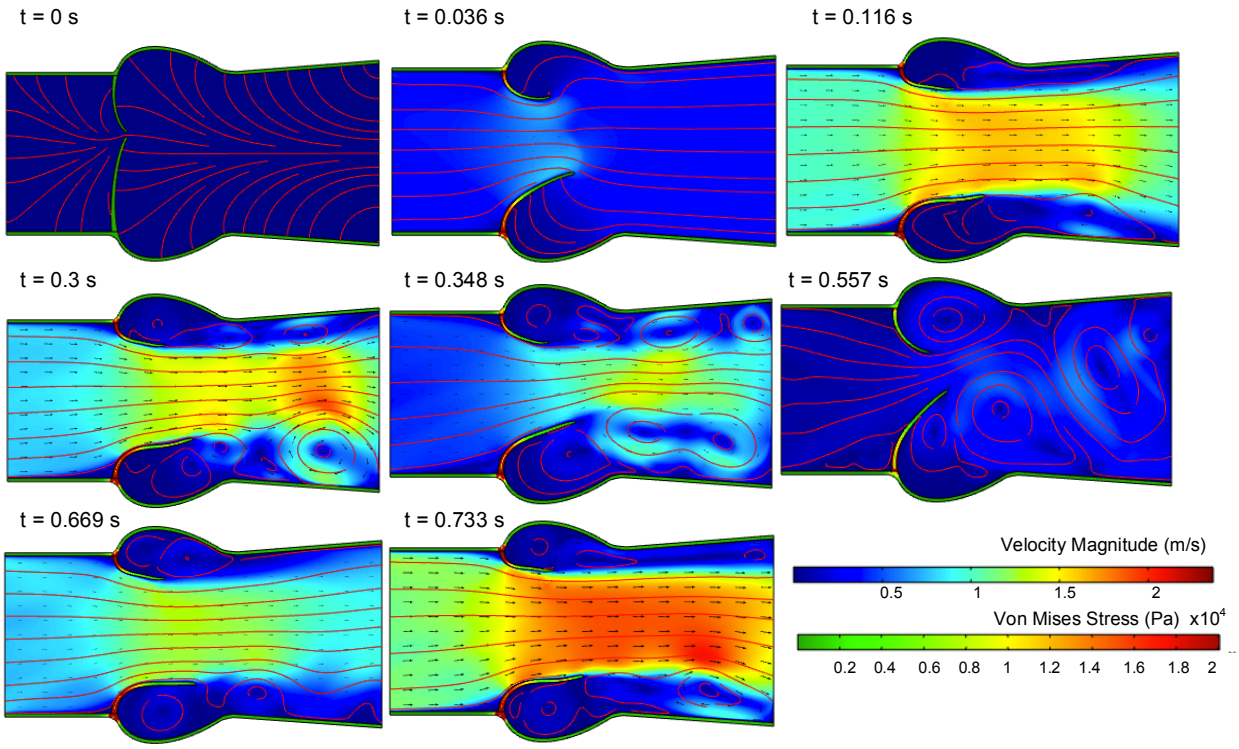

Figure 4.29. Aortic root model of BAV6: flow velocity, flow patterns (with the red streamlines), Von Mises stress.

The WSS has effects on the leaflets and on the ascending thoracic region (Figure 4.30, highlighted areas), but this is the BAV with less WSS effects for the same boundary conditions (justified by the respective model dimensions). Maximum WSS values are between 8.06 and 29.5 N/m^2. For example, at 0.116 s the maximum velocity magnitude is 1.7 m/s (same velocity on TAV2), the WSS will be 26.8 N/m^2, (representing an increase of 61.19%); and, at 0.3 s, values of the velocity magnitude are close to 1.96 m/s, the WSS is around 20.8 N/m^2, representing an increase of 65.14%, comparing with TAV 2.

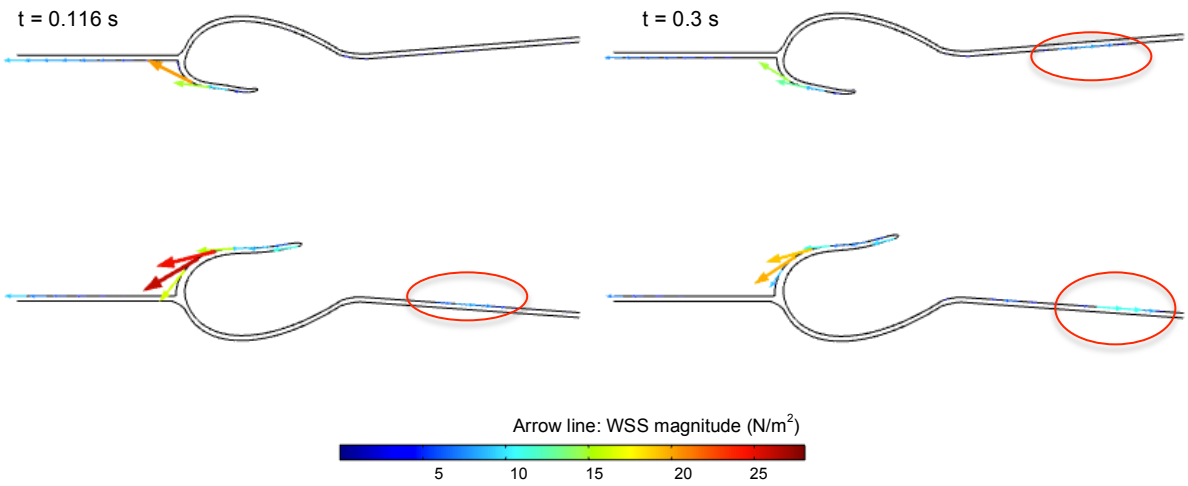

Figure 4.30. BAV 6: Wall Shear Stress (N/m^2) for valve.

As in the previous cases, high von Mises stress values are verified with maximum velocities when leaflets are open (Figure 4.31). Von Mises stresses are similar on the fused leaflet and on the non-coronary leaflet (where the maximum Von Mises stress is approximately between 8.0x10^5 Pa and 1.1x10^6 Pa). However, calcified leaflet is subject to more stresses (Figure 4.31, red line). Von Mises stress on the leaflets is 86,36% higher in comparison with the aortic wall (more 6.36% in relation to TAV 2). On the wall (Figure 4.31, green and violet lines), Von Mises stress values are 2,0x10^5 Pa.

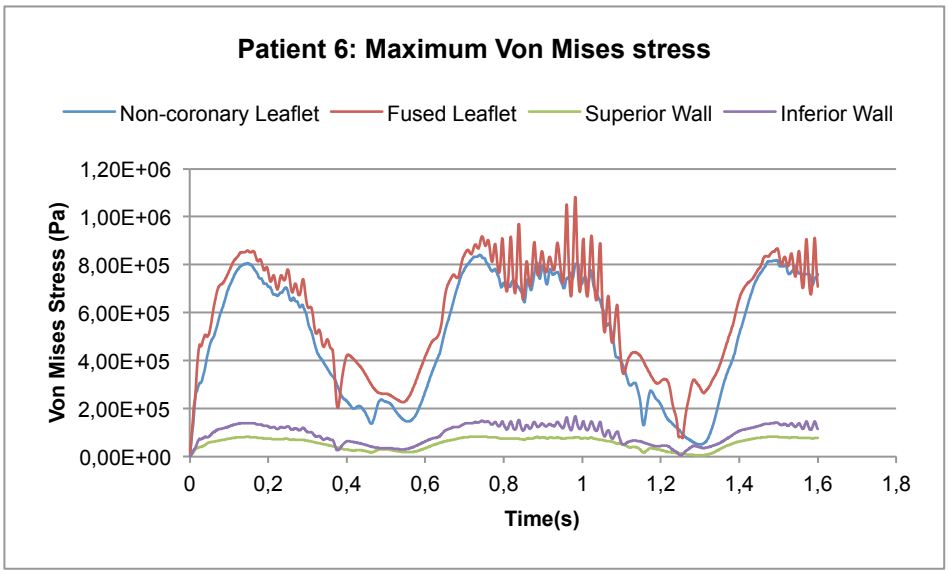

Figure 4.31. BAV 6: maximum Von Mises stress (Pa) during two cardiac cycles.

Regarding the WSS, non-coronary leaflet and fused leaflet present a maximum WSS average between 6.0 and 9.8 N/m^2 which corresponds to an increase greater than 58.33% (the maximum WSS average was 3.5 N/m^2 for TAV 2). Superior and inferior aortic wall (Figure 4.31,A, green and violet lines, respectively) have maximum WSS average close to 3.8 N/m^2 in Figure 4.32, B. WSS differences, on the wall, before the leaflets, and between both leaflets is around 3.0 N/m^2, with maximum WSS in average between 4.0 and 7.0 N/m^2; (ii) considering the wall after the leaflets, the superior and inferior walls are affected on a similar way during the cardiac cycle, with maximum WSS average values around 3.5 N/m^2.

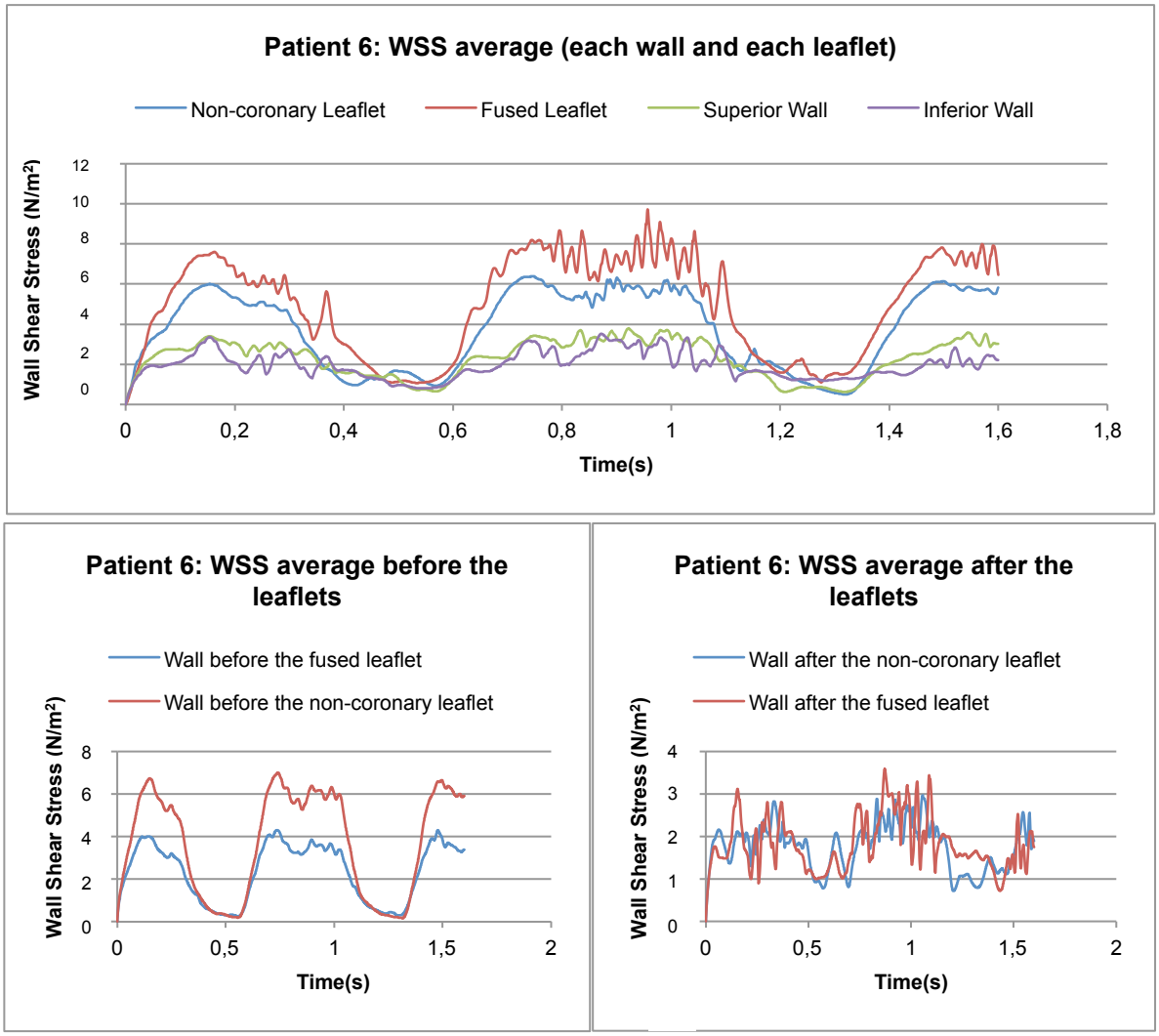

Figure 4.32. WSS average (superior and inferior leaflets, superior and inferior wall), for patient 6. (A) WSS average analysis along the aortic wall, before (B) and after the leaflets (C) during two cardiac cycles.

4.2.7. OSI analysis

Figures 4.33.A shows the OSI variation for all models (TAVs and BAVs) during the cardiac cycle. OSI measures the cycle oscillatory nature or the directionality of the WSS at each point (as we explained in Chapter 3 - see equation (24) for the definition). We noted that the OSI decreases when the valve is opening or closing, but in transition moments (from open position to closed position) OSI increases until values are close to 0.5 (representing a purely bi-directional/oscillatory flow). Consequently, Figure 4.33.B, presents the average value of OSI for each created model, being the OSI values between 0.34 (BAV 4) and 0.44 (TAV 1).

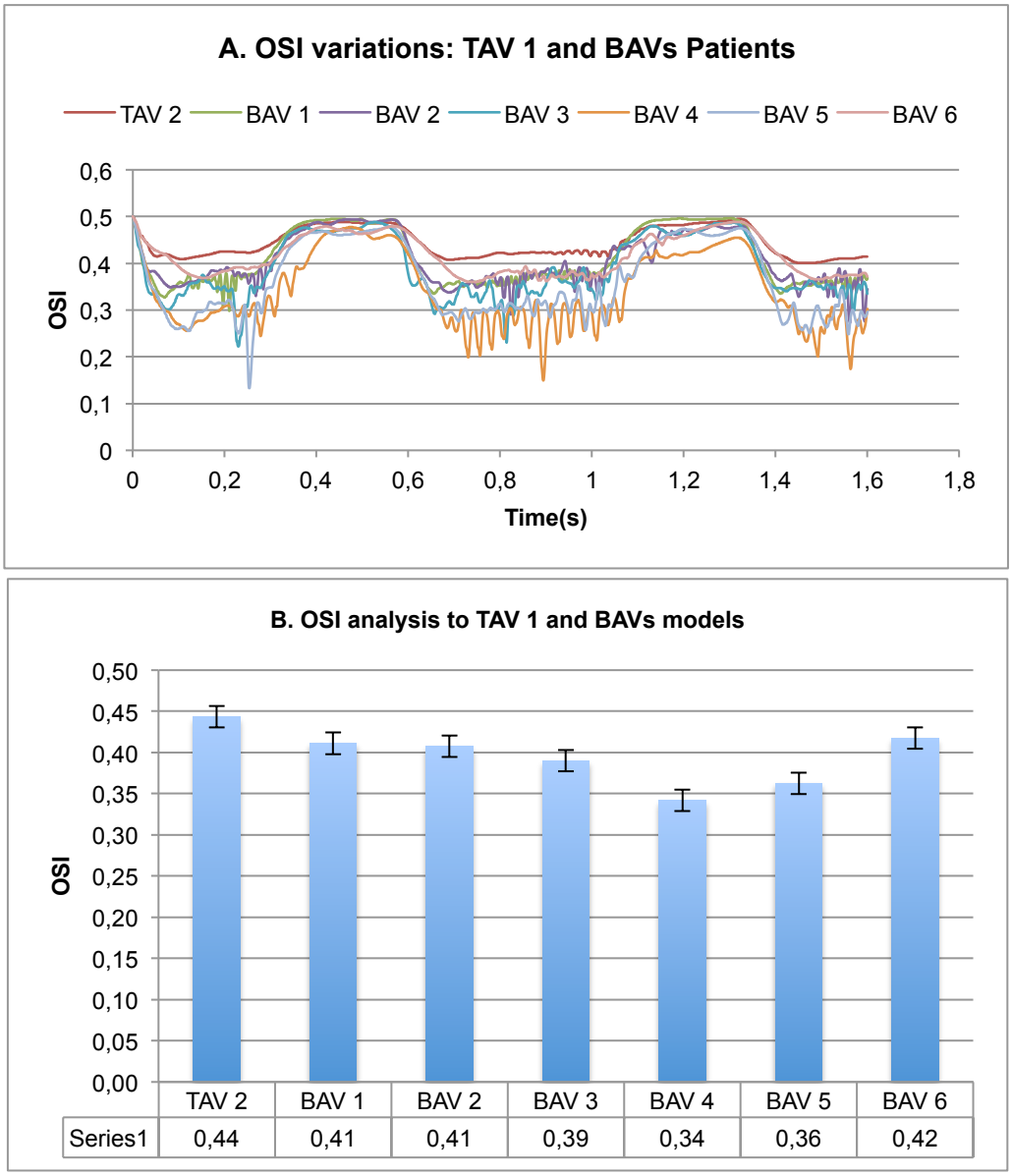

Figure 4.33. OSI variations for TAVs and BAVs created models: A. OSI during two cardiac cycles. B. Average of OSI for each model.

4.3. Main study findings

The results obtained from the current 2D study allow a comparison of each BAV with respect to the TAV 2. We noted that the resultant hemodynamics is dependent of the type of geometry considered: (i) with or without cusp symmetry (TAV and BAVs, respectively) and (ii) the dimensions of each aortic root component (considering the BAV models).

In fact the blood flow is sensitive to the valve geometry. Heterogeneous recirculation regions are observed in the different BAV models (due to the leaflets asymmetries), compared to the TAV model (the symmetric model). We conclude that the BAVs amplify the “flow effects” (recirculation regions and the asymmetric blood flow). These “flow effects” are caused by the geometrical asymmetry (due to the larger and the longer fused cusp). In the BAVs cases, these recirculation regions will interfere with the blood flow, particularly in the region of the ascending thoracic aorta, with higher WSS effects being verified in these regions. We assume that we observe some turbulence phenomena (in some cases) in this region, due to the formation of vortices. This turbulence promotes the calcification process on the leaflets of the valve, leading to a cycle of deterioration of the valve.

The peak stresses took place on the cusp base and the lowest stress occurred on their free edges. The fused leaflet suffered a greater deflection, compared to the other leaflet. Higher velocity magnitudes are associated to higher Von Mises stress values.

Regarding the WSS, the fused leaflet was more affected compared to the non-coronary leaflet, due to its properties. The WSS was higher along the leaflets, particularly on the belly and on the tip region, but also along the ascending thoracic region. In contrast, the wall of the aortic sinus had a minimum WSS value.

Some of the previous results, resulting from the comparison between the TAV 2 and the BAVs models, are summarized in Table 4.1. We think that this data allow an understanding of the mechanical stress concentration in the different created valves. Thus, a possible application is the improvement of the BHV design.

Table 4.1. Summary of the results for all models compared to TAV 2 model (according some instants of time).

TAV 2	Velocity Magnitude (m/s)	Von Mises Stress (Pa)	WSS (N/m^2)
TAV 1 (t = 0.116s)	+ 23.53%	+ 22.73%	+ 31.42%
BAV 1 (t=0.076 s)	+ 26.88%	+ 37.5%	+ 77.68%
BAV 2 (t = 0.116s)	+ 8.60%	+ 44.74%	+ 70.6%
BAV 3 (t=0.076 s)	+ 22.11%	+ 53.82%	+ 66.42%
BAV 4	+ 13.27% (t=0.144 s)	+ 38.8% (t=0.116s)	+ 67.88% (t=0.116s)
BAV 5 (t=0.116s)	+ 19.46%	+ 57.84%	+ 71.89%
BAV 6	+ 28.57% (t=0.3s)	+ 27.42% (t=0.116s)	+ 61.19% (t=0.116s)

4.4. 3D TAV model

Finally we created a 3D TAV model to do some numerical simulations. Figure 4.34 (A and B) present the Von Mises stress from the inlet (A) and the outlet (B) views, at t=0s. Figure 4.34(C) shows the same result but with the velocity streamlines at t=0s.

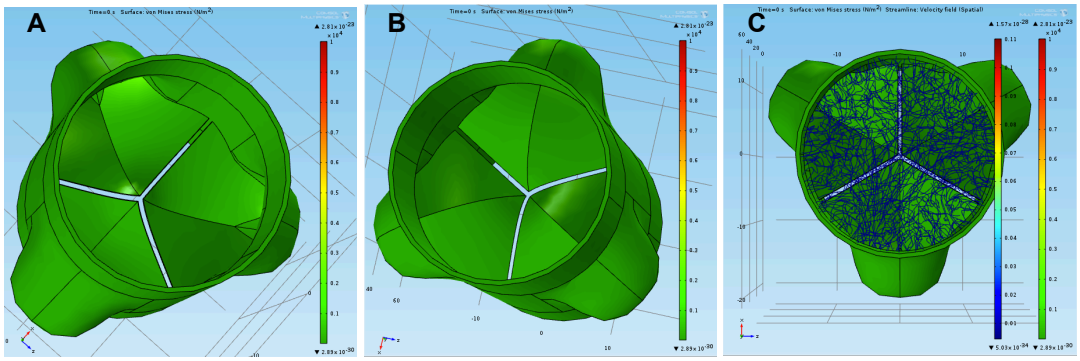

Figure 4.34. 3D TAV model: Von Mises Stress from inlet (A) and outlet (B) views at t=0s. (C) Von Mises Stress from inlet view with velocity streamlines.

According to the boundary conditions applied, Figure 4.35 (A,B,C,D) shows for t=0.058s (A), t=0.1s(B), t=0.165s(C) and t=0.2s (D), the maximum velocities of 0.3 m/s (open position), 0.13 m/s

(closed position), 0.3m/s (open position) and 0.15 m/s (closed position). We observed the Von Mises stress values between $2.24x10^4$ Pa and $9.1x10^4$ Pa.

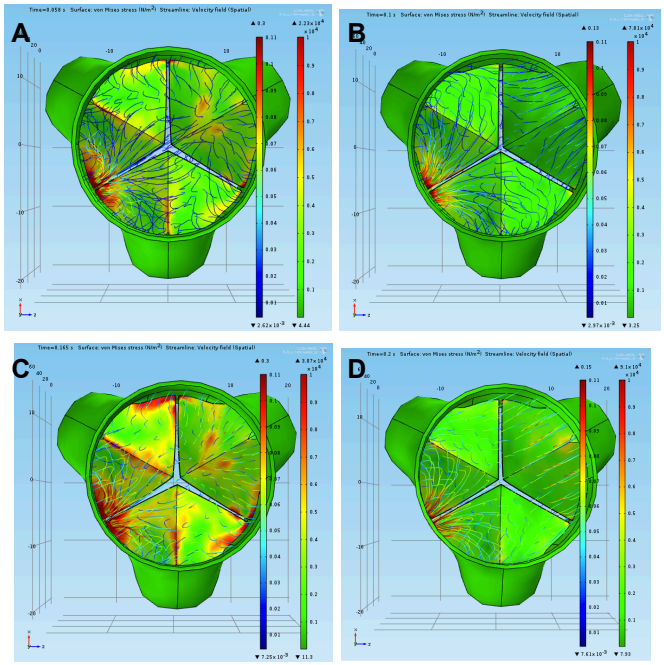

Figure 4.35. 3D TAV model: velocity flow field and Von Mises stress from the inlet view, at t=0.058s (A), t=0.1s(B), t=0.165s(C) and t=0.2s (D).

Figure 4.36 (A and B) shows the velocity field magnitude in the TAV model. We realize that the maximum velocity values are observed at inlet boundary and the minimum velocity values are verified at the outlet boundary.

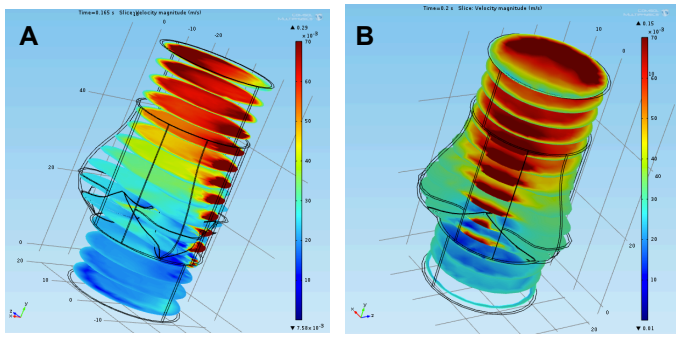

Figure 4.36. 3D TAV model: Velocity field magnitude (slice representation) from inlet view, at t=0.165s(A) and t=0.2s (B).

The results obtained for the 3D TAV model are not physiological, and the main reason is because the FSI based on an ALE formulation didn't allow the contact of the leaflets. Possibly, it also requires the development of a new algorithm for remeshing.

CHAPTER 5

Conclusions and Future Developments

This thesis describes the application of a fluid structure interaction numerical method based on an ALE formulation using COMSOL Multiphysics to obtain numerical solutions with the purpose of helping the clinical decision and the understanding of the BAV pathophysiology. Thus, different models were created, in particular: (i) an idealized TAV model and six patient specific BAVs models where different aspects of the blood flow, during the cardiac cycle (considering the 2D case), were analyzed; (ii) also an idealized 3D TAV model, based on the 2D TAV geometry.

To reach the initial objectives numerical simulations were performed to obtain approximate results of: (i) the blood flow (with maximum velocities for the BAVs around 2 m/s that had important consequences in other indicators, such as the WSS and the OSI number); (ii) the Von Mises stresses, on the cusps and on the wall (with the maximum values of 1.0×10^6 Pa).

In fact disturbed flow conditions (such as recirculation regions) can exacerbate the BAV disease[58]. BAVs show a particular hemodynamic behavior due to characteristics of the fused leaflet. Abnormal WSS stresses were concentrated (average WSS values between 8 and 12 N/m^2) on the leaflets. These values can affect the aortic root during the valvular function, resulting in vascular complications (for example, calcification of the leaflets and the ascending aortic pathologies, in particular the dilatation).

Regarding the medical images quality, there are limitations in the image resolution to provide accurate information of the thickness and the leaflets length of the structures[13]. In this work the thicknesses found in the literature were used for the leaflets. To improve the quality of this study more results would be needed and also more patients with the same age for validation. In our population (BAV analysis) we have an heterogeneous population of males and females.

We observed some difficulties: (i) it is difficult to obtain patient-specific material properties, material properties specifications from the literature have been assumed; (ii) during the FSI simulations large structural displacements of the cusps have been verified (this implied the change of the topology making difficult the use of the ALE formulation). The main limitations related with the ALE method are: (i) for large mesh deformations the quality of the mesh created by the applied smoothing method can be deteriorated; (ii) problems in the convergence; and consequently, inverted element elements are generated. As consequence of these limitations, the accuracy of the solution can be deteriorated and the solver can diverge generating an ill-conditioned system. This was the main reason to develop 3D simulation only during 0.2 s. With realistic boundary conditions, the 3D simulation present higher velocities, but due to the leaflets contact there are convergence problems (Figure 5.1).

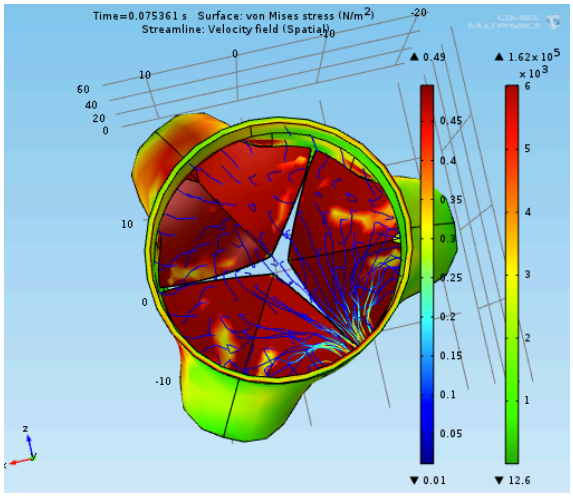

Figure 5.1. 3D TAV model result with different inlet boundary conditions.

In relation to future developments they can be summarized as follows: (i) inclusion of an aortic arch in the 2D BAV models due to the predisposition to the weakening of the aortic wall; (ii) expansion of the 2D BAV models to 3D BAV models, studying the same indicators but with more realist boundary conditions; (iii) the extension to realistic BAV geometries reconstructed from medical images.

References

1. S.K. Atkins. Etiology of bicuspid aortic valve disease: focus on hemodynamics. *World Journal of Cardiology,* 6(12):1227, 2014.
2. S. Morganti (2011). Finite element analysis of aortic valve surgery, PhD Thesis in Bioengineering and Bioinformatics, University of Pavia, Faculty of Engineering.
3. A.C. Braverman, H. Güven, et al. The bicuspid aortic valve. *Current Problems in Cardiology*. 30(9):470-522, 2005.
4. C.M. Otto, R.O. Bonow (2014). Valvular Heart Disease. Braunwald's Heart Disease: A Textbook of Cardiovascular Medicine (4th edition). Philadelphia.
5. H. Sievers, C. Schmidtke. A classification system for the bicuspid aortic valve from 304 surgical specimens. *The Journal of Thoracic and Cardiovascular Surgery.*133(5):1226-1233, 2007.
6. E. Girdauskas, M.A. Borger, et al. Novel phenotypes in bicuspid aortic valve disease, 315-330, 2011.
7. N. Yener, G.L. Oktar, et al. Bicuspid aortic valve. *Annals of Thoracic and Cardiovascular Surgery.* 8(5):264-267, 2002.
8. R. Gnyaneshwar, R.K. Kumar, et al. Dynamic analysis of the aortic valve using a finite element model. *Annals of Thoracic and Cardiovascular Surgery,* 73(4):1122-1129, 2002.
9. H. Kim, J. Lu, M. Sacks, et al. Dynamic simulation of bioprosthetic heart valves using a stress resultant shell model. *Annals of Biomedical Engineering*, 36(2):262-275, 2008.
10. M. Sacks, W. Sun, et al. Simulated bioprosthetic heart valve deformation under quasi-static loading. *Journal of Biomechanical Engineering*,127(6):905-914, 2005.
11. J. De Hart, G. Peters, et al. A three-dimensional computational analysis of Fluid Structure Interaction in the aortic valve. *Journal of Biomechanics*, 36:103-112, 2003.
12. N. Piazza, P. de Jaegere, et al. Anatomy of the aortic valvular complex and its implications for transcatheter implantation of the aortic valve. *Circulation: Cardiovascular Interventions*,1(1):74-81,2008.
13. K.B. Chandra, S.C. Vigmostad. Patient-specific bicuspid valve dynamics: an overview of methods and challenges. Journal of Biomechanics, 46(2):208-216, 2014.
14. G. Marom. Numerical Methods for Fluid Structure Interaction models of aortic valves. *Archieves of Computational Methods*, 22(11):595-620, 2015 (doi:10.1007/s11831-014-9133-9).
15. G. Marom (2012). Fluid Structure Interaction modeling of native aortic valve with root replacement and asymmetric configuration. PhD Thesis, Tel Aviv University, The Zandman-Slaner Graduate School of Engineering.
16. P.N. Jermihov (2013). Biomechanical implications of congenitally bicuspid aortic valves : a finite element analysis of patient-specific geometry. PhD Thesis in Biomedical Engineering, University of Iowa.
17. S. Chandra, P. Sucosky, et al. Computational assessment of bicuspid aortic valve wall-shear stress: implications for calcific aortic valve disease. *Biomechanics and Modeling in Mechanobiology*,11:1085-1096, 2012.
18. Software COMSOL Multiphysics (v. 4.4), with the licence number:17073661.

19. H. Sievers, E.I. Charitos. Anatomy of the aortic root: implications for valve-sparing surgery. *Annals of Cardiothoracic Surgery*, 2(1):53-56, 2013.
20. H. Sievers, W. Hemmer, et al. The everyday used nomenclature of the aortic root components: the tower of babel? *European Journal Cardio-thoracic Surgery*, 41(3):478-482, 2012.
21. R. Van Loon (2005). A 3D method for modeling the fluid-structure interaction of heart valves. Archieves of the Bulletin of the American Physical. PhD Thesis in Biomedical Engineering, Eindhoven University of Technology.
22. A. Hasan, K. Ragaert, et al. Biomechanical properties of native and tissue engineered heart valve constructs. *Journal of Biomechanics*, 47:1949-1963, 2013.
23. P.M. Taylor, P. Batten, et al. The cardiac valve interstitial cell. *The International Journal of Biochemistry and Cell Biology*, 35(2):113-118, 2003.
24. M. Sacks, W. D. Merryman, et al. On the biomechanics of heart valve function. *Journal of Biomechanics*, 42(12):1804-1824, 2009.
25. K. Balachandran, P. Sucosky, et al. Hemodynamics and mechanobiology of aortic valve inflammation and calcification. *International Journal of Inflammation,* 263870, 2011.
26. M. Sacks. Incorporation of experimentally-derived fiber orientation into a structural constitutive model for planar collagenous tissues. *Journal of Biomechanical Engineering*, 125(2):280-287, 2003.
27. P.N. Jermihov, M. Sacks, et al. Effect of geometry on the leaflet stresses in simulated models of congenital bicuspid aortic valves. *Cardiovascular Engineering and Technology*, 2(1):48-56, 2011.
28. E. Aikawa (2013). Calcific Aortic Valve Disease. InTech Publisher.
29. K.L. Losenno, R.L. Goodman, at al. Bicuspid aortic valve disease and ascending aortic aneurysms: gaps in knowledge. *Cardiology Research and Practice*, (1):145202, 2012.
30. J. Robledo-Carmona, I. Rodríguez-Bailón, et al. Hereditary patterns of bicuspid aortic valve in a hundred families. *International Journal of Cardiology*, 168(4):3443-3449, 2013.
31. K.D. O'Brien. Pathogenesis of calcific aortic valve disease: a disease process comes of age (and a good deal more). *Arteriosclerosis, Thrombosis and Vascular Biology*, 26(8):1721-1728, 2006.
32. P.W.M. Fedak, S. Verma, et al. Clinical and pathophysiological implications of a bicuspid aortic valve. *Circulation*,106:900-904, 2002.
33. C. Vergara, F. Viscardi et al. Influence of bicuspid valve geometry on ascending aortic fluid dynamics: a parametric study. *Artificial Organs*, 36(17):368-378, 2012.
34. C. Ward. Clinical significance of the bicuspid aortic valve. *Heart*, 83(1):81-85, 2000.
35. C.M. Otto. Calcification of bicuspid aortic valves. *Heart*. 88(4):321-322, 2002.
36. E. Girdauskas, M.A. Borger, et al. Is aortopathy in bicuspid aortic valve disease a congenital defect or a result of abnormal hemodynamics? A critical reappraisal of a one-sided argument. *European Journal of Cardiothoracic Surgery*, 39(6):809-814, 2011.
37. S.C. Siu, C.K. Silversides. Bicuspid aortic valve disease. *Journal of the American College of Cardiology*, 55(25):2789-2800, 2010.
38. S. Yuan, H. Jing.The bicuspid aortic valve and related disorders. *Sao Paulo Medical Journal*,128(5):296-301, 2010.

39. B. Fernández, V. Sans-Coma, et al. Anatomy and formation of congenital bicuspid and quadricuspid pulmonary valves in syrian hamsters. *The Anatomical Record*, 250(1):70-79, 1998.
40. B. Fernández, A.C. Durán, et al. Bicuspid aortic valves with different spatial orientations of the leaflets are distinct etiological entities. *Journal of the American College of Cardiology*, 54(24):2312-2318, 2009.
41. V. Sans-Coma, B. Fernández, et al. Fusion of valve cushions as a key factor in the formation of congenital bicuspid aortic valves in syrian hamsters. *The Anatomical Record*, 244(4):490-498,1996.
42. P.W.M. Fedak, M.P.L. De Sa, et al. Vascular matrix remodeling in patients with bicuspid aortic valve malformations: Implications for aortic dilatation. *The Journal of Thoracic Cardiovascular Surgery*, 126(3):797-806, 2003.
43. I. Mordi, N. Tzemos. Bicuspid aortic valve disease: a comprehensive review. *Cardiology Research and Practice*, (1):196037, 2012.
44. S.M Fernandes, P. Khairy, et al. Bicuspid aortic valve morphology and interventions in the young. *Journal of the American College of Cardiology*, 49(22):2211-2214, 2007.
45. B.M. Schaefer, M.B. Lewin, et al. Usefulness of bicuspid aortic valve phenotype to predict elastic properties of the ascending aorta. *American Journal of Cardiology*, 99(5):686-690, 2007.
46. H.Y. Sabet, W.D. Edwards, et al. Congenitally bicuspid aortic valves: a surgical pathology study of 542 cases (1991 through 1996) and a literature review of 2,715 additional cases. *Mayo Clinic Proceedings*, 74(1):14-26, 1999.
47. S.M. Fernandes, S.P. Sanders, et al. Morphology of bicuspid aortic valve in children and adolescents. *Journal of the American College of Cardiology*, 44(8):1648-1651, 2004.
48. V. Jackson, C. Olsson, et al. Aortic dimensions in patients with bicuspid and tricuspid aortic valves. *The Journal of Thoracic and Cardiovascular Surgery*,146(3):605-610, 2013.
49. F. Robicsek, M.J. Thubrikar, et al. The congenitally bicuspid aortic valve: how does it function? why does it fail? *The Annals of Thoracic Surgery*, 77(03):177-185, 2004.
50. S.K. Atkins. Etiology of bicuspid aortic valve disease: focus on hemodynamics. *World Journal of Cardiology*, 6(12):1227, 2014.
51. M.R. Dweck, N.A. Boon, et al. Calcific aortic stenosis. *Journal of the American College of Cardiology*, 60(19):1854-1863, 2012.
52. M.D. Hope, T.A. Hope, et al. Bicuspid aortic valve: four-dimensional MR evaluation of ascending aortic systolic flow patterns. *Radiology*. 255(1):53-61, 2010.
53. M. Soncini, E. Votta, et al. Finite element simulations of the physiological aortic root and valve sparing corrections. *Journal of Mechanics in Medicine and Biology*, 06(01):91-99, 2006.
54. M Bäck, T.C. Gasser, et al. Biomechanical factors in the biology of aortic wall and aortic valve diseases. *Cardiovascular Research*, 99:232-241, 2013.
55. E. Sirois, Q. Wang, et al. Fluid simulation of a transcatheter aortic valve deployment into a patient-specific aortic root. *Cardiovascular Engineering and Technology*, 2(3):186-195, 2011.
56. L. A. Freeman, P.M. Young, et al. CT and MRI assessment of the aortic root and ascending aorta. *American Journal of Roentgenology*, 200(6), 2013.

57. G.N. Levine, A.S. Gomes, et al. Safety of magnetic resonance imaging in patients with cardiovascular devices: An american heart association scientific statement from the committee on diagnostic and interventional cardiac catheterization, Council on Clinical Cardiology, and the Council on Cardiovascular Radiology. *Circulation*, 116(24):2878-2891, 2007.

58. P.J. Cawley, C.M. Otto, et al. Valvular heart disease : changing concepts in disease management. *Circulation*, 468-478, 2009.

59. J.F. Gerbeau, M. Astorino, et al. Computational analysis of an aortic valve jet with lagrangian coherent structures. *Chaos: An Interdisciplinary Journal of Nonlinear Science*, 20:1-10, 2010.

60. K. Chandran, M. Sacks, et al. Effect of geometry on the leaflet stresses in simulated models of congenital bicuspid aortic valves. *Cardiovascular Engineering and Technology*, 1(1):18-38, 2010.

61. K.J. Grande, R.P. Cochran et al. Mechanisms of aortic valve incompetence: finite element modeling of aortic root dilatation. *The Annals of Thoracic Surgery*, 69(6):1851-1857, 2000.

62. H. Kim, M. Sacks, et al. An experimentally derived stress resultant shell model for heart valve dynamic simulations. Annals of Biomedical Engineering, 35(1):30-44, 2007.

63. J. De Hart, G.W. Peters, et al. A two-dimensional fluid structure interaction model of the aortic valve. *Journal of Biomechanics*, 33(9):1079-1088, 2003.

64. J. De Hart (2002). Fluid structure interaction in the aortic heart valve: a three-dimensional computational analysis. PhD Thesis, Eindhoven University.

65. J. N. Reddy (1988). An Introduction to the Finite Element Method with Application to Nonlinear Problems. McGraw-Hill (2nd edition). Texas A & M University.

66. K.J. Grande, R.P. Cochran, et al. Stress variations in the human aortic root and valve: the role of anatomic asymmetry. *Annals of Biomedical Engineering*, 26(4):534-545, 1998.

67. C.A. Conti, A. Della Corte, et al. Biomechanical implications of the congenital bicuspid aortic valve: a finite element study of aortic root function from in vivo data. *The Journal of Thoracic Cardiovascular Surgery*, 140(4):890-896, 2010.

68. G. Marom, H.K. Moshe, et al. Fully coupled fluid-structure interaction model of congenital bicuspid aortic valves: effect of asymmetry on hemodynamics. *Medical and Biological Engineering and Computing*, 51:839-848, 2013.

69. H.G. Bahraseman, K. Hassani, et al. Estimation of maximum intraventricular pressure: a three-dimensional fluid structure interaction model. *Biomedical Engineering Online*,12:122, 2013 (doi:10.1186/1475-925X-12-122).

70. E.J. Weinberg, M.R. Kaazempur Mofrad. A multiscale computational comparison of the bicuspid and tricuspid aortic valves in relation to calcific aortic stenosis. *Journal of Biomechanics*, 41:3482-3487, 2008.

71. S. Katayama, N. Umetani, et al. Bicuspid aortic valves undergo excessive strain during opening: A simulation study. *The Journal of Thoracic Cardiovascular Surgery*, 145(6):1570-1576, 2013.

72. E.J. Weinberg, M.R. Kaazempur Mofrad. Transient, three-dimensional, multiscale simulations of the human aortic valve. *Cardiovascular Engineering*, 7:140-155, 2007.

73. M.Y. Kuan, D.M. Espino Systolic fluid-structure interaction model of the congenitally bicuspid aortic valve: assessment of modelling requirements. *Computer Methods in Biomechanics and Biomedical Engineering*, 18(12):1305-20, 2015 (doi: 10.1080/10255842.2014.900663).

74. L. Formaggia, A. Quateroni, et al (2009). Cardiovascular Mathematics: Modeling and Simulation of the Cardiovascular System. Volume 1, Springer.

75. D.M. Sforza, C.M. Putman, et al. Hemodynamics of cerebral aneurysms. *Annual Review of Fluid Mechanics,* 41:91-107, 2009.

76. M.K. Gobbert, S. Yang. Numerical demonstration of finite element convergence for lagrange elements in COMSOL Multiphysics, 1-15, 2008.

77. R.S. Beroukhim, T.L. Kruzick, et al. Progression of aortic dilation in children with a functionally normal bicuspid aortic valve. *American Journal of Cardiology*, 98(6):828-830, 2006.

78. J.S. Rankin, A.F. Dalley, et al. A “hemispherical” model of aortic valvar geometry. *The Journal of Heart Valve Disease*, 17(2):179-186, 2008.

79. C. Yap, A. Yoganathan et al. Experimental measurement of dynamic fluid shear stress on the aortic surface of the aortic valve leaflet. *Biomechanics and Modeling in Mechanobiology,* 18(9):1199-1216, 2013

80. G.Thiene, C. Basso. Pathology and pathogenesis of infective encarditiis in native heart valves. *Cardiovascular Pathology*, 15(5):256-263, 2006.